Charles University in Prague

Faculty of Mathematics and Physics

DOCTORAL THESIS

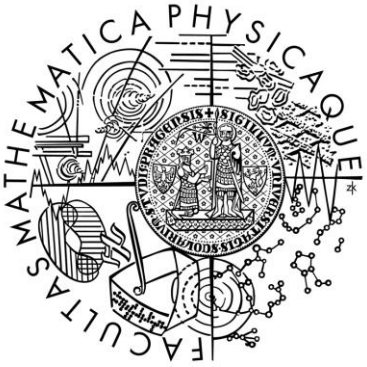

Roman Perekrestov

The investigation of low pressure HCPJ system for TiO_2 film deposition

Department of Surface and Plasma Science

Supervisor of the doctoral thesis: doc. Mgr. Pavel Kudrna, Dr

Study programme: Physics

Branch: Physics of Plasma and Ionized Media

Prague 2016

I would like to thank all the people who were involved in this doctoral work. Special thanks to my supervisor Mgr. Pavel Kudrna. Dr., who was patiently helping me during all years of study. His exceptional experience in electronics and plasma physics allowed us to overcome arising problems readily. A huge contribution in my research and education was made by RNDr. Milan Tichý, DrSc., who was a consultant of PhD work. He taught me methods of plasma diagnostics and actively took a part in a discussion of obtained results. Mgr. Ivan Khalakhan. Ph.D. was a person who greatly helped me with a diagnostics of thin films and his ideas were used in a characterization of results. A friendly atmosphere in a research team made the process of investigation enjoyable and significantly increased my motivation.

Special thanks to the Czech Republic and Charles University in Prague, in particular, which gives an opportunity for foreign citizens to get a high-quality education and supports them financially. Financial support by the Czech Science Foundation, grant No. 15-00863S and by Charles University Grant Agency, grant 268115 and 604612 is gratefully acknowledged.

I declare that I carried out this doctoral thesis independently, and only with the cited sources, literature and other professional sources.

I understand that my work relates to the rights and obligations under the Act No. 121/2000 Coll., the Copyright Act, as amended, in particular the fact that the Charles University in Prague has the right to conclude a license agreement on the use of this work as a school work pursuant to Section 60 paragraph 1 of the Copyright Act.

In…..... date..... signature

Název práce: Studium nízkotlakého systému HCPJ pro depozici tenkých vrstev TiO_2

Autor: Mgr. Roman Perekrestov

Katedra / Ústav: Katedra fyziky povrchů a plazmatu

Vedoucí doktorské práce: doc. Mgr. Pavel Kudrna, Dr.

Abstrakt: Plazmatické systémy jsou v současnosti široce využívané pro depozice tenkých vrstev jak pro komerční řešení tak i pro výzkumné účely. Zejména tam je pak potřebná detailní znalost parametrů plazmatu v těchto systémech nejen pro zajištění reprodukovatelnosti, ale i pro cílené ovlivňování vlastností deponovaných tenkých vrstev. Cílem disertační práce bylo studium parametrů plazmatu s ohledem na růst a vlastnosti tenkých vrstev vznikajících v systému plazmatické trysky s dutou katodou. Zkoumaným experimentálním zařízením byla plazmatická tryska, která pracovala v stejnosměrném režimu. Pro diagnostiku výboje byla používána Langmuirova sonda, kvadrupólový hmotnostní a optický spektrometr. Teplotu neurálního plynu ve výboji měřil teploměr s optickým vláknem. Růst nanočástic z plynné fáze byl studován pomocí rozptylu světla laserového paprsku. Pro diagnostiku tenkých vrstev Ti/TiO_2 bylo použito metod XPS, SEM, AFM, TEM, XRD a EDX. Fotovoltaická účinnost TiO_2 byla testována na barvivem senzitizovaném solárním článku.

Klíčová slova: plazmová tryska, Langmuirova sonda, nanočástice, oxid titaničitý

Title: The investigation of low pressure HCPJ system for TiO_2 film deposition

Author: Mgr. Roman Perekrestov

Department / Institute: Department of Surface and Plasma Science

Supervisor of the doctoral thesis: doc. Mgr. Pavel Kudrna, Dr.

Abstract: Plasma sources are widely used for deposition of thin films for both commercial solutions as well as for research purposes. In particular, information about plasma parameters in such systems is of a great importance not only to ensure reproducibility, but also for the targeted influence on properties of deposited thin films. The aim of the dissertation was the study of plasma parameters with respect to the growth and properties of thin films deposited by means of HCPJ sputtering system. The investigated plasma system was plasma jet powered in DC mode. The diagnostics of the discharge was carried out by means of a cylindrical Langmuir probe, quadrupole mass and optical spectrometer. Neutral gas temperature in discharge was measured by an optic-fibre thermometer. The growth of nanoparticles in a gas phase was studied using scattering of laser beam light. For the diagnostics of Ti/TiO_2 thin films were used XPS, SEM, AFM, TEM, XRD and EDX methods. The photovoltaic performance of TiO_2 thin films was tasted in dye-sensitized solar cells.

Keywords: plasma jet, Langmuir probe, nanoparticles, titanium dioxide.

Contents

1. Motivation and aims of doctoral thesis

In this work hollow cathode plasma jet (HCPJ) was investigated as a sputtering system for deposition of thin films. The principle of hollow cathode plasma jet is based on sputtering of the inner cathode surface by the high energy positive ions of working gas [1,2]. A sputtering system with HCPJ gives us an opportunity to control a wide range of parameters in a process of deposition. Among them the most important are: pressure, discharge current/voltage/power, working gas flow rate, etc. Manipulation with these parameters allows to create necessary conditions for deposition of thin films with certain properties. A plasma jet can be powered in DC, pulsed DC and RF regime. RF plasma jets are usually used for sputtering of nonconductive materials. One of the significant advantages of HCPJ over the magnetron sputtering is a continuous flow of the working gas which (i) helps to achieve a higher purity of the films and (ii) gives us control of the divergence of the flow of sputtered atoms. However, magnetron sputtering allows thin film deposition on larger areas with less difference in a thickness.

One of the main aims of PhD work was to obtain and investigate TiO_2 thin films deposited by HCPJ [3]. This material was chosen because of its exceptional applicability in energy sector of science and technology. There are a number of examples of its application in the fabrication of lithium ion batteries [4,5], visible light-driven photocatalytic hydrogen production [6] and photo electrodes for dye-sensitized solar cells (DSSC) e.g. [7,8].

The HCPJ proved to be a good source for nanoparticle synthesized from a gas phase [3]. In a general case particles with a size from 1 to 100 nm are called nanoparticles. The application of nanoparticles is rapidly growing in nanoscale science and engineering. Such properties of nanoparticles as surface to volume ratio, quantum confinement and surface atom arrangement are of a great importance. It means that by controlling the size of nanoparticles we can obtain new properties of material. The widely spread techniques of gas-phase nanoparticle synthesis using evaporation of solid material are: pulsed laser ablation [9], spark discharge generation [10], flame reactors [11] and ion sputtering [12].

Surface morphology, chemical composition and crystalline structure of Ti and TiO_2 thin films were investigated by the different experimental techniques. Scanning electron microscope (SEM), atomic force microscope (AFM) and transmission

electron microscope (TEM) were used for surface morphology characterization. The combination of these methods gives us complex information about the thin film surface. Energy dispersive analysis (XRD) was used for detection of impurities and correspondence of atomic concentration of different element to the stoichiometry of TiO_2. The diagnostics of chemical composition of thin film was carried out by means of X-ray photo electron spectroscope (XPS) in order to check the existing chemical bonds on the surface. Crystalline structure of TiO_2 thin films were studied by means of both X-ray diffraction (XRD) and TEM methods. Photovoltaic tests of TiO_2 films were carried out in order to evaluate the perspective of their application in dye sensitized solar cells[13].

A deposition process starts in the plasma plume, hence plasma has a direct influence on the thin films growth. Information about plasma brings more understanding and control over the process of deposition. In our laboratory the main instrument for plasma diagnostics is Langmuir probe. This technique is the oldest and most often used for investigation of a low temperature plasmas. The main advantages of this method are a simplicity in exploitation and a wide list of parameters we are able to estimate from the measured data: electron/ion energy, electron/ion energy distribution function, ionization degree, plasma potential, floating potential. The probe takes information from the certain place in plasma, therefore it is possible to measure spatial distribution of interesting for us plasma parameters. However, the presence of Langmuir probe in plasma brings some disturbance because it drains charged particles. Another disadvantage is complexity of measured data estimation.

Main chamber of our experimental vacuum system was equipped by the quadrupole mass spectrometer. It was used for quantitative determination of plasma composition and concentration of impurities, change of the signal from the most abundant ions in time during the process of deposition.

Since we deal with so called “dusty plasma” we tried to detect the nanoparticles in a gas phase. Our method, laser-induced scattering, is based on the detection of scattered light when the plasma with nanoparticles is illuminated by laser beam. Other techniques as laser-induced absorption [14], scattering [15] and fluorescence [16] have been developed for similar purposes. Instant data acquisition and low cost [17] makes laser-induced scattering technique more favourable to the other nanoparticle detection methods. It is possible to evaluate the nanoparticle mean

size/size distribution from the scattered laser intensity using Mie/Rayleigh theories. The nanoparticle detection in HCPJ plasma was not carried out before, therefore obtained results are of a great interest.

2. Theoretical part

2.1 Plasma

The first definition of plasma was given by Irving Langmuir during the investigation of a glow discharge. He described plasma as "brightly shining gas that consists of electrons, different sorts of ions and neutral atoms". He was the first who introduced the term "plasma" and main plasma parameters: ion density – n_i, electron density – n_e, density of neutral atoms – n_o and electron, ion and neutral gas temperatures T_e, T_i, T_o.

From the fundamental knowledge is well known that matter can be in three states – gaseous, liquid and solid. The current state of the matter is mostly defined by such parameters as pressure and temperature. If we heat up a material in a solid state then at certain temperature we will observe the transition from solid to liquid state. If we continue the process of heating the material will evaporate and becomes gaseous. The temperature of the state transition depends on the properties of the material. Further supply of energy will dissociate molecules and ionize atoms. If the concentration of ions and electrons will be sufficiently high such state of matter will get qualitatively new properties in comparison with normal gas. The concentrations of negative electrons and positive ions in sufficiently large volume tend to equalize to make this ionized gas quasineutral. Moreover, such state of matter has unique conductive properties in comparison with neutral gas. Thus, it can be affected by electric and magnetic fields. Provided that the studied volume is sufficiently large, the concentration of charged particles sufficiently high and the electrostatic interaction predominates the mechanical interaction during collisions with neutral particles this state of ionized gas is called plasma. These qualitative requirements are specified in more detail below.

Plasma is in a steady state only in a case of the continuously working ionization source. It can be DC (glow discharge, arc discharge, etc.) or RF discharge (electrodes powered by high frequency current, induction coils, etc). Plasma can be created by heating the neutral gas to high temperature that is sufficient for ionization. The laboratory plasma has as a rule low degree of ionization. For example electron

density in glow discharge of a fluorescent lamp is approximately 10^{15} m^{-3} while density of neutral gas atoms is about 10^{20} m^{-3}; that corresponds to degree of ionization 10^{-5}.

In plasma physics the temperature of particles is often expressed in energy units associating it with energy k_bT. In this case a common unit is eV (1 eV = 11600 K). Examples of typical values of charged particle concentration and temperature of plasmas in nature are given in **Tab. 2.1**.

Plasma source	Charged particle concentration [cm^{-3}]	Electron temperature [eV]
Fusion reactor	10^{15}	10^4
Tokamak	$10^{12} – 10^{14}$	$100 – 10^4$
Open trap	$10^{12} – 10^{14}$	$10 – 10^3$
Pinch	10^{16}	100
Gas discharge	$10^6 – 10^{12}$	2
Laser plasma	$10^{20} – 10^{24}$	$10^2 – 10^3$
Solar corona	10^6	200
Solar atmosphere	10^{14}	1
Earth's ionosphere	$10^5 – 10^6$	0.1
Solar wind	5	10 – 50
Interstellar gas	1	0.01 – 1

Tab. 2.1. The values of charged particle concentration and temperature for different types of plasmas in nature.

There are four criterions for an ionized gas to be treated as plasma [18]. The **first criterion** is *quasineutrality* which requires almost complete equality of positive and negative charge densities. In this case positive and negative charges compensate each other so that the electric field in plasma is approximately zero. It is explained by the strong electric field that appears even under the slight inequality of negative and positive charge carriers. In a presence of positive ions and electrons the quasineutrality can be expressed as $n_e \cong n_i$, where n_e and n_i are electron and ion concentrations.

Charged particles behave collectively and arrange themselves in such a way as to effectively shield any electrostatic fields. But the quasineutrality cannot be

fulfilled in small volumes, e.g. near the biased electrode. The characteristic distance of this shielding is called Debye length λ_D and can be calculated by the equation

$$\lambda_D = \sqrt{\frac{\varepsilon_0 k_b T_e}{n_e e^2}} \tag{2.1}$$

where ε_0 – dielectric permittivity of vacuum, k_b – Boltzmann constant, T_e – electron temperature, n_e – electron density and e – elementary charge. The quasineutral plasma is therefore separated from each outer source of electrostatic field by the region with positive or negative charge called *space charge sheath* which shields this electrostatic field. Dimensions of the space charge sheath are of the order of Debye length and the condition of quasineutrality may not be satisfied inside of the space charge sheath. The existence of space charge sheath or Debye shielding effect is a characteristic of all plasmas, although it does not occur in every medium that contains charged particles.

Further necessary and obvious requirement for plasma is that its dimensions should be larger than Debye length. If L is a characteristic dimension of plasma we can define the **second criterion** of plasma

$$L >> \lambda_D . \tag{2.2}$$

We can define the *Debye sphere* as a sphere inside the plasma of radius equal to Debye length. The electrostatic field outside of this sphere is effectively screened by the charged particles and does not affect the electric field in a centre of this sphere. Thus, charges inside of Debye sphere interact effectively with each other, while the charge interaction with outer charged particles can be neglected. The number of electrons N_D inside a Debye sphere is given by equation

$$N_D = \frac{4}{3}\pi\lambda_D^3 n_e = \frac{4}{3}\pi\left(\frac{\varepsilon_0 k_b T_e}{n_e^{1/3} e^2}\right)^{3/2} \tag{2.3}$$

Since the shielding effect is the result of the collective particle behaviour the number of electrons inside of Debye sphere should be very large. Hence, the **third criterion** of plasma is satisfaction of the inequality

$$\lambda_D^3 n_e >> 1. \tag{2.4}$$

The above expression expresses that the mean distance between electrons should be much smaller than λ_D. We can introduce the plasma parameter g, which physical meaning is the ratio of the mean inter-particle potential energy to the mean

plasma kinetic energy. The condition $g \gg 1$ is called plasma approximation. It is described by the following equation

$$g = \frac{1}{\lambda_D^3 n_e}. \tag{2.5}$$

When the external force is changed the internal electric field accelerates charged particles to restore the plasma quasineutrality. The restoring of the charge balance after this disturbance cannot be instantaneous because of the inertia of charged particles. This characteristic time is inversely proportional to the physical quantity that characterizes this oscillation and is known as *plasma frequency*

$$\omega_{pe} = \left(\frac{n_e e^2}{m_e \varepsilon_0} \right)^{1/2}, \tag{2.6}$$

where m_e is electron mass. Ions are much heavier than electrons, hence the collective motion of charged particles is provided mostly by electrons. It should be noted that only small disturbances in plasma are considered in this theory.

Collisions of electrons with neutral atoms and molecules dump the collective oscillation. From this we can derive the **fourth criterion** of plasma

$$\frac{\omega_{pe}}{2\pi} > \nu_{en}, \tag{2.7}$$

where ν_{en} is the electron-neutral collision frequency. Otherwise electrons will not be able to behave independently and will be forced by collisions towards the complete equilibrium with the neutrals [18].

2.2 Gas discharge

Term *gas discharge* is usually connected with processes of the electric current in the gas. The founder of gas discharge physics is the John Sealy Townsend. He created the theory of gas breakdown and principles of ionization at the beginning of 20-th century.

Modern physics treats gas discharge in more broad sense. It is not only the electrical current in gases but any process of gas ionization by means of electric field. This process occurs not only in constant electric field but also in high frequency (MHz), ultra-high frequency (GHz) and even in optical range (optical discharge).

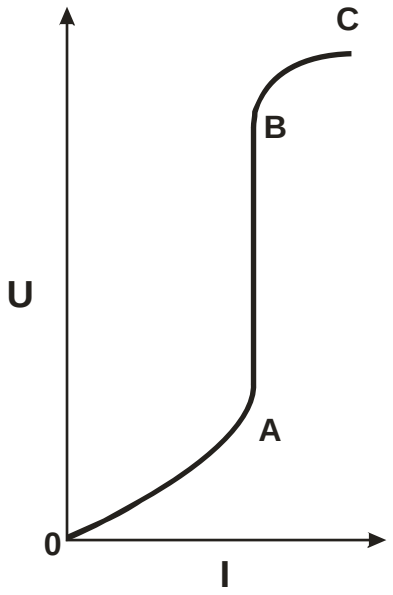

Fig. 2.1. Schematic current-voltage characteristic of non-self-sustaining discharge.

Discharges in constant electric field are divided into *self-sustaining* and *non-self-sustaining* [18,19]. Gases consisting of neutral atoms and molecules at room temperatures are almost nonconductive. The very small degree of ionization is caused by natural radioactivity, cosmic rays or ultraviolet radiation. Neutral particles in gas can be additionally ionized for example be means x-rays or collisions with electrons and other particles with energy necessary for the ionization.

Let's assume that ions in gas are created only by outer ionizer. Thus, the current and subsequently discharge stops after that ionizer switch-off. Such type of the discharge is called non-self-sustaining.

The typical current-voltage characteristic for non-self-sustaining discharge is qualitatively shown in **Fig. 2.1**. Discharge current grows at small applied voltages (curve 0A), than it reaches saturation and keeps almost independent of voltage (curve AB); that corresponds to the complete involvement of free charged particles created by the outer ionizer.

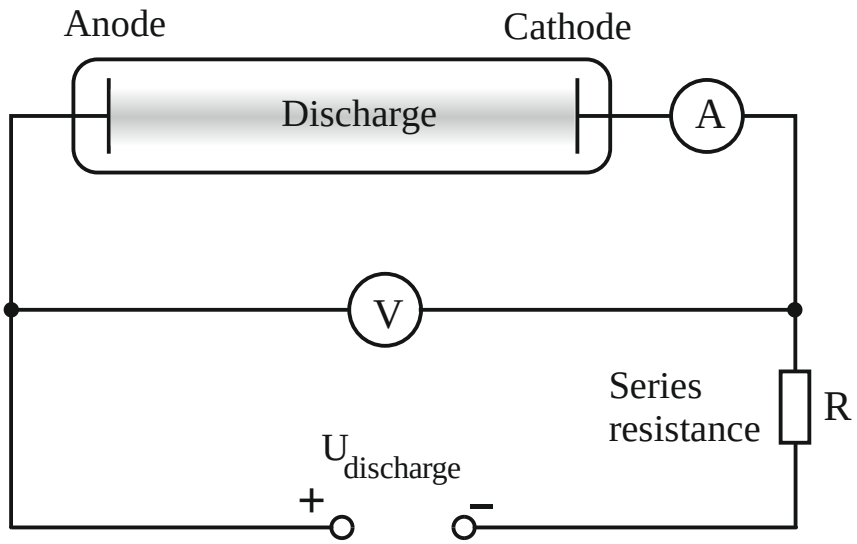

Fig. 2.2. The scheme for the measurement of I-V characteristic of a gas discharge lamp.

With further increase of the applied voltage the current starts to increase (BC). Ions and electrons are accelerated by the electric field. As soon as more electrons gain energies higher than the ionization threshold the electron avalanche appears. The discharge changes are still non-self-sustaining. This process depends on the pressure and ionization potential of neutral atoms and molecules in the discharge.

The conductivity of gas can, in sufficiently strong electric field, increase abruptly which is called breakdown. The corresponding voltage in a discharge gap is called breakdown voltage. If we remove the outer ionizer after breakdown the discharge current doesn't cease. It means that discharge is in self-sustaining mode and ionization is maintained by processes in the discharge itself.

I-V characteristic of the gas discharge tube is measured by means of the scheme that is described in **Fig. 2.2**. This electrical circuit includes the power supply E, with adjustable voltage that varies in a range from tens up to thousands V and changeable resistor that is called *series resistance*. This resistance is necessary for the restriction of the current and discharge stabilization in a region with negative differential resistance. In a regime with negative resistance the discharge is not stable and the discharge current tends to grow without limit. This electrical circuit also includes ammeter and voltmeter in order to measure the current and voltage between electrodes.

It is possible to obtain any known discharge mode in a given gas conductor by means of scheme in **Fig. 2.2**. The discharge regime is determined by intersection

point of load line (*U=E-RI*) and I-V characteristic of the discharge. We can choose the regime of the discharge by means of adjusting *E* and *R*.

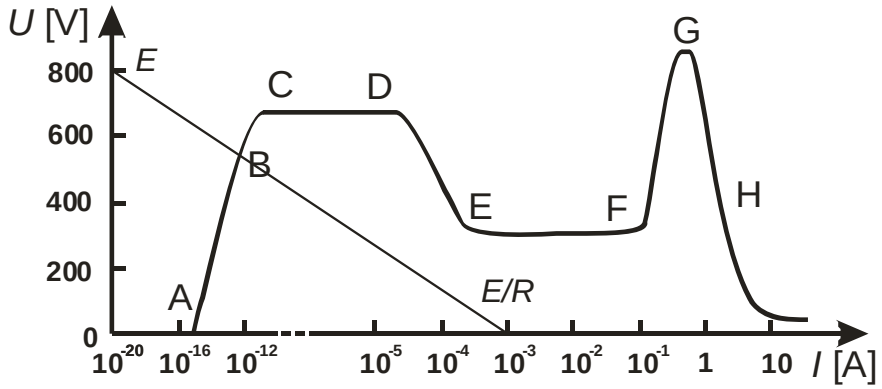

Fig. 2.3. I-V characteristic of discharge in neon at the pressure 1.3 mbar with load line.

The shape of I-V characteristic for certain gas conductor depends on the conditions. The most important parameter is pressure. I-V characteristic in neon discharge under the pressure 1.3 mbar is shown in **Fig. 2.3**. It is obtained experimentally by means of circuit shown in **Fig. 2.2**. The area of copper electrodes was 10 cm^2 and distance between them is 50 cm. The typical load line is also given in **Fig. 2.4**. The beginning of I-V characteristic is not possible to describe because of the low signal in absence of outer ionizer. The basic ionization is provided by natural radioactive radiation or cosmic rays. Characteristic starts from AB region that corresponds to saturation current. The breakdown occurs in point B. CD part corresponds to self-sustained dark discharge.

The part DEFG corresponds to the glow discharge where DE – subnormal glow discharge, EF – normal glow discharge and FG – anomalous glow discharge. GH corresponds to arc discharge. It is possible to obtain this regime with high value of current and low series resistance.

Qualitative scheme of glow discharge in a glass tube is given in **Fig. 2.5**. The dependencies of the main quantities that characterize plasma on horizontal coordinate are shown below – radiation intensity, electric field intensity, electron and ion currents, electron and ion concentration and total spatial charge density.

The discharge consists of light and dark regions. The distance from cathode to these regions is defined by electron mean free path because all processes in plasma are connected with electron – atom collisions. Dimensions of these regions are increasing with decrease of pressure. Dark Aston space is directly near the cathode

followed - in the direction towards the anode - by cathode glow and cathode dark space. Negative glow region with transition to Faraday dark space comes after that. The longest part is commonly the positive column and near the anode the dark anode space and anode glow are formed.

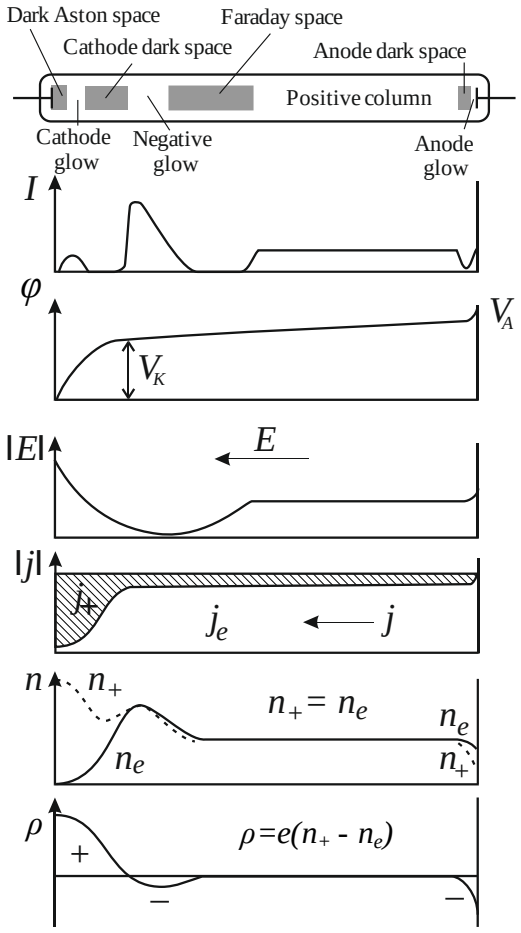

Fig. 2.4. Structure of the glow discharge and distribution of the main parameters along the horizontal discharge axis [19].

Usually, negative glow is the brightest region in the discharge. It has blue colour at the air, that's why this regime of the discharge is called "glow". Electrons emitted by the cathode have an energy that is not enough for excitation of atoms. That's why the layer in proximity to the cathode is dark (dark Aston space). After that electrons gain energy and first glowing region appears – cathode glow. Because of high electron energy the process of ionization becomes dominant. This process corresponds to the cathode dark space in **Fig. 2.4** Positive ions move along the discharge tube and create positive spatial charge. Electric field is weak in the end dark cathode space but a lot of relatively slow electrons moves towards anode. They are able to excite neutral gas atoms. The region of negative glow starts at this place.

Then electrons lose their energy and the glow transfers into Faraday space. In Faraday space electric field increases until it reaches positive column value. Positive column can be considered as the conductor with electron conductivity. Electrons continuously collide with neutral atoms and excitation occurs. Close to anode the positive ions practically do not exist and electrons form the negative space charge that creates small anode fall. Here electrons gain energy and cause anode glow. Dependencies shown in **Fig. 2.4** demonstrate given explanation.

2.2. Discharge in hollow cathode plasma jet

Hollow cathode glow discharge configuration is used for achieving high charge density in a simple way. Although a huge number of works about hollow cathode discharge is already published this topic is still interesting for science and technology. For the technology the hollow cathode plasma jets (HCPJ) are used as sputtering sources for thin films deposition. It can be used for physical vapour deposition (PVD) and plasma enhanced chemical vapour deposition (PECVD). During PVD deposition the thin film grows from particles sputtered from the cathode by impinging positive ions. PECVD methods use precursors in order to obtain thin films with complicated chemical composition.

Let's compare the hollow cathode discharge with normal glow discharge (NGD). Two configurations of glow discharge are given in **Fig. 2.5**. The upper scheme corresponds to NGD system with two planar electrodes. The current density j_0 can be calculated from the equation

$$j_0 = \frac{4\varepsilon_0 \mu_+ V_{cn}^2 (1+\gamma_i)}{d_n^3}, \tag{2.8}$$

where V_{cn} is the cathode voltage drop, d_n its length, μ_+ the ion mobility and γ_i the ion-electron secondary emission coefficient. The application of NGD system with planar electrodes for thin films deposition is not effective because sputtering rate is low. It is known that if we increase the current of the discharge in the current density j_0 stays constant but cathode spot increases its area.

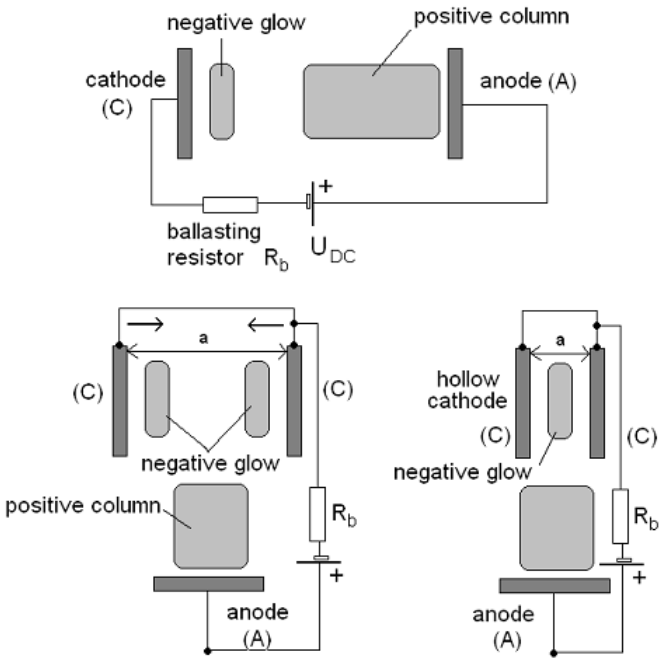

Fig. 2.5. The schemes of DC normal glow discharge (upper) and DC hollow cathode discharge (lower) systems [2].

The transition from NGD to anomalous glow discharge (AGD) occurs when the whole cathode area is covered by the cathode spot. In this case current density can reach values more than several units of mA/cm^2 under the discharge voltage from 2 up to 5 kV. However, even with this current density the sputtering rate is still low.

The principle of the hollow cathode is schematically shown in the lower part of the **Fig. 2.5**. Experiments have shown that if we decrease the distance between electrodes negative glows start to overlap. Due to the hollow cathode effect we can obtain the high plasma density between two connected cathodes at relatively low cathode voltage. The main processes in the hollow cathode are shown in **Fig. 2.6**.

Some electrons emitted from the cathode are able to leave the cathode fall region without suffering any collision. In this case they acquire the full energy of cathode fall. They are reflected from the opposite cathode fall region and this process continues in a form of oscillations. These oscillating high energy "pendulum electrons" play an important role in plasma ionization [2]. The discharge can be powered by DC or RF power sources whereas both types can be operated in continuous and pulsed modes. In the pulsed modes usually the weak continuous DC

or RF voltage is applied even between the pulses to maintain the stability of the discharge.

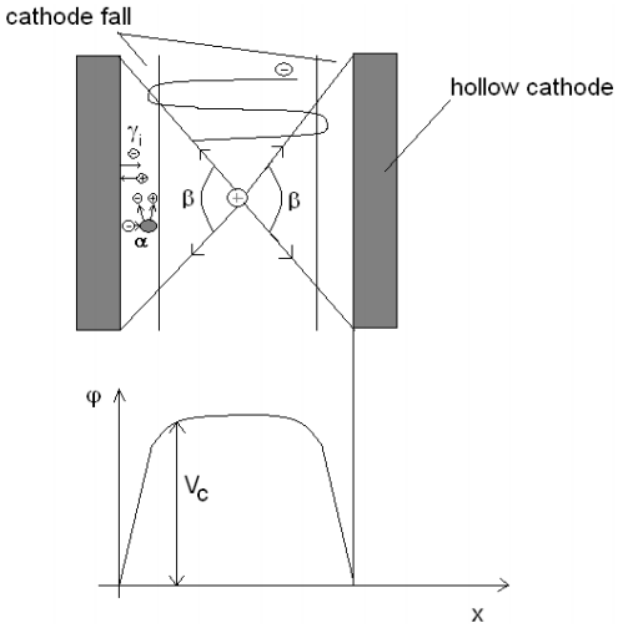

Fig. 2.6. The main processes involved in hollow cathode effect [2].

Another important process is the bombardment of the cathode surface by ions, metastables and photons which becomes a reason of secondary emission and hence the increasing of ionization. By means of anomalous hollow cathode discharge it is possible to obtain thousandfold higher level of ionization in comparison with normal glow discharge and consequently higher deposition rate.

2.3. Langmuir probe diagnostics

The electrical probes are used for plasma diagnostics since invented by I. Langmuir in 1923. The principal scheme and general shape of current-voltage characteristic is shown in **Fig. 2.7**. The Langmuir probe current is sum of currents I_{pe} and I_{pi} caused by the flows of negative and positive charges respectively. The probe attracts or repels charged particles in dependence of their charge and the probe potential with respect to plasma. Almost full difference of potentials between plasma and probe is concentrated in the space charge sheath – thin layer between plasma and probe surface. Langmuir probe theory is based on assumption that charged particles

move inside the sheath without collisions [2,19]. This assumption determines the range of pressures where the original Langmuir theory is applicable.

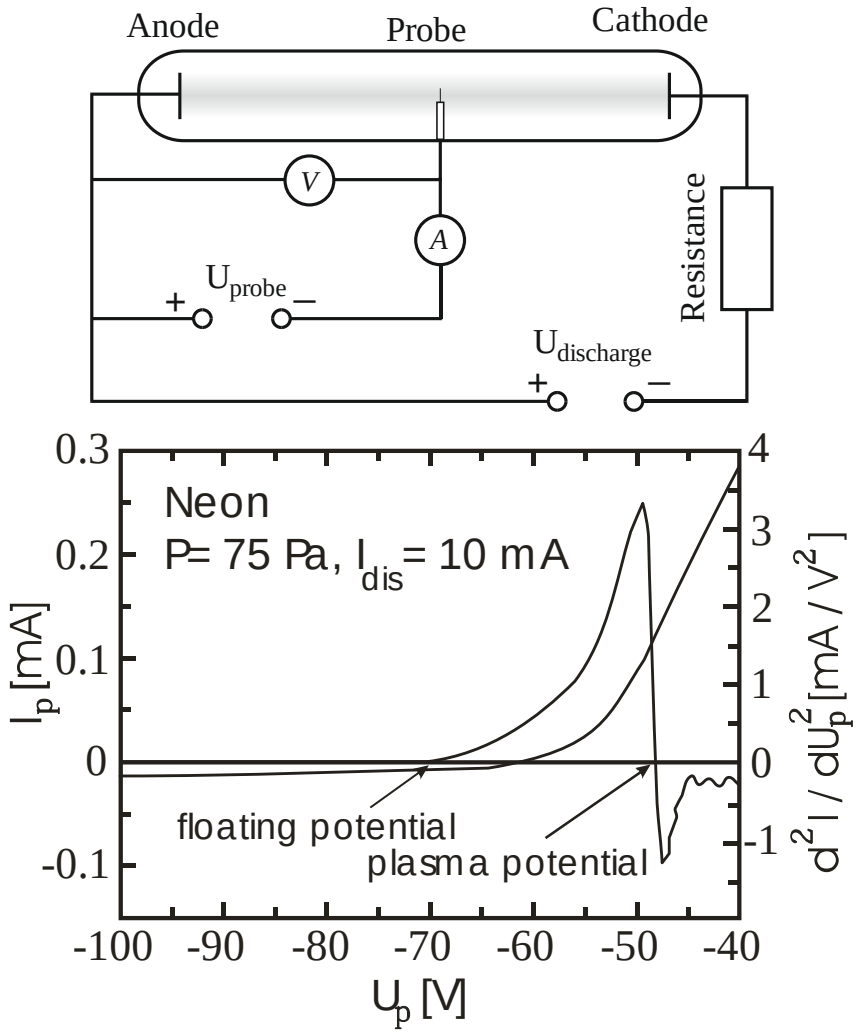

Fig. 2.7. The scheme of gas discharge lamp and I-V characteristic of Langmuir probe in neon discharge [2].

Together with the probe there must the reference electrode in the probe circuit. It can be one of the electrodes, any conductive part of the discharge chamber or special reference probe. In the case when dimensions of the probe are much less than dimensions of the reference electrode the I-V characteristics is determined by the sheath of probe only. The thickness of the probe sheath ($r_p - r_s$) is of the order of the Debye length (λ_D) and depends on the voltage difference between the plasma and probe potentials. Typical probe characteristic and its second derivative are shown in **Fig. 2.7**. Here the voltage corresponding to the zero probe current defines the floating potential U_{fl} and the voltage of the inflexion point define the space potential U_{sp}. The space potential is also called plasma potential since it is the potential of the

plasma at the probe position. The probe characteristics can be divided into three regions:

I	$U_p << U_{fl}$	$\rightarrow I_{pi}/I_{pe} >> 1$	*Positive ion acceleration region*
II	$U_{fl} \approx U_p \leq U_{sp}$	$\rightarrow I_{pi}/I_{pe} \approx 1$	*Transition region*
III	$U_{sp} \leq U_p$	$\rightarrow I_{pi}/I_{pe} << 1$	*Electron acceleration region*

Langmuir probe enables to determine the charged particle density, energy/velocity distribution function, plasma potential, and the electron temperature.

In the case of Maxwellian electron energy distribution function (EEDF) in unperturbed plasma, Boltzmann distribution of charged particles density in the probe sheath ($n=n_0 \cdot \exp[-eU/k_bT_e]$) and arbitrarily shaped probe, the electron current in the transition region is

$$I_e(U_p) = \frac{1}{4} e n_e \bar{v}_e S_p \exp \frac{e(U_p - U_{sp})}{k_b T_e},\ U_p \leq U_{sp} \tag{2.10}$$

where e is the electron charge, $\bar{v}_e = (8kT_e/\pi m)^{1/2}$ is mean electron velocity, n_e electron concentration, S_p probe surface area and T_e is electron temperature [19]. The pre-exponential factor in this equation represents the chaotic current at $U_p = U_{sp}$. The space potential U_{sp} is usually determined as the potential of the zero cross of the second derivative of the probe current $\mathrm{d}^2I_p/\mathrm{d}U_p^2 = 0$.

For arbitrary EEDF the electron current in the transition region is

$$I_e(U) = \frac{2\pi n_e e S_p}{m_e^2} \int_{eU}^{\infty} f(\varepsilon)(\varepsilon - eU)\mathrm{d}\varepsilon, \tag{2.11}$$

where e, m_e are electron charge and mass, ε is the electron energy, $f(\varepsilon)$ electron energy distribution function (EEDF) $\int_0^{\infty} f(\varepsilon)\mathrm{d}\varepsilon = 1$ and $U = U_p - U_{sp}$ is the probe potential with respect to plasma potential. Druyvesteyn expressed the EEDF using the second derivative of electron current in the transition region

$$f(\varepsilon) = 2^{3/2} n_e m^{1/2} e^{-3/2} S_p^{-1} U^{1/2} \frac{\mathrm{d}^2 I_e}{\mathrm{d}U^2}, \tag{2.12}$$

This equation is valid for convex probe geometries. The mean electron energy can be determined from the EEDF

$$\bar{\varepsilon} = \int_0^\infty \varepsilon f(\varepsilon) \mathrm{d}\varepsilon \,. \tag{2.13}$$

The electron density yields the integral of the second derivative of the electron current

$$n_e = 2^{3/2} m^{1/2} e^{-3/2} S_p^{-1} \int_0^\infty U^{1/2} \frac{\mathrm{d}^2 I_e}{\mathrm{d}U^2} \mathrm{dV} \,, \tag{2.14}$$

the chaotic flow of the electrons to the probe at plasma potential U_{sp} (electron saturation current)

$$n_e = \frac{4 I_e(U_{sp})}{e \bar{v} S_p} . \tag{2.15}$$

In case of the OML regime (probe sheath thicker than the probe radius) the n_e can be estimated from the slope of the square of the electron current dependence $I_e^2(U_p)$ on the probe voltage in the electron acceleration region

$$I_e^2(U_p) = \frac{2e^3 A_p n_e^2}{\pi^2 m_e} \cdot U_p + const \,. \tag{2.16}$$

In the case of Maxwellian EEDF the electron temperature T_e can be determined from the slope of the semi logarithmic plot of probe characteristics in the transition region

$$\frac{k_b T_e}{e} = -\left[\frac{\mathrm{d}(\ln I_e)}{\mathrm{d}U_p} \right]^{-1} . \tag{2.17}$$

The ion density can be determined from the ion saturation current part of I-V characteristics. It is one of the most complicated problems of the probe diagnostics: it is necessary to know the theoretical description of ion current-voltage dependence that in turn depends (among others) on the plasma parameters being estimated: namely plasma density, electron temperature and plasma ion composition. The ion current can be usually approximated by the formula:

$$I_i = e n_i S_p \left(\frac{k_b T_e}{2\pi M_i} \right)^{1/2} \left(\frac{eU_p}{k_b T_e} \right)^n , \tag{2.18}$$

where M_i is the ion mass and n has to be determined experimentally. For the thin probe and collision less thick sheath $n = 0.5$.

The important advantages of the probe diagnostic are the simplicity of experimental setup, number of plasma parameters which can be estimated and the spatial resolution. As disadvantages of the probe method can be mentioned

complicated data processing, disturbance of the plasma by the probe presence and its drain of the charge carriers, difficulties of probes application in inhomogeneous plasmas, changes on the probe during exploitation and limited usability in other than the low-temperature plasma conditions [2].

2.4. Light scattering on nanoparticles

The change of the light properties after the interaction with matter is called light scattering. In the case of particle this process consists of borrowing of the energy of the electromagnetic wave propagating in media by the particle and re-radiation of this energy to the solid angle with the vertex in the centre of the particle [20]. In most of cases this process can be described by the wave theory. From the point of view of this theory the electric field of the propagating light wave affects atomic electrons and they become centres of the secondary spherical waves that radiate in all directions.

In media with low level of inhomogeneity the scattering of the light is weak, e.g. the light beam is not visible in a high quality glass or clean water. The light scattering occurs even when linear particles dimensions are smaller than the light wavelength. The basics of the light scattering in a turbid media were experimentally studied by John Tyndall in 1869.

In a case when the media can be considered as continuous the scattering will occur on its optical inhomogeneities. Dielectric permittivity and refraction index of such media is a function of coordinates $\varepsilon = \varepsilon(\vec{r})$ or $n = n(\vec{r})$. The electromagnetic wave in this media consists of the superposition of incident and scattered waves: $\vec{E} = \vec{E}_0 + \vec{E}'$ and $\vec{H} = \vec{H}_0 + \vec{H}'$. For the continuous media the scattering is reduced to diffraction of the waves on inhomogeneities [20–22]. The elastic scattering is characterized by the same wavelength of the scattered light and incident light. An example of inelastic scattering is the *Raman scattering* [23] characterised by usually smaller energy of scattered photons. The *Thomson scattering* [24] is the elastic scattering on free electrons.

For particles characterized by the refractive index n the description of the elastic light scattering depends on the ratio between the wavelength λ and the linear particle dimension d:

1) For the *Rayleigh scattering* [15] approximation the dimensions of the particles are small in comparison with the wavelength: $d \leq (1/15) \cdot \lambda$.
2) The *Mie scattering* [25] is more general and applicable even for $d > (1/15) \cdot \lambda$ but has to be calculated numerically.

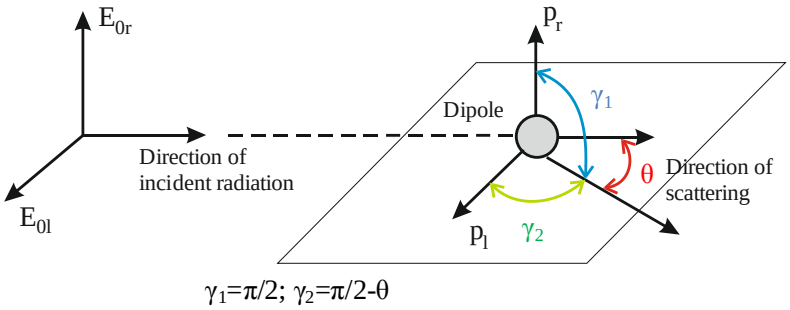

Fig. 2.8. The scheme of the scattering process.

In the *Rayleigh approximation* a small homogeneous spherical particle with size smaller than the wavelength of incident radiation is considered. The electric field $\vec{E}_0$ of the wave is therefore homogeneous across the particle. Let $\vec{p}_0$ be the induced dipole moment of the particle given by the its polarizability α

$$\vec{p}_0 = \alpha \vec{E}_0 . \tag{2.19}$$

In harmonic periodic field with frequency ω of the wave the dipole moment is given in terms of induced dipole moment by

$$\vec{p} = \vec{p}_0 \mathrm{e}^{i\omega t} . \tag{2.20}$$

The electric field created at the large distance r (called far field approximation) by the changing dipole is given by

$$E = \frac{1}{4\pi\varepsilon_0} \frac{\omega}{c^2 r} \frac{\partial p}{\partial t} \sin\gamma , \tag{2.21}$$

where γ is the angle between the scattered dipole moment $\vec{p}_0$ and the direction of observation and thus the electrical field is

$$\vec{E} = -\frac{1}{4\pi\varepsilon_0} \vec{E}_0 \frac{\exp(-ikr)}{r} k^2 \alpha \sin\gamma , \tag{2.22}$$

where $k = 2\pi/\lambda$ is the wave number. Decomposing the electrical vector on two orthogonal components perpendicular and parallel to the plane of scattering (the plane containing incident and scattering beams), we have

$$E_r = -\frac{1}{4\pi\varepsilon_0} E_{0r} \frac{\exp(-ikr)}{r} k^2 \alpha \sin\gamma_1 \tag{2.23}$$

$$E_l = -\frac{1}{4\pi\varepsilon_0} E_{0l} \frac{\exp(-ikr)}{r} k^2 \alpha \sin\gamma_2 . \tag{2.24}$$

Using formula for determination of intensity

$$I = \varepsilon_0 c |E|^2 \tag{2.25}$$

the perpendicular and parallel intensities (or linear polarized intensities) are

$$I_r = \frac{1}{16\pi^2\varepsilon_0^2} \frac{I_{0r} k^4 \alpha^2}{r^2} \tag{2.26}$$

$$I_l = \frac{1}{16\pi^2\varepsilon_0^2} \frac{I_{0l} k^4 \alpha^2}{r^2} \cos^2\theta \tag{2.27}$$

For unpolarised incident beam is $I_{or} = I_{ol} = I_o/2$ and finally

$$I = I_r + I_l = \frac{1}{16\pi^2\varepsilon_0^2} \frac{I_0}{r^2} \alpha^2 \left(\frac{2\pi}{\lambda}\right)^4 \frac{1+\cos^2\theta}{2} . \tag{2.28}$$

From electrostatics the polarizability α of the spherical dielectric particle with the diameter d and the refractive index n is

$$\alpha = 4\pi\varepsilon_0 \left(\frac{d}{2}\right)^3 \frac{n^2-1}{n^2+2} . \tag{2.29}$$

Substituting this in (2.28) we get the Rayleigh formula for unpolarised light intensity [20–22]

$$I = I_0 \frac{1+\cos^2\theta}{2r^2} \left(\frac{2\pi}{\lambda}\right)^4 \left(\frac{n^2-1}{n^2+2}\right)^2 \left(\frac{d}{2}\right)^6 . \tag{2.30}$$

If the incident light is polarized and we observe the scattered light in the plane parallel to $\vec{E}_0$ the polar distribution of scattered intensity can be described as $I \sim \cos^2\theta$. The scattered light intensity in forward and back directions are maximal but to $\theta = 90°$ it is zero since the dipole does not irradiate light along its axis, see red curve in **Fig. 2.9(left)**.

If the scattering of the same polarised light is observed in the plane perpendicular to $\vec{E}_0$, there is no dependence on θ, see black curve in **Fig. 2.9(left)**.

In the unpolarised incident light the vectors $\vec{E}_0$ and so as $\vec{p}_0$ are uniformly distributed in the plane perpendicular to the beam. Therefore all planes of observation that lie in the plane of the beam are equivalent and the angular dependency has the form $(1+\cos^2\theta)/2$, see **Fig. 2.9(right)**.

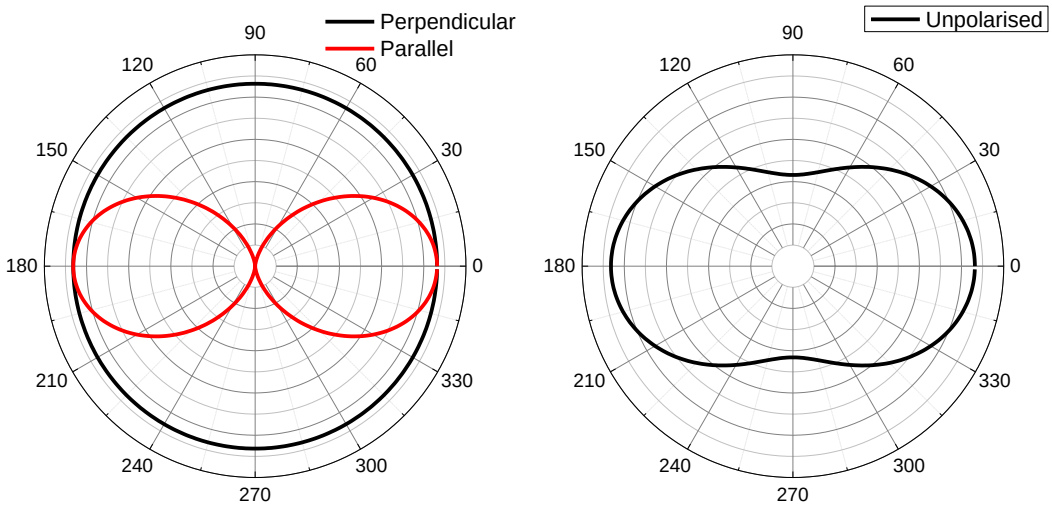

Fig. 2.9. Polar diagrams of the polarized (left) and non-polarized (right) incident light.

The polar diagrams for Rayleigh theory are left to right symmetrical, i.e. scattering intensities are the same in forward and backward directions. This is almost exactly valid for molecules and particles with dimensions less than $0.07\,\lambda$. If dimensions of particles are comparable with the incident light wavelength that symmetry of the scattering polar diagram is lost and the forward scattering becomes dominant.

The theory of the light scattering on spherical particles with dimensions comparable and bigger than the incident light is developed by Gustav Mie in 1908 [26]. Mie scattering can be considered as diffraction on uniform and identical inhomogeneities of the media distributed on the distances larger than the wavelength from each other. The solution of Mie theory is the solution of Maxwell set of equations with the boundary conditions on the surface of the spherical particle with arbitrary radius characterized by ε, μ and σ. The solution is in a form of series with parameter $\alpha = ka$, where a – radius of the spherical particle. The Mie scattering becomes Rayleigh at $\alpha<0.2$.

Differences in Mie and Rayleigh theories are:

1) The reradiation of the primary wave by the elementary scatterers (bound electrons) should be taken into account hence the refractive indexes *n* inside of the particle n≠1.
2) According to Rayleigh theory the radiation of elementary scatterers of the same particle interfere under the same phase shift regardless of the direction. In Mie theory is necessary to take into account the phase shift for elementary scatterers and the phase shift made by the distance between them.

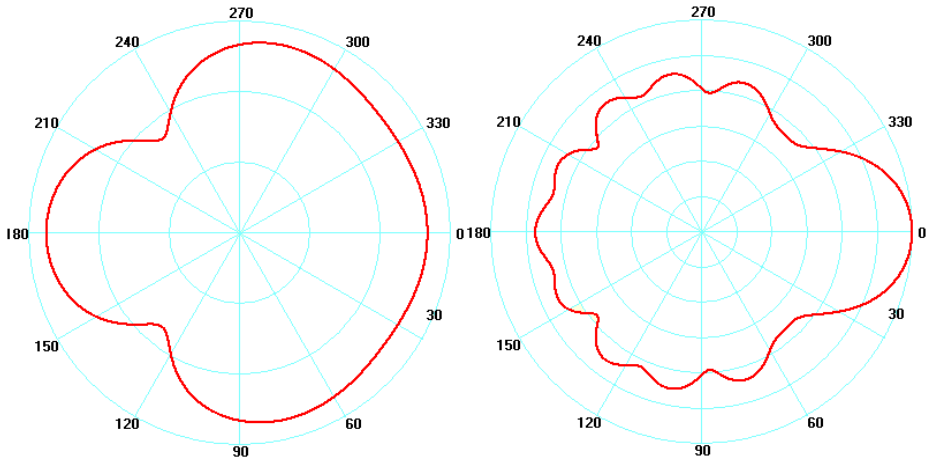

Fig. 2.10. Polar diagram of the scattering intensity on particles with size $\alpha = \lambda/4$ (left) and $\alpha \sim \lambda$ (right) intensity is given in logarithmic scale. Diagrams were calculated by means of software MiePlot [27].

The main results of this difference are following:

1) With increase of α/λ the backward and forward scattering becomes asymmetrical, forward is dominant. The polar diagram for particles with $\alpha=\lambda/4$ is schematically shown in **Fig. 2.10(left)**. A lot of secondary maxima will appear if we continue to increase the particle size **Fig. 2.10(right)**.
2) The dependence on the wavelength is weak for particles with dimensions much larger than the wavelength.
3) The partial polarization of the light is observed.

2.5. Quartz crystal microbalance (QCM)

To take control over the thickness of the films during the deposition onto the sample the quartz crystal microbalance (QCM) can be used. It consists of the quartz

crystal exposed to deposited material. The mass of this material causes a slight decrease of the crystal resonant frequency. From this frequency decrease the film thickness can be estimated. If the thickness varies in a range of nanometres then approximate shift reaches hundreds of Hz hence the quartz crystal might be used in many experiments without cleaning. The initial resonant frequency of unloaded quartz crystal was 5 MHz. To measure the film thickness on the substrate with high accuracy the quartz crystal should be positioned in vacuum chamber as close as possible to the substrate.

In literature there are several formulas to estimate thickness of a film. The first approximation shown below was performed by Sauerbrey [28]:

$$T_f = \left(\frac{N_q d_q}{d_f f_q^2} \right) \left(f_q - f_c \right), \tag{2.31}$$

where T_f is film thickness, d_q the density of quartz (2.60 g/cm^3), d_f density of film, $N_q = f_q \cdot l_q$ is the frequency constant for quartz crystal, l_q the thickness of quartz crystal, f_q the resonant frequency of unplated crystal (5 MHz) and f_c the resonant frequency of crystal loaded by the film. In order to keep the thickness measurement reasonably accurate, frequency shift is limited to about 3 % of f_q. The second generation quartz thickness monitors use better formula

$$T_f = N_q \frac{d_q}{d_f} \left(\frac{1}{f_c} - \frac{1}{f_q} \right), \tag{2.32}$$

which performs good accuracy of measurements for selected materials with frequency shift up to 10 % of f_q.

Miller and Bolef [29]were the first who took into account elastic properties of the thin films. They introduced acoustic impedance ratio Z into formula for thickness computation

$$Z = \sqrt{\frac{d_q \mu_q}{d_f \mu_f}} \tag{2.33}$$

where μ_f and μ_q are shear moduli of deposited film and quartz crystal respectively. The resultant formula

$$T_f = \frac{N_q d_q}{\pi d_f f_c z} \tan\left(Z \tan\left[\frac{\pi \left(f_q - f \right)}{f_q} \right]_c \right) \tag{2.34}$$

is the same as (2.20) if Z=1 or if the deposition material is quartz.

2.6. Dye-sensitized solar cells

In this work we tried to test the efficiency of TiO_2 thin films deposited by means of HCPJ in dye-sensitized solar cells. A dye-sensitized solar cell (DSSC) is a low-cost solar cell belonging to the group of thin film solar cells. It is photo-electro-chemical system based on a semiconductor formed between a photo-sensitized anode and an electrolyte. The modern version of a dye solar cell, also known as the Grätzel cell, was originally co-invented in 1988 by Brian O'Regan and Michael Grätzel at UC Berkeley and this work was later developed by the aforementioned scientists at the École Polytechnique Fédérale de Lausanne until the publication of the first high efficiency DSSC in 1991 [30].

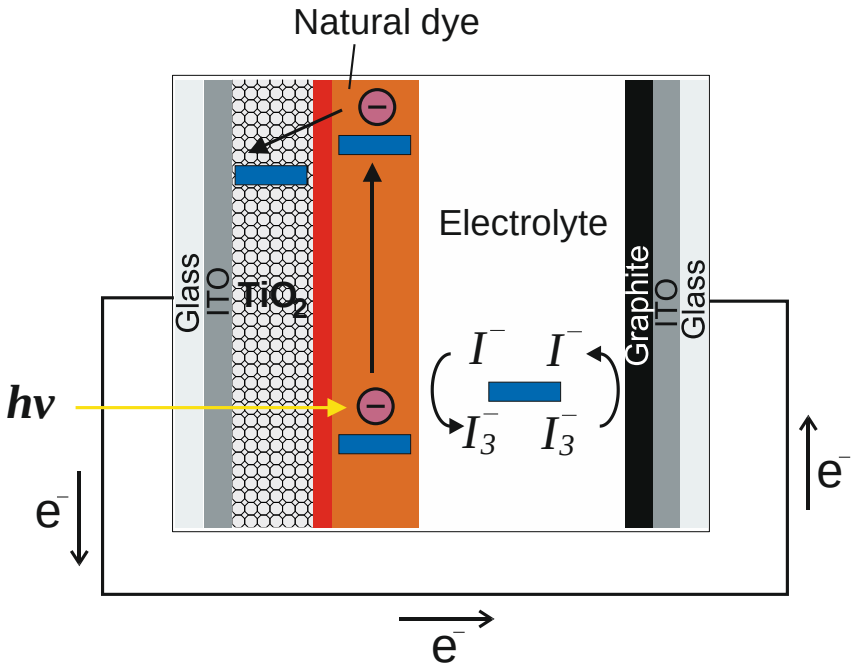

Fig. 2.11. Principal scheme of dye-sensitized solar cell.

Dye-sensitized solar cell has two main functional elements: anode and cathode, see **Fig. 2.11**. Anode is a glass plate with transparent conductive oxide, usually indium-tin oxide (ITO), layer on the top since the main requirements for the electrode are light transparency and conductivity. TiO_2 was deposited on the ITO layer and serves as main active part for production of free charge carriers (electrons). TiO_2 only absorbs a small fraction of the solar photons (those in the UV). Therefore

plate is then immersed in a solution of the photosensitive colourer (photosensitizer) in order to improve the spectral photosensitivity of TiO_2 thin layer. Between electrodes the electrolyte with I^-/I_3^- ions is responsible for the charge transfer. On the cathode electrons have to be transferred back to the electrolyte. To increase the cathode effectivity the thin graphite/Pt film is usually applied to its surface as a catalyst.

The following steps convert photons to current:

1. The incident photon is absorbed on the TiO_2 surface.
2. The photosensitizers are excited from the ground state (S) to the excited state (S^*). The excited electrons are injected into the conduction band of the TiO_2 electrode. This results in the oxidation of the photosensitizer (S^+).

$$S + h\nu \rightarrow S^*$$

$$S^* \rightarrow S^+ + e^- (TiO_2)$$

3. The injected electrons in the conduction band of TiO_2 are transported between TiO_2 nanoparticles via diffusion toward the back contact (ITO). And the electrons finally reach the counter electrode through the circuit.
4. The oxidized photosensitizer (S^+) accepts electrons from the I^- ion leading to regeneration of the ground state (S), and the I^- is oxidized to the oxidized state, I_3^-.

$$S^+ + e^- \rightarrow S$$

5. The oxidized redox mediator, I_3^-, diffuses toward the counter electrode and then it is reduced to I^- ions [31].

$$I_3^- + 2\ e^- \rightarrow 3I^-$$

The efficiency of a DSSC depends on four energy levels of the component: the excited state (approximately HOMO) and the ground state (LUMO) of the photosensitizer, the Fermi level of the TiO_2 electrode and the redox potential of the mediator ($I-/I_3-$) in the electrolyte [31].

The solar cells were tested by means of the light source with defined optic spectrum, typically sun-like, and defined power. The efficiency of solar cells was calculated from the I-V characteristics.

The electric circuit used for the measurement of solar cell I-V characteristic (left) and the explanation of the most important points of characteristic (right) are shown in **Fig. 2.12**. For the fine voltage adjustment the voltage divider with

R1 ≪ R2 was used. For determination of different parameters of solar cell it can be connected to the power supply in reverse bias (dark) regime which is marked as (1) in **Fig. 2.12(left)** and forward bias (illuminated) marked as (2). The conversion efficiency is defined as:

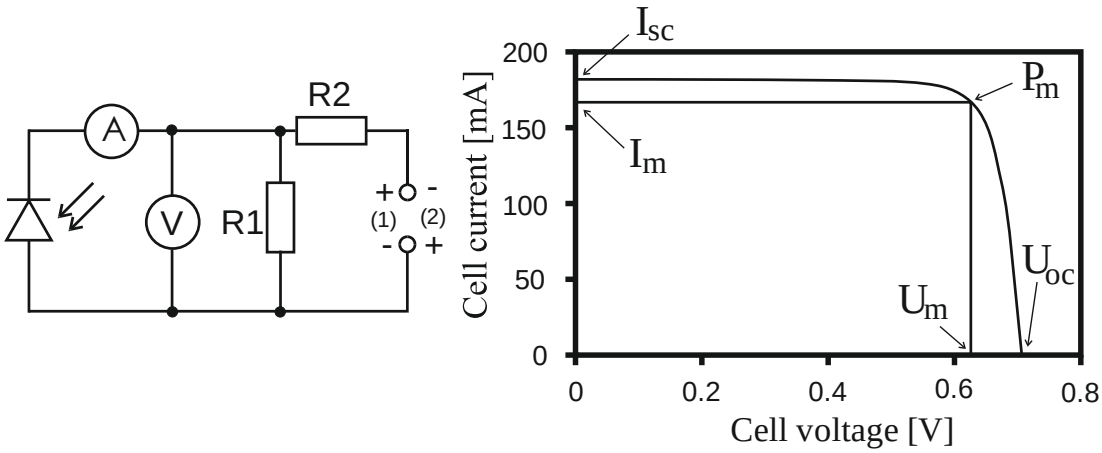

Fig. 2.12. The principal electrical circuit for measurement of I-V characteristic of solar cell (top) and the reversed fourth quadrant of I-V characteristic (bottom).

$$\eta = \frac{P_m}{P_{in}}, \tag{2.35}$$

where P_{in} is the power input to the cell, P_m is the maximum power point which can be determined as $P_m = I_m \cdot U_m$, see **Fig. 2.12(right)**. Another important parameter is the fill factor (FF) that characterizes the inner resistance of a solar cell. It can be expressed by the equation:

$$FF = \frac{I_m U_m}{I_{sc} U_{oc}}, \tag{2.36}$$

where I_{sc} is the short current and U_{oc} is the open circuit voltage. All these parameters can be determined from the cell I-V characteristic.

The reverse bias I-V curve test is performed in the dark between 0 V and the level where breakdown begins to occur (third quadrant). In this region, the slope of the current-voltage characteristic can be used to estimate the shunt resistance.

3. Experimental setup

Experimental measurements were carried out in the laboratory of the low temperature plasma at the Department of Surface and Plasma Science, Faculty of Mathematics and Physics, Charles University in Prague. The experimental system was changed accordingly for the purposes of the measurements (thin film deposition, plasma diagnostics, nanoparticle detection etc.). Cylindrical Langmuir probe was used for plasma diagnostics. Neutral gas temperature was measured by fibre-optic thermometer. Plasma jet in this work was served as nanoparticle source. The process of nanoparticle nucleation was studied by means of laser scattering. Lasers were operated in pulsed mode to improve the signal to noise ratio. Electric connections of laser photodiodes and detector are described.

3.1. Experimental vacuum system

The vacuum system scheme is shown in **Fig. 3.1**. It consists of the vacuum chamber with the diameter of 30 cm and height 30 cm constructed for UHV conditions. We used Ar as a working gas and O_2 as a reactive component for our experiments. Balloons with these gases were connected to the inlets of the main chamber by means Teflon tubes. Flow meters MKS instruments 1259CC-00500SV (maximum 500 sccm for N_2) and MKS instruments MF1 (maximum 10 sccm for N_2) were used for control of the Ar and O_2 flow rate respectively. The operation of flow meters was provided by MKS multi gas flow controller 157. Valve system allows us to drive the flow of gases to the different inlets in the main chamber. In experiments with the pure Ar it was introduced directly to the hollow cathode. In a case of reactive sputtering the oxygen was introduced through the separate inlet in a main chamber because introducing it to hollow cathode results in discharge instabilities like sparks, change of the glow regime and rapid increase of the voltage.

Three vacuum gauges are installed in a vacuum system to monitor the pressure. Pirani gauge was used for monitoring the pressure between primary and secondary pumps. Primary vacuum in a main chamber was achieved by Leybold Oerlikon EcoDry M15 dry piston vacuum pump.

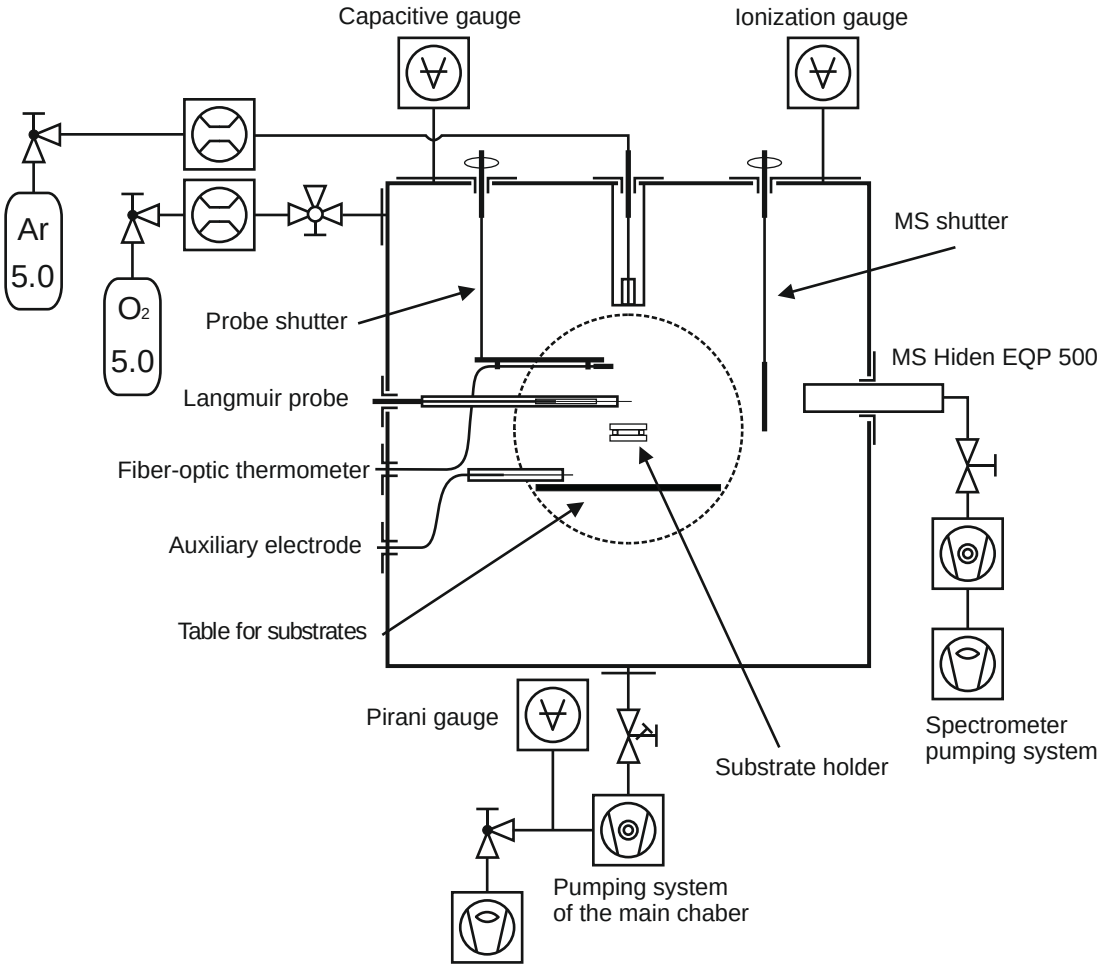

Fig. 3.1. Principal vacuum scheme of the system with basic function parts.

Although the minimal pressure in the main chamber was in order of 10^{-6} Pa we used higher values in our experiments since the purity of Ar is 99.999 % and pumping of the system down to the pressure lesser than 10^{-4} Pa makes a minor contribution in a purity of the experimental conditions. The achievement of the oil free high vacuum conditions we provided by means of turbomolecular pump Pfeiffer Vacuum TMU 521 P. The maximal pumping speed was 500 l/s for Ar. Two vacuum gauges were installed in a main chamber. During the experiments the pressure was measured by means of capacitive gauge Pfeiffer Vacuum CMR 263. Combined vacuum gauge Pfeiffer Vacuum PBR 260 with measuring range 10^{-8} – 10^{5} Pa consisting of Pirani and ionization vacuum gauges was used for the monitoring of the pressure during pumping before experiments with plasma.

The hollow cathode plasma jet (HCPJ) was vertically mounted at the top of the vacuum system. The manipulation with vertical position of HCPJ was provided by edge welded below with thread mechanism. This allowed changing the vertical

position along its axis in the range of 10 cm. Vacuum system was equipped with quadrupole mass spectrometer (MS) Hiden EQP-500. The spectrometer chamber is connected to the main chamber through the small orifice (20 μm diameter). Mass spectrometer chamber was pumped by means of primary and turbomolecular pumps even when mass spectrometer wasn't used in experiments.

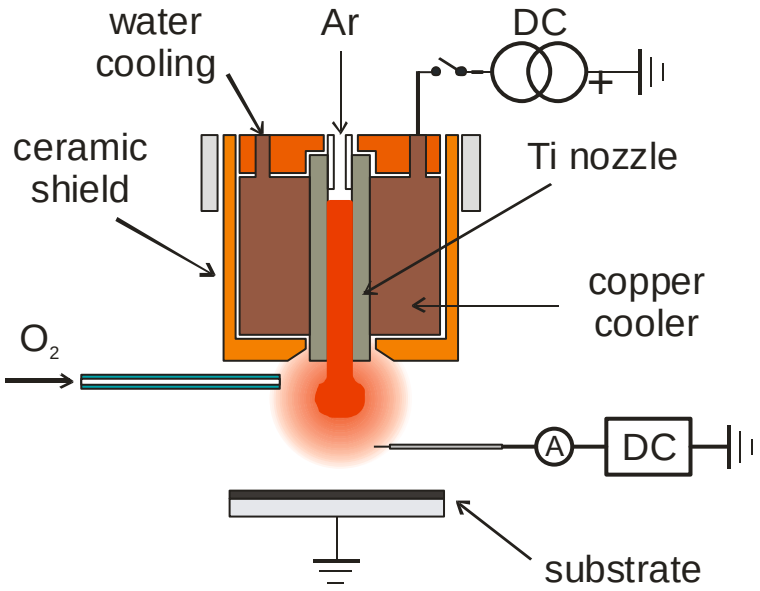

Fig. 3.2. Process of the deposition by means of hollow cathode plasma jet in DC regime and Langmuir probe electrical connection.

For the effective manipulation with samples we used the load-lock system. It consisted of the buffer chamber, forked rod and sample holder. Load-lock system gives an opportunity to insert and extract samples without venting of the vacuum system. Reload of the samples took approximately 20 minutes.

The scheme of the HCPJ is shown in **Fig. 3.2**. The main part is the cylindrical pure titanium (99.995 %) hollow cathode. The cathode has tubular shape with length of 30 mm, outer diameter 8 mm and inner diameter 6 mm. The cathode is tightened between two water cooled copper blocks. The copper tubes for the cooling water are electrically isolated from the chamber and serve also as the electric connection. HCPJ was powered by means of DC power supply Advanced Energy MDX 500 which provided maximum values of power, current and voltage of 500 W, 500 mA and 1.2 kV respectively. The 25 Ω resistor was connected in series with plasma jet. HCPJ was insulated from the vacuum system by means of ceramic tubes and shield.

The vacuum chamber and metal parts inside of it were grounded and served as anode. We faced the problems with discharge stability in a case of reactive sputtering

with introduction of oxygen into the main chamber. It was caused by covering of the inner surface of the chamber by nonconductive TiO_2 layer that resulted in a problem with charge outflow. Some small metal parts of the chamber (screws, shutters or table) became localized anode with a small collecting surface and high current density. The conductivity was provided by continuous heating and removal of the oxide layer by means of electron and negative ion current. It resulted in erosion of arbitrary metal parts and unstable regime of discharge glow. This problem was solved by mounting auxiliary electrode with the potential of +18 V with respect to the ground which drained the almost whole current from the cathode.

3.2. Langmuir probe measurements

A tungsten cylindrical Langmuir probe is used for plasma diagnostics in HCPJ. The schematic drawing of the probe is shown in **Fig. 3.3**. The active part of the probe, which was in contact with plasma, is a thin wire with diameter of $2r_p$ = 50 μm and the length of l_p = 2.2 mm. Tungsten was chosen since it has a high melting point and relatively weak chemical activity at low temperature. The probe was connected through the copper wire to the measuring electrical circuit. The probe insulation was provided by the ceramic tube. Near the probe tip the thinner centring tube inserted into a thicker one was added and shifted from the face of the tube to the distance of about 1 mm inside of the bigger one. This was done to avoid the possible contact of the probe wire with the outer tube surface. This surface becomes conductive during the deposition and its contact with probe would make the probe collecting surface undefined. The probe tip was cleaned by heating it with electron current before taking several probe characteristics. The heating current was limited to several mA in order not to overheat the probe.

The probe was mounted from the side of the main chamber perpendicularly to the axis of the HCPJ. The movable feedthrough allowed the horizontal manipulation with the probe in a range of 15 cm. Under the assumption of the axial symmetry and together with vertical hollow cathode movement this makes possible to measure the complete profiles of plasma parameters.

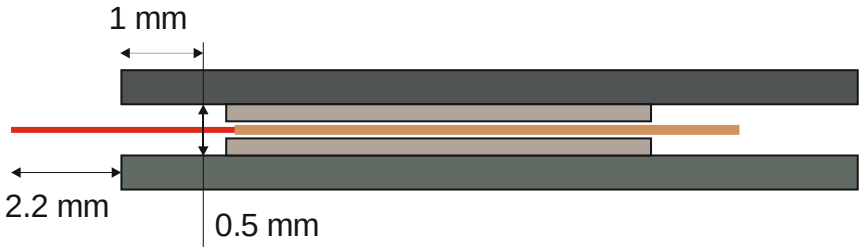

Fig. 3.3. The schematic drawing of the Langmuir probe. The probe is highlighted by the red colour.

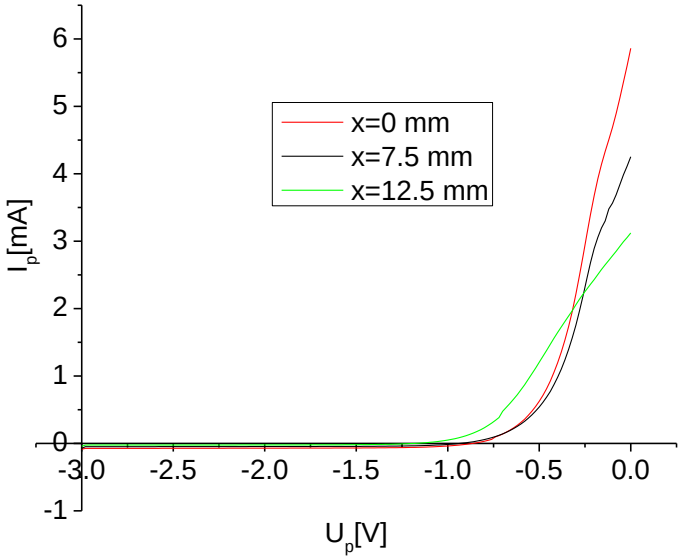

Fig. 3.4. Examples of the probe characteristics measured at the different horizontal position.

The automation of the manipulation process was achieved by step motor connected to the driving system Micron CD40x with integrated microcontroller and high power amplifier with pulsed regulation. Step motor was operated by means of program written in Agilent VEE environment and connected to PC via serial port. This makes possible fast and accurate adjustment of the probe position.

The Langmuir probe current was measured by the multimeter Siemens B 3220 and the voltage was adjusted by Siemens B 3050 calibrator. Both devices were connecter to PC via GPIB interface and operated by means of software written in Agilent VEE. It gives an opportunity to change the voltage step and number of averages of each measured point. Measured data were stored in "*.dat" format with probe voltage in a first column and probe current in a second. Measured data was processed by means of program START [32]. The examples of probe characteristics are given in **Fig. 3.4**.

3.3. Measurement of neutral gas temperature by fibre-optic thermometer

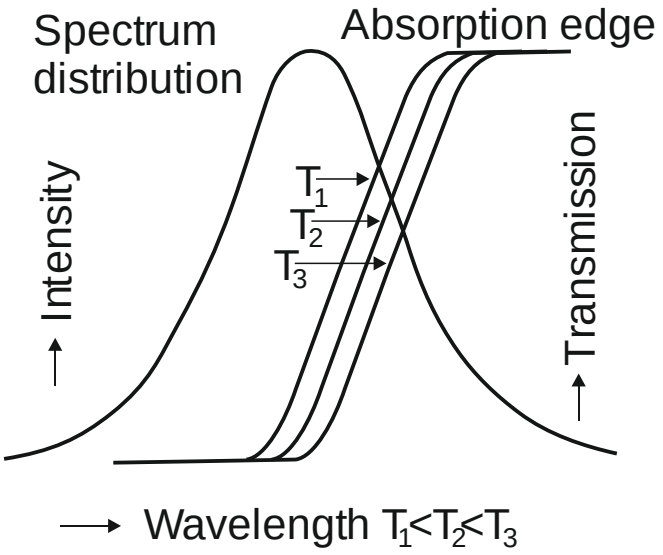

Fig. 3.5. Basic principle of the fiber-optic thermometer [33].

The neutral gas temperature is one of important parameters that determine the processes in a hollow cathode discharge plasma, e.g. the growth of nanoparticles or the thin film crystal structure. It is especially advantageous to measure the temperature in the active plasma discharge using modern device – the fibre-optic thermometer – since its sensor is nonconductive. The working principle is shown in **Fig. 3.5**. The energy bandgap of most kinds of semiconductors decreases almost linearly with the increasing temperature T near the room temperature. Hence, the wavelength $\lambda_g(T)$ corresponding to their optical absorption edge shifts towards longer wavelength with T. As shown in **Fig. 3.5**, when we employ a light source of a LED with a radiation spectrum coincident with $\lambda_g(T)$ of the selected semiconductor, the intensity of the light transmitted through the semiconductor decreases with T [33].

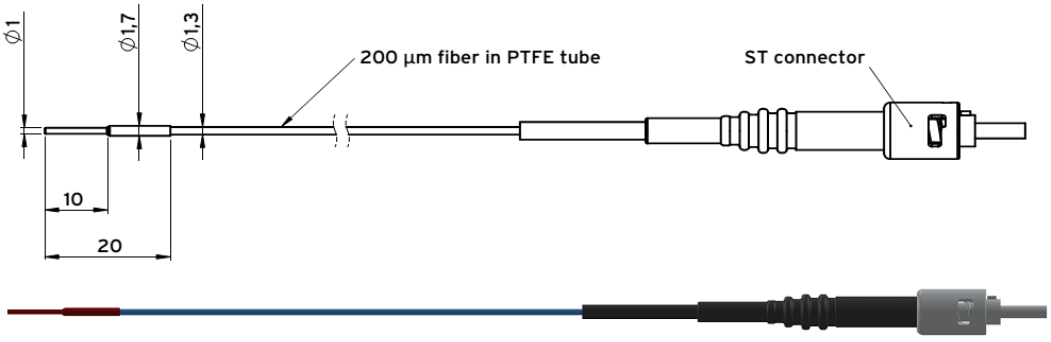

Fig. 3.6. The construction of fibre-optic temperature sensor TS2. Dimensions are given in mm.

We used the commercial measuring device Optocon FOTEMP1 equipped with fibre optic sensor Optocon TS2. The scheme of the sensor is shown in **Fig. 3.6**. Its functional part is GaAs (Gallium arsenide) crystal. This semiconductor has direct band gap, which means that it can absorb and emit light with high efficiency. Starting at the wavelength of 850 nm GaAs becomes optical translucent. The position of the band gap shifts about 0.4 nm/K. The excellent chemical resistance is achieved by the teflon jacket. GaAs crystal is attached to PTFE protected glass fiber (1mm Ø) with the ST-connector in the end. Sensor TS2 has a response time of 2 s. With an accuracy of ± 0.2 °C it allows precise and repeatable measurements. The FOTEMP 1 has a measuring range from -200 °C to +300 °C which is determined by the accuracy of the theory and used materials (The melting point of teflon is about 310 ºC). Temperature range is sufficient for the majority of experimental conditions except of the measurements when plasma jet is operated under the high values of the discharge current, i.e. at currents over 400 mA.

The probe was attached to the horizontal part of the probe shutter (**Fig. 3.1**) and the signal was brought out via the optical feedthrough. The probe shutter is movable hence we were able to measure the horizontal temperature profiles. The position of the probe was determined by the rotation angle of the shutter. Then it was recalculated in linear shift since the distance from the tip of the probe to the axis of rotation was known. The monitoring system is equipped with by the light source and simple optical spectrometer which measures the band gap shift according to the reflected light from the GaAs crystal sensor.

The most valuable advantages of the fibre-optic thermometer concerning measurements in plasma are that it is unaffected by the electromagnetic (EMI) or radio frequency interference (RFI), it is small to measure locally and can be exploited in a chemically aggressive environment.

3.4. Detection of nanoparticles using laser beam scattering

Nanoparticles nucleation in a gas phase was investigated by means of the light scattering technique. The principal scheme of the experiment is shown in **Fig. 3.7**. The laser beam horizontally passed the vacuum chamber below the nozzle where it crossed the vertical axis of the system and then it was reflected by the mirror away of

the visibility of the detectors in order to be dumped. The detector optics was focused to the cross of the laser beam and the system axis. There is shown the angle θ between the incident light, i.e. laser beam, and the light scattered to the detector optics.

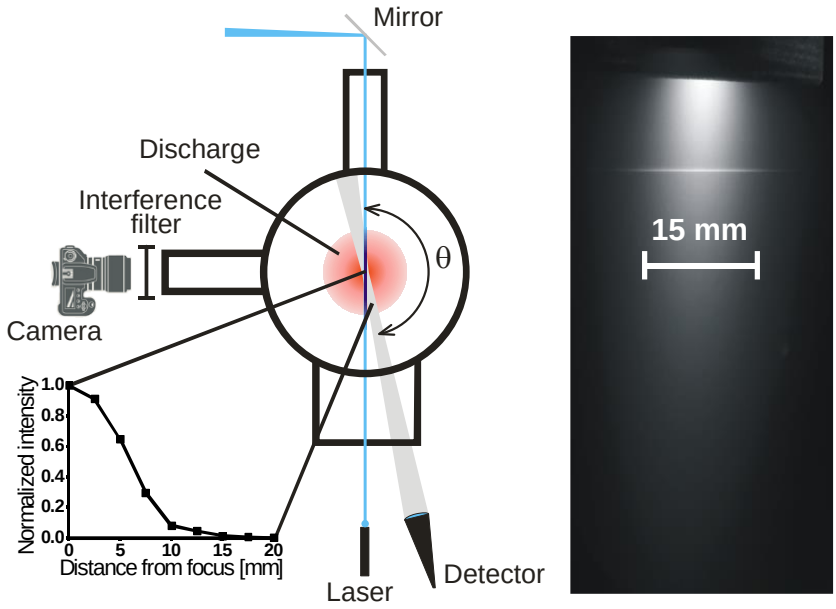

Fig. 3.7. Top view of the experimental set up for detection of nanoparticles based on laser-light scattering (left). Given graph indicates the dimension of measuring volume (maximum is at the plasma axis). Distance from the detector to plasma axis is 61 cm. Grayscale photo of the plasma jet with the scattered laser beam taken through the blue interference filter (right).

The scattered light was collected and focused by the lens with diameter of 24 mm to the 0.6 mm diameter optical fibre P600-2-SR. The proper focusing of the detector optics to the HCPJ axis was carried out by additional laser placed at the photodiode position at the end of the optic fibre. The graph in the left part of the figure describes sensitivity of the detector on the distance from the focus.

There were used two detector types at the end of the fibre: the photodiode or the optical spectrometer Ocean Optics HR4000. The third detector was photo camera Nikon 5100D with AF-S DX Nikkor 18–55 mm f/3.5–5.6G VR objective lenses. For measurement of 2D intensity distribution profiles the photographs were processed using Photoshop CS6 and Origin 8.5.

To support both laser and detectors the geodesic tripod and HAMA Star 63 tripods were used. Laser was movable in both vertical and horizontal directions using linear shifts. This allowed the accurate adjustment of the laser position in experiments with digital photo camera.

We used three laser diodes with wavelength 446, 632 and 661 nm. Laser diode with wavelength 632 nm was used in our early experiments.

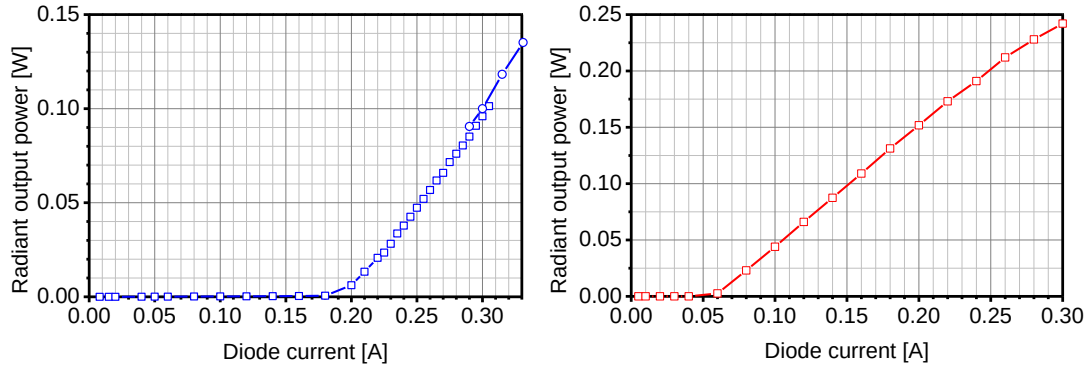

Fig. 3.8. Measured dependencies of radiant output power on laser diode current for blue (left, 446 nm) and red (right, 632 nm) laser photodiodes used for nanoparticle detection.

Since we did not know the type of laser diodes we measured the dependencies of radiant output power on the diode current for blue and red laser diode as shown in **Fig. 3.8**. The blue laser diode was constructed to operate at higher values of diode current. Moreover, the technique of the light scattering is more sensitive to the shorter wavelengths; because of this we used mostly blue laser in our experiments.

Spectral profiles of the blue laser intensity and the blue interference filter (IF) transmittance are shown in **Fig. 3.9**. The measurements were carried out by means of the low-resolution optical spectrometer Ocean Optics HR4000. The laser peak position is 446 nm while the peak position of the IF is shifted by about 4 nm. The full width at 50 % of maximum intensity (FWHM) of approx. 10 nm for both peaks ensures still good signal corresponding to the overlap of both peaks while suppressing the out of band wavelengths at the detector.

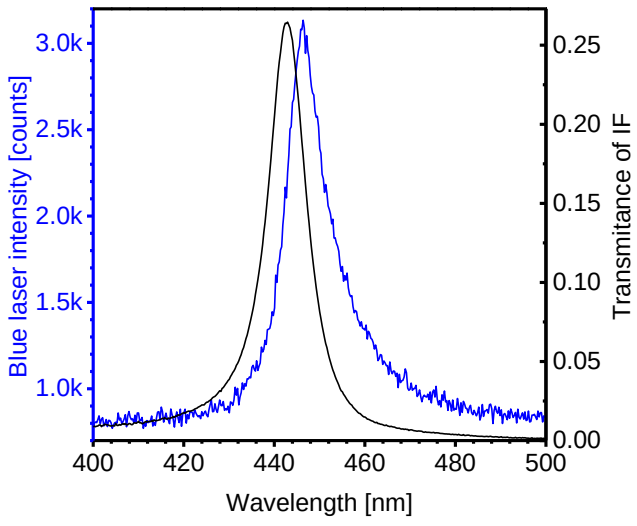

Fig. 3.9. Optical spectrum of the blue laser (blue) and spectral bandwidth of interference fiter.

Laser diodes were calibrated by means of Thorlabs PM100D power meter in combination with Thorlabs S121C detector. Its sensitivity is

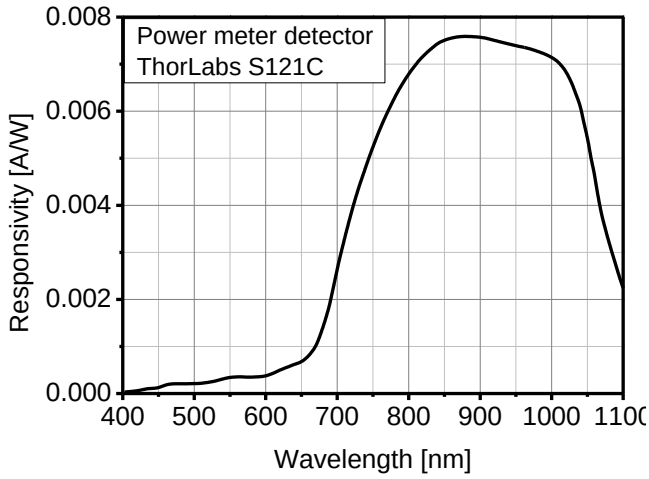

Fig. 3.10. Optical sensitivity of the detector we used for calibration of blue and red lasers.

shown in **Fig. 3.10**. Although the sensitivity at blue (446 nm) and early red (632 nm) wavelengths is low the manufacturer specified 5 % tolerance. This device was also used for the radiant power control of laser diodes during experiments since the laser diodes are sensitive to the temperature change. During the operation the laser diodes were actively cooled by fan.

For the scattered laser light detection the Siemens BPW 34 photodiode was used. Its photosensitive area was $2.65 \cdot 2.65\ \mathrm{mm}^2$ and the spectral sensitivity is shown in **Fig. 3.11**. The maximum sensitivity is in a range of wavelengths 800–900 nm. The sensitivity at wavelengths 446 nm and 661 nm drops down to 25 % and 70 % of its maximum respectively.

The photodiode was negatively biased to III-rd quadrant and AC connected to the operational-amplifier-based current-voltage converter, see **Fig. 3.12**. The resistor and capacitor in its feedback formed 2 kHz low-pass filter. The signal was then connected via the 600 Hz passive RC high-pass filter to narrow-band (40 dB/octave) amplifier (Unipan, Selective nanovoltmeter 237) tuned to laser modulation frequency of 1 kHz. The signal was then visualized on the oscilloscope and its value measured peak-to-peak in mV.

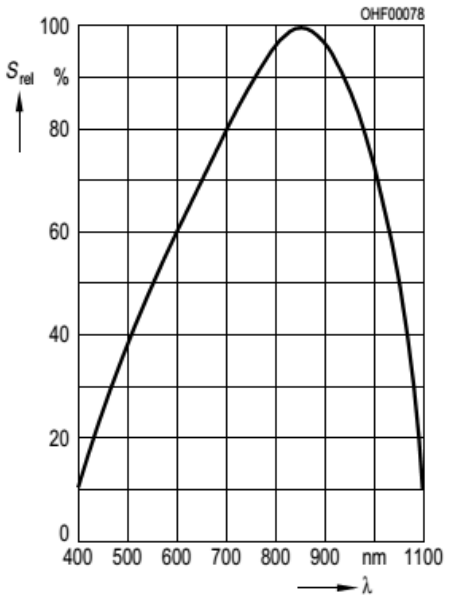

Fig. 3.11. The spectral sensitivity of the photodiode Siemens BPW 34.

Laser was modulated at the frequency of 1 kHz for the filtration of the noise, especially at the mains frequency of 50 Hz and its harmonics, and the stray light at the detector. The electrical scheme of the laser diode driver is shown in **Fig. 3.13**. The laser diode current

amplitude was controlled by changing the supply voltage.

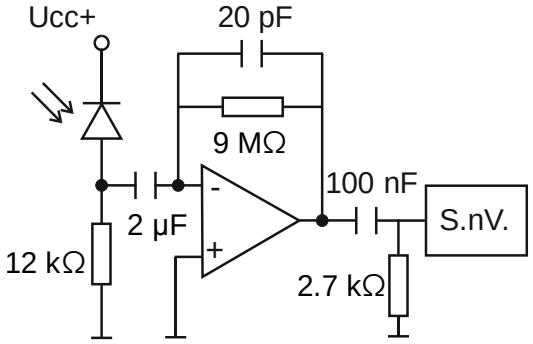

Fig. 3.12. Photodiode signal amplifier connected to the selective nanovoltmeter (S.nV.) and the scope.

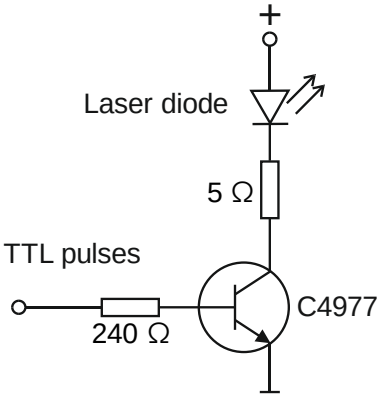

Fig. 3.13. Electrical connection of laser photodiode for pulsed modulation.

4. Deposition of titanium dioxide nanoparticles by means of HCPJ

The presence of the "heavy" nanoparticles that consist of more than thousands of atoms can dramatically affect the plasma. Nanoparticles serve as a charge carriers with both positive and negative sign. The positive charge can be created by the secondary emission caused by the positive ions bombardment. The negative charge of nanoparticles is more natural in plasma out of the cathode region since electrons have much higher mobility hence particles collect electrons until they reach floating potential.

Generally particles with a size ranging from units up to hundreds of nm are called nanoparticles. The application of nanoparticles is growing rapidly in nanoscale science and engineering. Such properties of nanoparticles as surface to volume ratio, quantum confinement, and surface atom arrangement are of great importance. New properties of the materials can be obtained by controlling the size of nanoparticles.

In recent years a number of techniques for nanoparticle synthesis have been developed. The most widespread techniques of gas-phase nanoparticle synthesis using we should mention: pulsed laser ablation, spark discharge generation, inert gas condensation and ion sputtering. Gas-phase methods are based on achieving the gas supersaturation necessary to start the nucleation of nanoparticles [34,35]. Supersaturation in HCPJ is achieved by conditions of the high deposition rate and strong pressure gradient between nozzle and substrate. A review on plasma nanofabrication can be found in [36]. Different materials can be deposited by various plasma jet systems, e.g. ZnO [37], WO [38] or Fe [39]. TiO_2 nanoparticles have applications in different fields of technology because of their photocatalytic properties (tested by e.g. dye decomposition [40]), high chemical resistance and stability. Examples of their application are found in biomedical research [41], treatment of wastewater [42] and pesticide degradation [43]. Nanoparticles of TiO_2 dissociate the water molecule to produce hydrogen. The TiO_2 is used for dye production in industry because of its "pure" white colour [44]. Colourers that contain this material are not dangerous for human health hence it is widely used in food industry. The production of dye-sensitized solar cells with positive electrode covered by TiO_2 layer was investigated e.g. in this work.

The crystalline structure of TiO_2 has three polymorphs: anatase (tetragonal), rutile (tetragonal), and brookite (orthorhombic). The investigation of anatase photocatalytic activity is of great interest for reduction of organic compounds and molecular gases [45]. Experiments have shown that using TiO_2 as a photocatalyst in the form of nanoparticles is more effective than bulk material because of the high effective surface area [44]. The information about crystalline structure is present in section 5.

One of advantages of the low pressure HCPJ is the possibility to use the DC discharge, which is simpler with respect to RF. HCPJ can be utilized in wide range of pressures: from low (0.1 Pa) up to atmospheric pressure [46]. The use of HCPJ for nanoparticle deposition is based on sputtering the material from the inner cathode surface by ions which gain energy from the cathode fall. In comparison with the more commonly used magnetron sputtering it has some significant advantages in the production of nanoparticles. The space inside the hollow cathode with its heightened pressure serves as a space for nanoparticle nucleation. To achieve this with a magnetron an aggregation chamber provided by differential pumping is necessary [12]. Moreover, the velocity of a working buffer gas can be adjusted via its flow rate [47,48]. This affects the resident time of nanoparticles inside and outside of the hollow cathode and, consequently, influences the size of the nanoparticles deposited on the substrate. The deposition mechanism by means of HCPJ is covered in more detail in [1,49].

This section describes our investigation of the relationship between the inhomogeneous parameters of the plasma plume generated by HCPJ and the properties of the nanomaterial deposited onto the substrate. Similar conditions were used in [39] for the deposition of Fe nanoparticles. The processes of nanoparticle by means of similar system were partially explained (relevant cathode geometry, flow rates and pressure). In our section of dissertation thesis we studied the distribution of nanoparticles on the substrate and added plasma diagnostics which is important since the nanoparticle growth occurs in the plasma. The stress is focused on conditions favourable for the formation and growth of nanoparticles before reaching the substrate.

4.1. Langmuir probe diagnostics of plasma plume under conditions relevant to deposition

When the formation of nanoparticles occurs in a gas phase, information about plasma is of great importance. Experimental conditions were close to those we used during the deposition of thin layers (turbulent regime of the plasma flow). Probe diagnostics of the plasma jet in a laminar regime of the flow was described in details in [50]. The aim of these measurements was to evaluate the influence of the plasma plume on the deposition since the samples were in a direct contact with plasma.

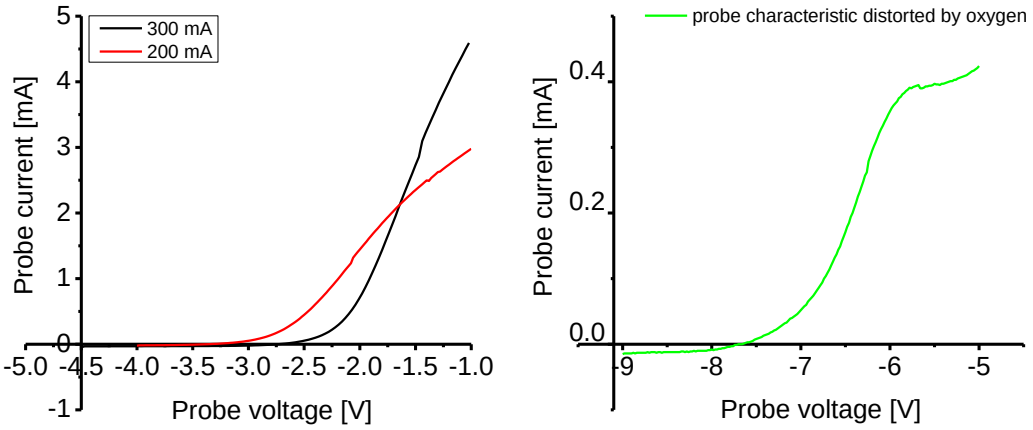

Fig. 4.1. Probe characteristics measured at the plasma plume axis at the pressure 100 Pa and the argon flow 200 sccm (left). Probe characteristic distorted by the probe oxidation (right).

Typical probe characteristics are shown in **Fig. 4.1**. The voltage step was 0.02 V and each point was averaged in order to reduce the noise caused by plasma fluctuations. The probe was positioned at the approximate position where the sample is located during the deposition. For the electron temperature T_e evaluation the Maxwellian EEDF f_{Max} was assumed

$$f_{Max}(eU) \propto \sqrt{eU}\,\exp\frac{-e(U_p - U_{sp})}{k_b T_e} \tag{4.1}$$

$$\frac{\mathrm{d}^2 I_p(U)}{\mathrm{d}U_p^2} = \frac{e^3 n_e S}{4}\sqrt{\frac{2}{m_e}}\sqrt{\frac{1}{eU_p}}\,f_{Max}(eU_p)\,. \tag{4.2}$$

The electron temperature T_e was calculated from the slope of the second derivative I-V characteristics in the semi logarithmic scale. The electron density was estimated: (i) from the integral of the second derivative of current-voltage characteristics equation (4.2) denoted as "*NeInt*" in **Fig. 4.2**, (ii) from the electron current at the plasma potential $I(U_{sp})$ denoted *NeVpl* and (iii) from the slope of the plot $I_e^2(U)$

denoted *NeIeSqr*. Three methods were used to assess the error of the electron density measurement.

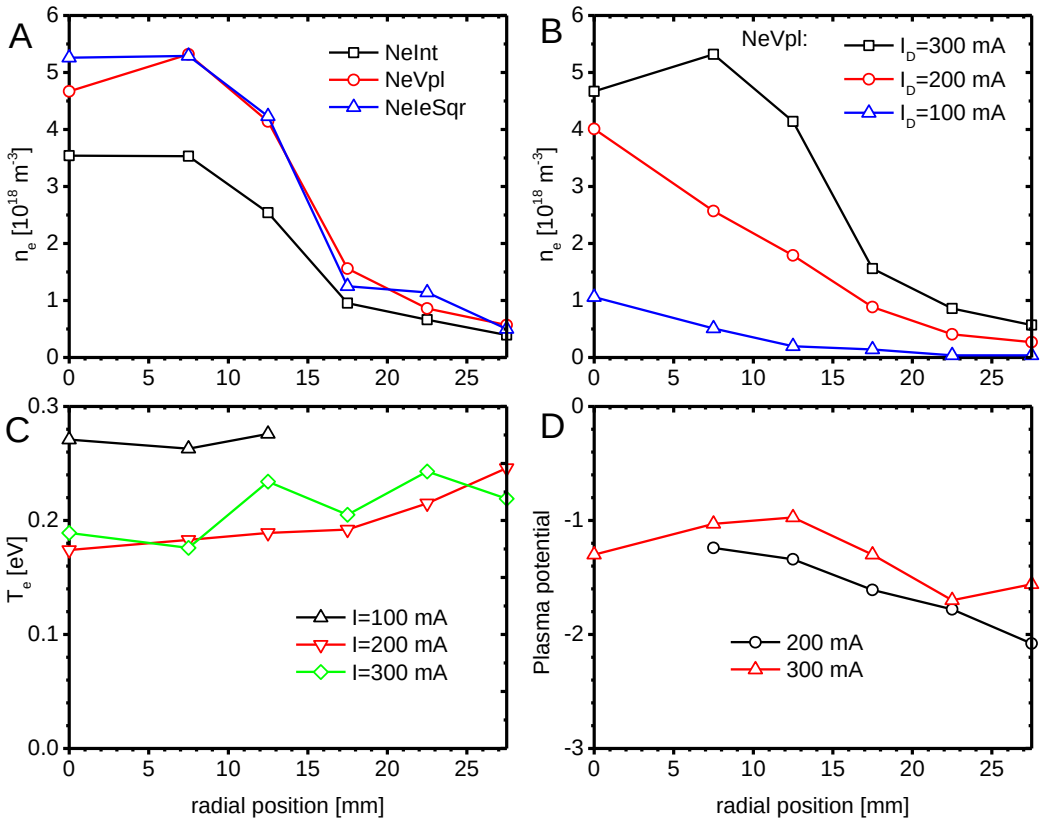

Fig. 4.2. Dependences of electron density, electron temperature and plasma potential on the distance between probe and discharge axis at a vertical position h=42 mm below the cathode outlet. The electron density (a) calculated by three different methods at I_d=300 mA and (b) NeVpl for different values of discharge current. Dependencies of electron temperature (c) and plasma potential (d) on the probe radial position. The values of pressure and argon flow rate were 100 Pa and 200 sccm, respectively.

The dependences of electron density on the radial position of the probe are shown in **Fig. 4.2(a,b)**. The comparison of the three different methods is presented in **Fig. 4.2(a)**. The density from integration of the second derivative of I-V characteristics shows, as expected, somewhat lower values of plasma density because of the error in the second derivative caused by the numerical differentiation near the U_{sp}. The method *NeIeSqr* assumes the thick sheath. Closer to the axis, i.e. at higher plasma densities the λ_D becomes smaller, which is associated with higher error. Nevertheless, it is seen from **Fig. 4.2(a)** that the $I_e^2(U_p)$ method agrees well with the $I_e(U_{sp})$. In **Fig. 4.2(b)** electron density dependences on the radial position under different discharge currents are shown. Here, the n_e is calculated from $I_e(U_{sp})$. It is

evident, especially from the dependence that corresponds to discharge current 300 mA, that plasma has a well-defined border approximately at a distance of 15 mm from the discharge axis. Outside of this border the ionization level falls dramatically.

The electron temperature and plasma potential stay almost independent on the radial probe position, see **Fig. 4.2(c,d)**. The values of pressure and argon flow rate were 100 Pa and 200 sccm, respectively. The values of the electron temperature for the discharge currents 100, 200, 300 mA are 0.27, 0.21, 0.2 eV, respectively. The low electron temperature is typical for this discharge type because almost the whole cathode fall is located inside or in the vicinity of the cathode. These values are in agreement with [47] and [51], but in the second reference much higher oxygen to argon ratios were used. The plasma potential is slightly negative when the probe is used in pure argon as in [47,51]. The negative value of the plasma potential can be explained by the low radial diffusion to the chamber walls at the working pressure of 100 Pa and the low electron temperature. This leads to the confinement of the discharge channel that carries the discharge current mostly to the substrate holder, causing the role of chamber walls as the anode to be nearly unimportant.

The measurements were performed without the oxygen flow. Even the smallest oxygen flow rate (0.1 sccm) causes a rapid oxidation of the tungsten Langmuir probe surface, after which the probe loses its conductivity and its further use becomes impossible until it is cleaned by an electron bombardment in pure argon. Oxidized probe is characterized by continuously growing absolute value of the floating potential which has a negative sign and distorted probe characteristic (low values of current). This effect is caused by accumulation of the electrons on the surface of the probe due to the problem with charge outflow, see **Fig. 4.1**.

4.2. Neutral gas temperature measurements by fibre-optic thermometer

The principle of this thermometer is described in section 2.3. Unfortunately, it cannot be used in all possible regimes of HCPJ due to the upper temperature limit of 300 ºC. Especially, the region below the nozzle and the high discharge currents are important for thin film deposition and annealing mechanisms but at these conditions the temperatures above the thermometer limit can be overcome.

Two HCPJ flow regimes can be distinguished: laminar and turbulent. First regime is characterized by the short spherical shape of the plasma jet with radius 1 to 4 cm. This regime, where the plasma diffuses in all directions, occurs at low values of pressure (1–20 Pa) and working gas flow rate about 100 sccm.

The second regime of plasma at pressure 50 Pa and more and the flow over approximately 100 sccm has shape of the oblong torch. The dimensions of the torch depend on the pressure and flow rate. The length of the plasma plume is more than several tens of cm at the argon flow rate of about 300 sccm. The motion of plasma in flow direction becomes dominant in comparison with radial diffusion. The transition between these two regimes is continuous.

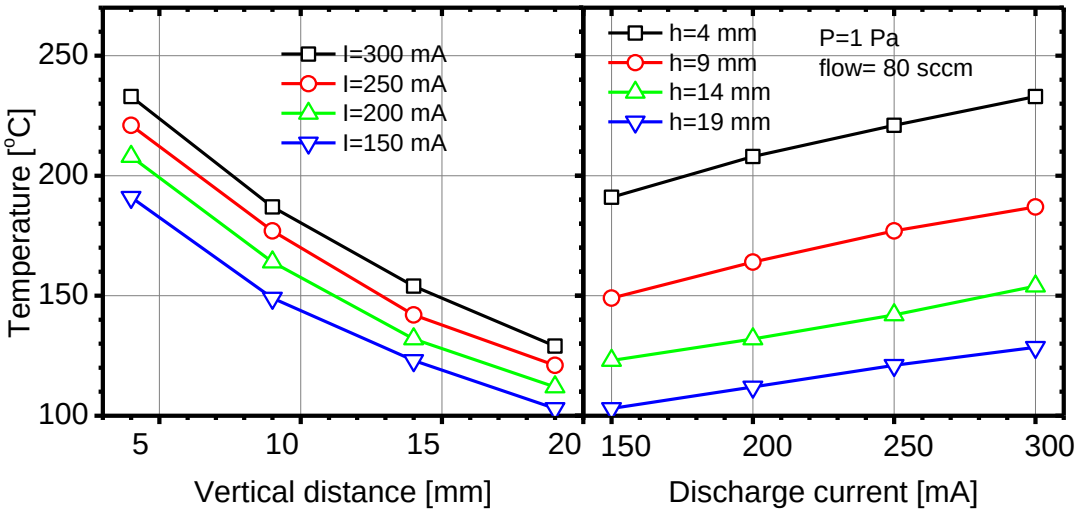

Fig. 4.3. Temperature measurements at the plasma plume axis in laminar regime of the gas flow. The dependences of the temperature on the discharge current *I* (right) and temperature on the vertical distance *h* from the nozzle (left).

The temperature measurements in laminar regime of the flow are shown in **Fig. 4.3**. The measurement was performed at the plasma axis where the maximum of the radial temperature distribution is considered. The dependences of the temperature on the discharge current perform show approximately linear growth. Dependences of the temperature on the vertical position show convex decrease with the maximum near the cathode nozzle. This regime is characterized by the low ionization and fast thermalization of neutral argon atoms. Thus the plasma annealing is not assumed at these conditions even at positions close to the nozzle.

The pressure increase in the discharge chamber leads to the increase of the temperature of the plasma plume as shown in **Fig. 4.4(left)**. This effect is caused by

the lower gas velocity at the higher pressure since the time of flight of argon atoms through the hot discharge region is shorter and energy transfer between discharge and working gas is reduced. Temperature profiles of the laminar gas flow regime at the pressure 1.2 and 11.7 Pa are shown in **Fig. 4.3(right)**. Profiles are characterized by dramatic fall near the proximity of the plasma axis. The temperature gradient is approximately 8 ºC/cm. The tail of the profiles is flat and at the distance of 40 mm from the axis temperature is slightly above the room temperature.

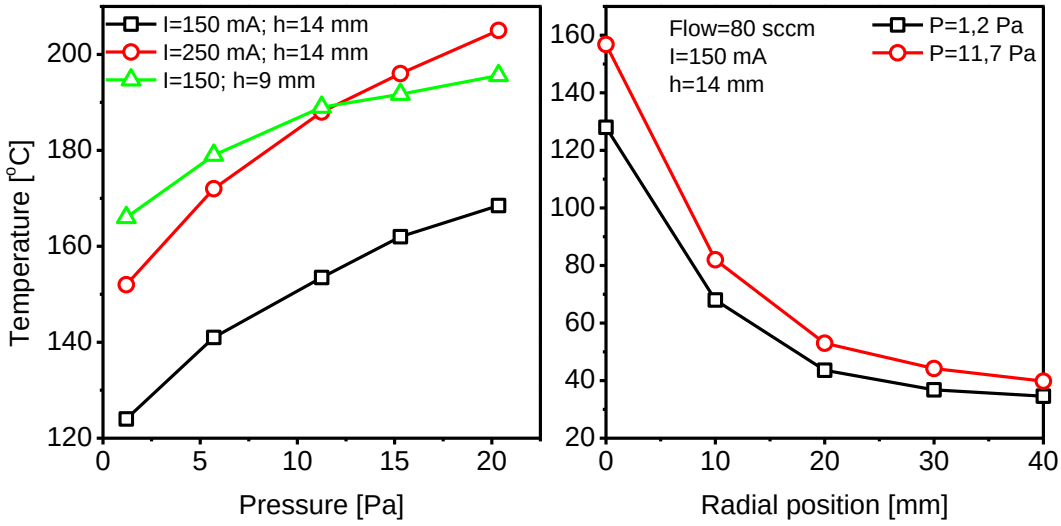

Fig. 4.4. Dependencies of the neutral gas temperature on pressure (left) and radial position (right).

The turbulent regime of the flow is more interesting since the stable and effective deposition of nanoparticles was achieved at this regime. Measurements were carried out with introduction of 0.5 sccm of oxygen to the main chamber. Such conditions completely correspond to the nanoparticles deposition conditions.

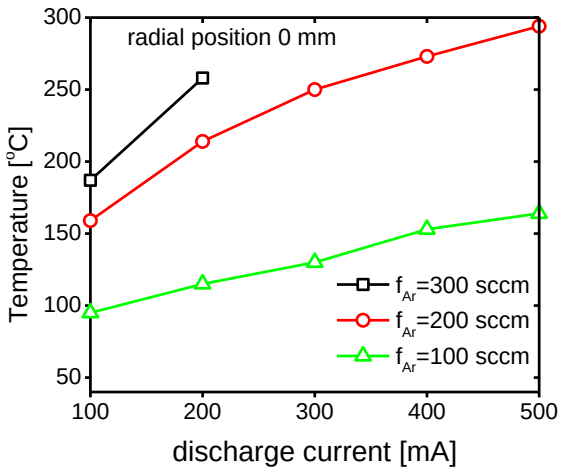

Fig. 4.5. Dependence of neutral gas temperature at the plasma axis on the discharge current with argon flow rate as parameter.

At these conditions the chemical resistance of the fibre optic thermometer is advantageous. The sensor was placed 42 mm below the nozzle exit at the position of the samples. Dependences of the neutral gas temperature at the plasma axis on the discharge current are given in **Fig. 4.5**, the radial temperature profiles for different flow rates with discharge current taken as parameter are shown in **Fig. 4.6**. Generally, the turbulent regime is characterized by the higher temperatures in comparison with the laminar one. Some points were not measured due to the thermometer upper limit of 300 ºC.

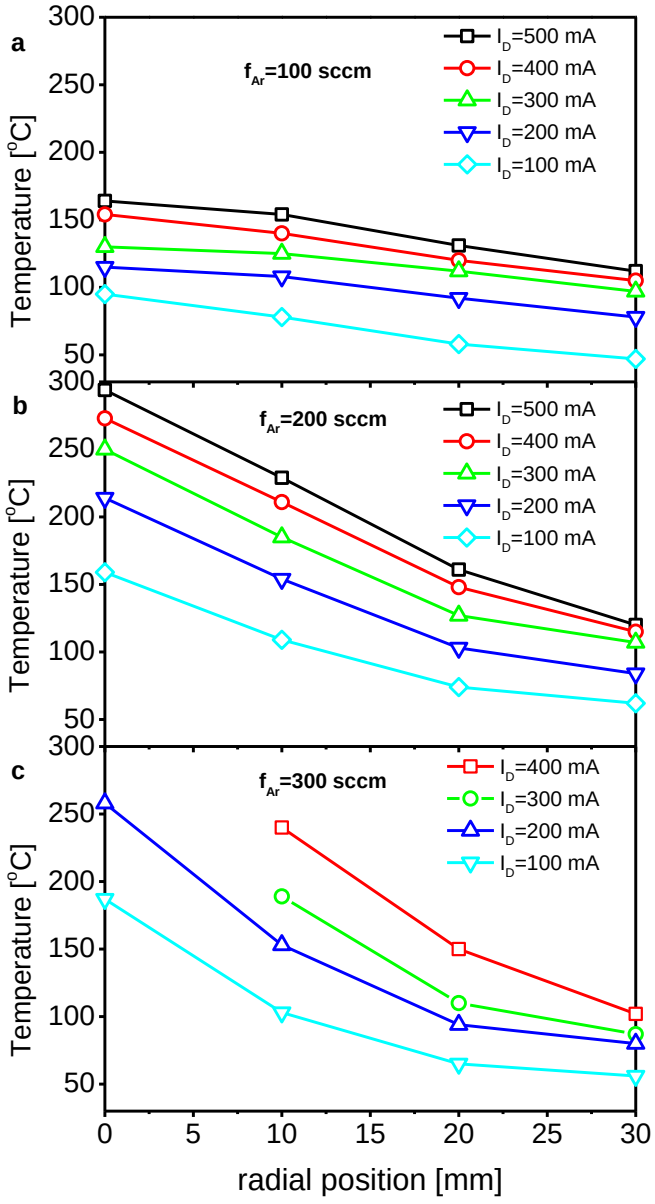

Fig. 4.6. Dependences on the radial position and discharge current for the three different values of argon flow.

However, extrapolation of the dependence that corresponds to an argon flow rate of 300 sccm shows that the temperature probably exceeds 300 ºC at discharge currents above 300 mA. The increased flow leads to higher radial temperature gradient especially in the proximity of the plasma axis. For the flow rates of 100 sccm, 200 sccm and 300 sccm this temperature gradient is 10 ºC/cm, 65 ºC/cm and 100 ºC/cm respectively. The temperature of plasma plume over 300 ºC initiates the processes of film crystallization. The thin film annealing by plasma is discussed in section 4.3.

4.3. Characterization of thin nanoparticle-rich pure titanium layers deposited in laminar flow regime

We tried to cover a wide range of experimental conditions to optimize the deposition process. We started from the laminar regime of the flow since it makes a lower stress on the pumping system and plasma plume is much colder. First results were obtained without introduction of the oxygen to exclude this parameter from the list of parameters that affect deposition process i.e. to make the characterization process easier.

The thickness of the films was measured during the deposition by the QCM. To keep the accuracy the quartz crystal was positioned in vacuum chamber as close as possible to the substrate. The crystal was connected to its oscillator by the in-vacuum coaxial cable and coaxial feedthrough. The frequency was monitored by the frequency counter HP 53181 A. Processing and saving obtained data was realized using software in Agilent VEE.

Frequency shift [Hz]	Thickness (AFM) [nm]	Thickness (QCM) [nm]	Ratio (T[AFM]/T[QTM])
200	22	7.9	2.78
300	33	12.0	2.75
450	44	18.0	2.44

Tab. 4.1. Results of QCM calibration.

To calibrate the QCM several depositions with a different frequency shifts were done. Thicknesses of obtained films were measured by means of AFM. All formulas for the thickness calculation from QCM, see chapter 2.5, provided almost the same results within 5 % error. The Ti film density d_f = 4.5 g/cm^3 was used in the calculation. The QCM results differed from AFM results approximately by the same factor of 2.6 for all three samples, see **Tab. 4.1**.

This factor cannot be explained only by the oxidation of the film after the deposition. The rough estimation shows that each nm of Ti metallic layer turns into 1.75 nm of TiO_2. In practice the deposited material has porous structure and its density is significantly lower with respect to the bulk material. Together with other uncertainties like different deposition rate on substrate and QCM, temperature changes etc. the necessity of the calibration is evident.

Unfortunately, this calibration has to be repeated for different deposition conditions i.e. the pressure, working gas flow rate, substrate position.

To check the purity during the deposition the ion plasma composition was measured by the mass spectrometer (MS). Before the deposition was carried out the system was pumped down to the basic pressure of $1.6 \cdot 10^{-4}$ Pa while during the

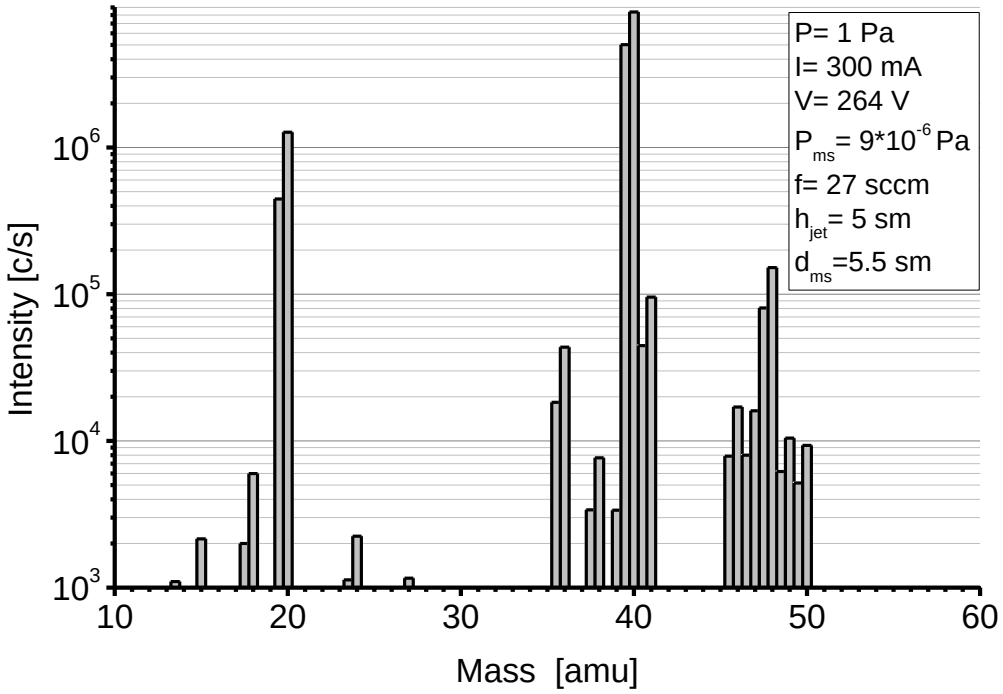

Fig. 4.7. The plasma ion composition during the deposition of thin layers.

deposition the Ar pressure of 1 Pa. The discharge current to HCPJ was stabilized at 300 mA and voltage was 264±10 V.

The mass spectrum is depicted in **Fig. 4.7**. Spectrometer was operated in the positive ion detection mode. The mass step was 0.5 amu hence the height of the peaks can be calculated as a mean value of two nearest peaks. Two highest peaks correspond to $^{40}Ar^{+}$ and $^{40}Ar^{++}$.

Next predominant peaks are titanium stable isotopes ^{46}Ti, ^{47}Ti, ^{48}Ti, ^{49}Ti and ^{50}Ti. Titanium has exceptionally high natural abundance of stable isotopes. Measured concentration of titanium isotopes approximately corresponds to the natural concentration which is given in **Tab. 4.2**.

Isotope	Mass [a.m.u.]	Natural abundance [%]
^{46}Ti	45.9526294 (14)	8.25 (3)
^{47}Ti	46.9517640 (11)	7.44 (2)
^{48}Ti	47.9479473 (11)	73.72 (3)
^{49}Ti	48.9478711 (11)	5.41 (2)
^{50}Ti	49.9447921 (12)	5.18 (2)

Tab. 4.2. Natural concentration of stable titanium isotopes [52].

The dynamics of selected ion signals in time is depicted in **Fig. 4.8**. The sputtering process lasted 40 minutes during which the mass spectrometer measured the concentration of the selected masses corresponding to atoms and molecules that can be present in the plasma. All atoms and molecules except of titanium and argon are considered as impurities.

From **Fig. 4.8** is apparent that the concentration of impurities after 40 minutes of sputtering is one order less than in the beginning. Titanium is an extremely active chemical element, consequently it absorbs all chemically active gases. It is reasonable to start the deposition process after 20 minutes of cleaning by titanium. Concentration of the mass 80 that corresponds to TiO_2 is slightly increasing during the sputtering process. It can be caused by the presence of Ar_2^{+} ions which mass coincide with TiO_2. They can be created in a region of heightened pressure inside of the hollow cathode. Lower titanium and argon ion signals at approximately 5 minutes

can be explained by the lower cathode sputtering rate due to the presence of passive oxidized TiO_2 layer on the cathode.

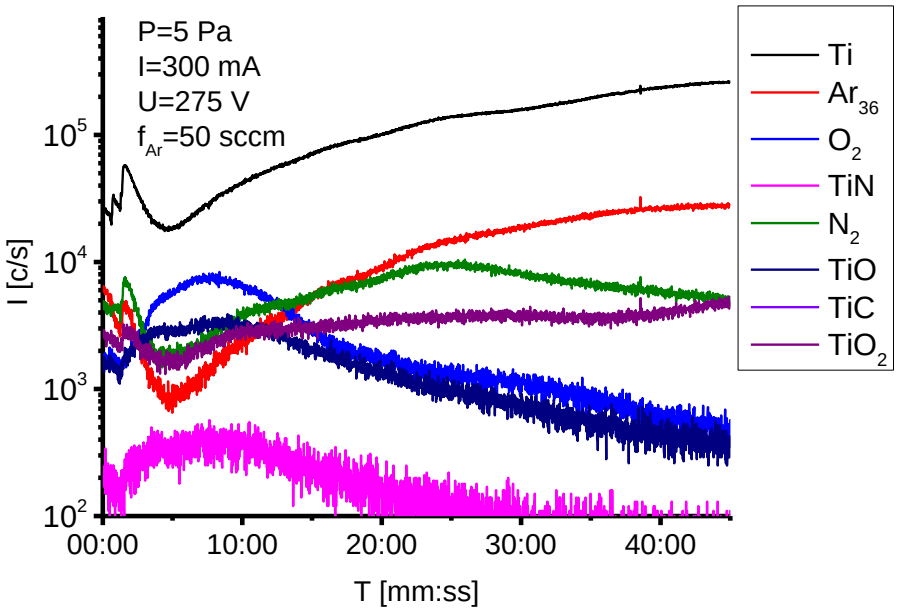

Fig. 4.8. The dynamics of selected ion signals in plasma during the deposition. List of the measured ions is shown in a right part of the figure.

MS measurements with introduction of the O_2 to the main chamber were complicated by the nonconductive TiO_2 layer covering the MS orifice diaphragm. It resulted in the accumulation of the charge near the orifice and ion signal decrease. Even changing the potential of the isolated diaphragm with the sampling orifice did not improved the ion signal. The floating potential of this diaphragm gradually increased after the introduction of O_2 and reached tens of volts.

AFM scan of deposited nanoparticle layers in a laminar regime of the plasma flow with the corresponding size distribution histogram are shown if **Fig. 4.9**. The vacuum system was pumped down to the basic pressure of $1.1 \cdot 10^{-4}$ Pa before the start of the deposition. Pressure and argon flow rate during deposition were 0.3 Pa and 30 sccm respectively. Plasma jet was powered by the dc current of 300 mA and voltage was 303–326 V. Voltage was gradually decreasing during the deposition process. We assume that it is associated with cleaning of the cathode surface and decrease of the cathode work function. The sample was deposited on the monocrystalline silicon (111) substrate placed on the substrate holder of the movable sample load-lock system. The cathode-to-substrate separation was 15 mm and the deposition of the sample in **Fig. 4.9** lasted 35 min.

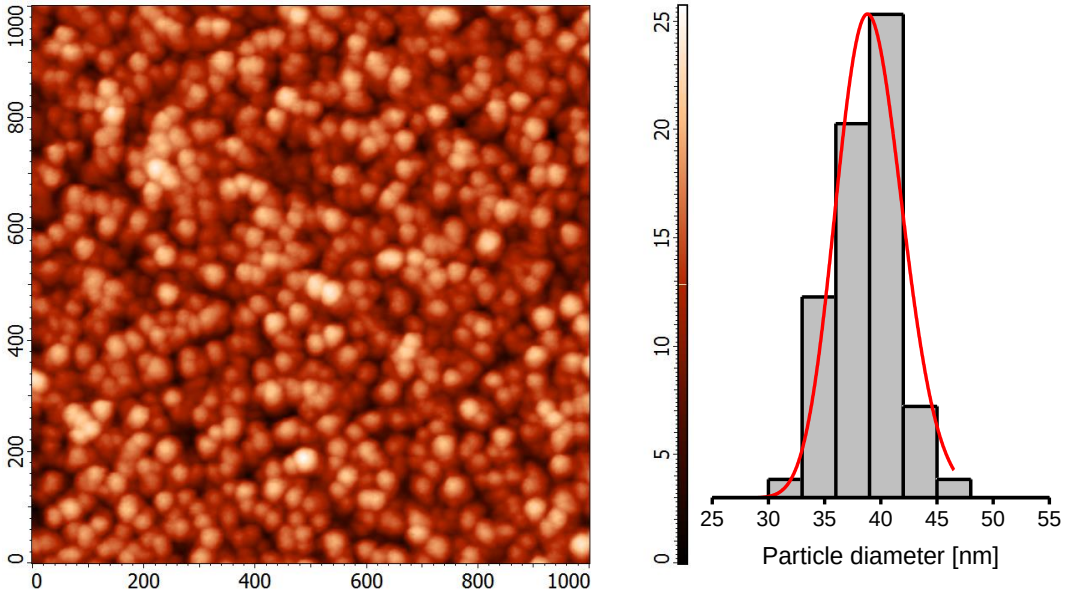

Fig. 4.9. AFM scan of pure Ti nanoparticle layers deposited in the laminar regime of the plasma flow (left) and corresponding size distribution histograms (right). Dimensions of the scan are given in nanometres.

The morphology of the thin film was analysed by AFM NT-MDT Ntegra Prima with Multi75-DLC cantilevers in semi-contact mode. The thin film consists of nanoparticle layers with rather narrow size distribution. Histogram with the size distribution is given in **Fig. 4.9(right)**. It is built from more than 100 manually measured particles. We used log-normal fit to estimate the mean particle diameter which is 39 nm.

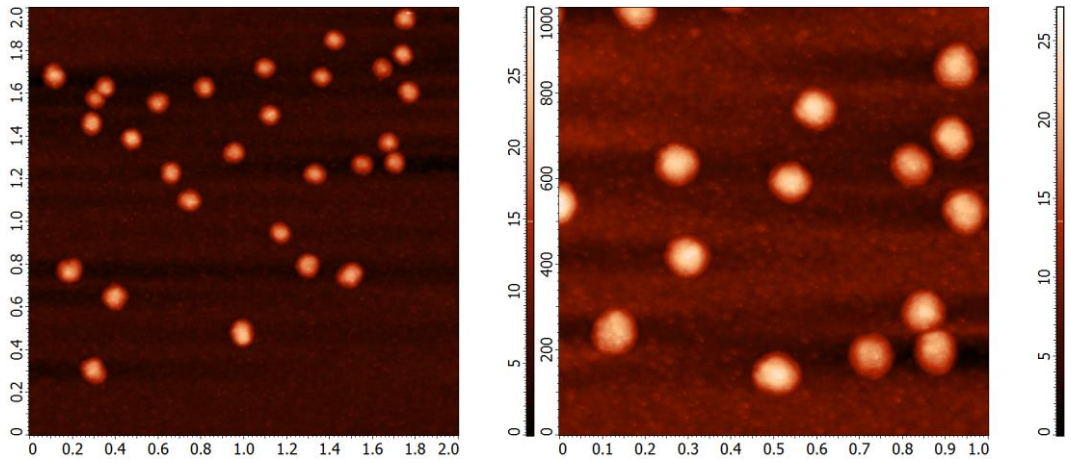

Fig. 4.10. AFM scan of pure Ti clusters measured at different zoom. Lateral scales of the left figure are given in μm while scales of right figure and both height scales are in nm.

Sometimes we observed the presence of clusters with diameter more than 100 nm. AFM scans of such clusters are shown in **Fig. 4.10**. Deposition lasted 10 minutes

at the cathode-to-substrate separation 10 mm. The rest of conditions coincide with deposition conditions of the sample shown in **Fig. 4.9**.

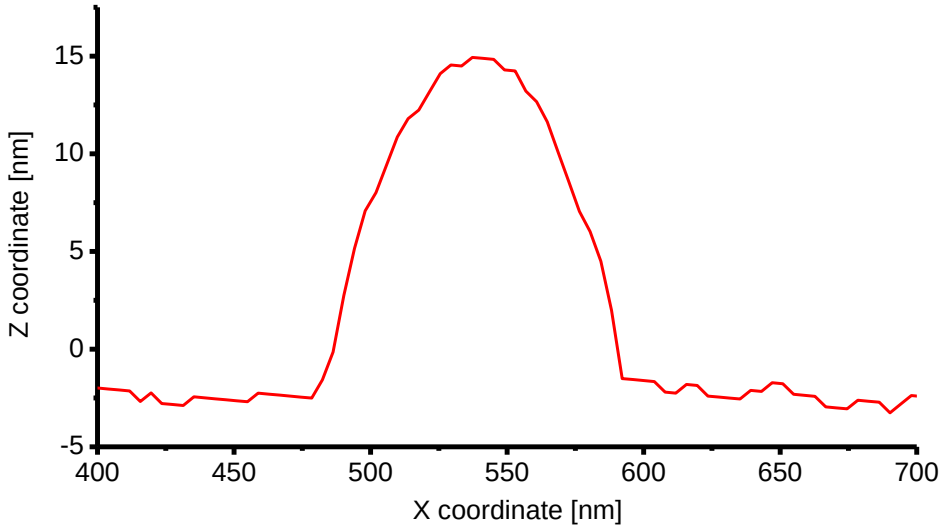

Fig. 4.11. The profile of the cluster with diameter 114 nm and height 17.5 nm.

Clusters have "squeezed" shape probably because of the interaction with substrate at the high velocity. We assume that these nanoparticles originate in plasma and obtain the velocity which is close to the neutral gas in plasma flow. Gas velocity can easily exceed supersonic value as it was shown in previous results by Bárdoš [53]. Clusters are surrounded by flat titanium film with 1–2 nm roughness. The profile of one cluster with diameter 114 nm and height 17.5 nm is shown in **Fig. 4.11**. The clusters were distributed nonuniformly at the surface of the sample, and it was hard to reproduce films with a constant morphology at these conditions. It can be partially explained by the change of the sputtering rate in time, which follows from the **Fig. 4.8**.

4.4. Surface analysis of TiO_2 nanoparticle-rich films

Nowadays science and industry is rather interested in a production of TiO_2 nanocomposites than pure Ti because of the exceptional photo activity of this material (dye-sensitized solar cells, photocatalysis, etc). The process of TiO_2 deposition by HCPJ is governed by several macroparameters. Among the most

important are discharge power, pressure, working gas flow rate, and the cathode to substrate separation. Each of these influences the physical quantities that are important for the properties of the deposited material: the degree of ionization, the gas temperature, plasma, flow dynamics, etc. We were concentrated on effects of the discharge current and argon flow rate since we believe that these parameters make the most valuable contribution in deposition process. The first idea was to use a passive $TiO_2/Ti_2O_3/TiO$ layer on the top of the cathode as the main source of oxygen which appears after each exposure of the cathode to the air atmosphere, or after introduction of argon mixed with oxygen into the HCPJ nozzle [54]. The passive layer has a thickness from several nanometres up to several tens of nanometres which depends on the surface porosity. This approach, however, has many disadvantages: restriction in thickness, a high degree of impurities, stoichiometric inhomogeneity, and difficulty in reproduction. In a case if we introduce oxygen directly to the hollow cathode mixed with the argon flow the discharge became extremely unstable because of intensive cathode surface oxidation and consequently higher cathode work function. To solve this problem we introduced the oxygen separately from argon into the main discharge chamber in the amount of 0.5 sccm which is comparably small in comparison with argon flow, see **Fig. 3.2**. Relatively high pressure (100 Pa) was used to create favourable conditions for cluster synthesis. Samples were deposited at distance 40 mm from the cathode outlet [3].

While conventional systems for the synthesis of nanoparticles use separate pumping of aggregation (higher pressure) and deposition (lower pressure) chambers [12] we made use of a pressure gradient between the hollow cathode's inner volume and the vacuum chamber. Thus, the inner volume of the hollow cathode serves as an aggregation chamber due to a heightened pressure inside it.

We made a cross section of several hollow cathodes that had been in use for approximately one year and examined its inner surface. We conclude that sputtering was not uniform and there was a region close to the nozzle outlet where erosion had reached its maximum. The position of this region was flow dependent and had a tendency to migrate along the inner surface of the hollow cathode [3]. This migration is evident from those rare cases when discharge accidentally changes its shape and voltage. The intensity of the working gas flow directly affects a plasma flow dynamics. With an increase in the argon flow rate the plasma plume becomes longer

and obtains a well-defined columnar shape. The divergence of the plasma plume depends on the pressure in the main chamber.

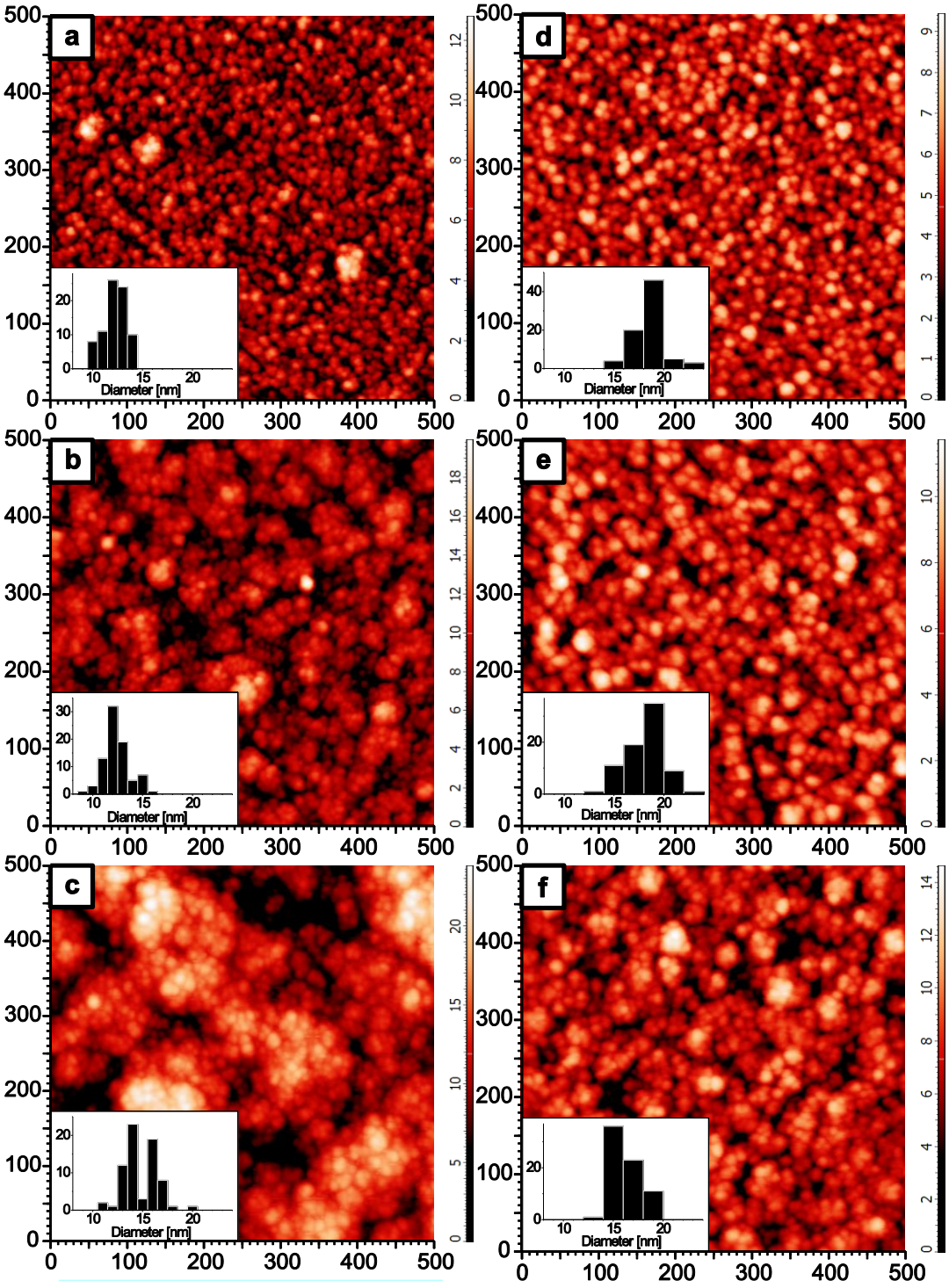

Fig. 4.12. AFM scans of TiO_2 nanoparticle layers deposited under different values of discharge currents and argon flow rates: (a)–(c) I_d = 400 mA, f_{Ar} = 100, 200, 300 sccm respectively; (d)–(f) I_d = 100 mA, f_{Ar} = 100, 200, 300 sccm respectively. Dimensions on the scales are given in nm.

AFM scans of the samples' surfaces deposited under different experimental conditions are depicted in **Fig. 4.12**. The surfaces were scanned approximately in the

sample centre. From vertical scales the conclusion can be drawn that the roughness of the film is gradually increasing with the argon flow rate. The samples deposited under a working gas flow rate of 100 sccm, see **Fig. 4.12(a,d)**, are out of the dense plasma region; therefore, we assume the plasma's influence is almost negligible and the temperature of the substrate surface stays at a relatively low value (from 50 up to 130 ºC). Measurements of the neutral gas temperature were described in more detail in section 4.2. On the other hand, samples deposited under argon flow rates higher than 200 sccm were in direct contact with the flow of plasma. Under these conditions nanoparticles have a tendency to form bigger agglomerates, see **Fig. 4.14**.

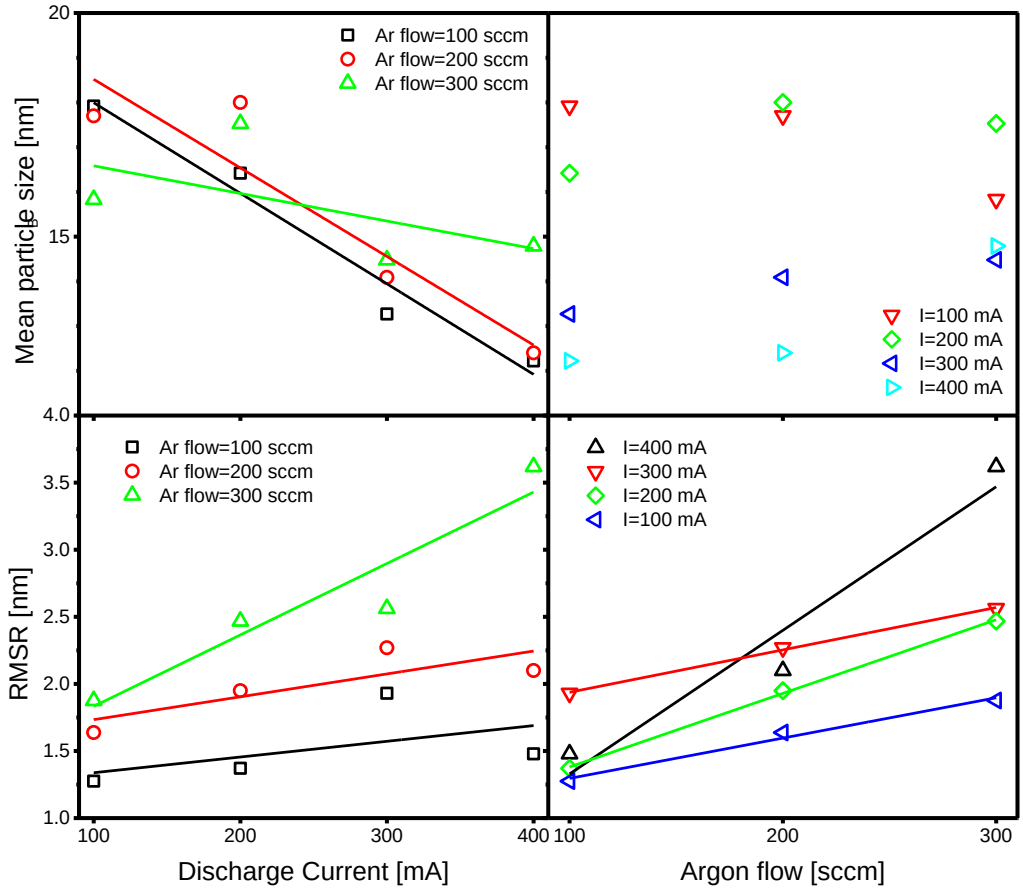

Fig. 4.13. Dependences of the mean nanoparticle size (top) and root mean square roughness (bottom) on: (left) discharge current, (right) argon flow rate.

We assume that in first approximation nanoparticles have a spherical shape. Using this assumption we have manually measured particle diameters. We used approximately 70–100 randomly chosen nanoparticles from each scan and complemented **Fig. 4.12** with corresponding histograms. Particle diameters were of the same order as the tip curvature of the AFM cantilevers, which was specified as

<10 nm. We assume that this can cause a slight shift of measured diameters to higher values.

In [39] was also observed the increase of the mean Fe nanoparticle size with the decrease of the working gas flow rate. The authors explained this effect by the increased time of flight of nanoparticles to the substrate. We did not observe the significant dependence of the mean nanoparticle size with the working gas flow rate as seen in **Fig. 4.13(top-right)**. Since the cathode to substrate separation is much shorter, we believe that the mean nanoparticle size is affected by two competing effects: (i) the shorter residence time at a higher gas flow rate which leads to the creation of smaller nanoparticles and (ii) more effective Ti atoms thermalization at higher working gas flow rates that is beneficial for creating larger nanoparticles. As follows from experiment, at a distance of 3.5 cm from the hollow cathode and the substrate used in our experiment, these two effects apparently cancel each other out.

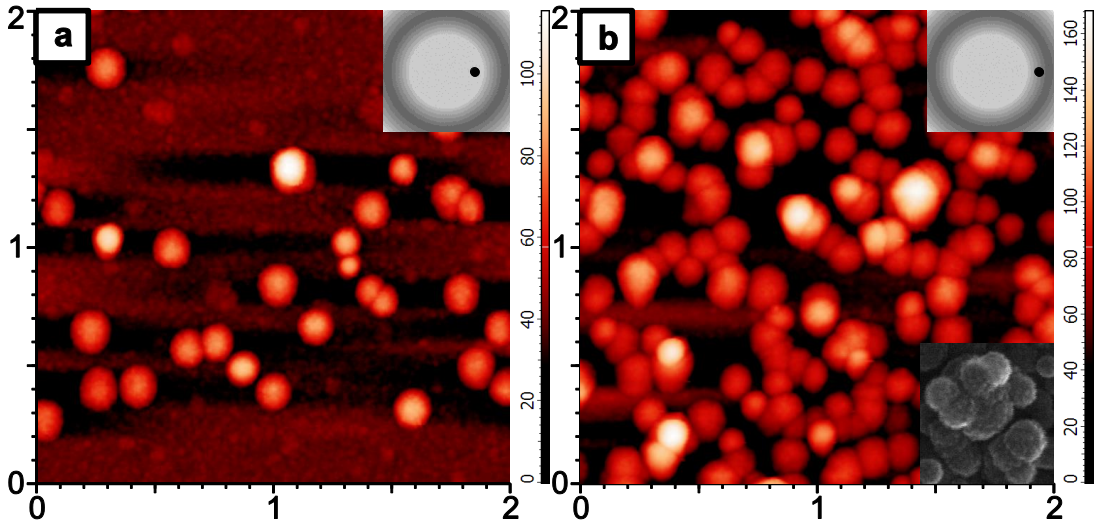

Fig. 4.14. AFM scans of the sample deposited under I_d = 520 mA and f_{Ar}=300 sccm (a) at 5 mm from the sample centre, (b) at 7 mm from the sample centre. The positions of the scans are indicated in the sketch in the top right-hand corner. The higher resolution SEM scan added in (b) shows the morphology of particles in details. Length and width are given in micrometres, colour height scale in nm.

The dependencies of mean nanoparticle size and root mean square roughness (RMSR) on discharge current and argon flow rate are given in **Fig. 4.13**. Nanoparticle sizes vary in the range of from 10 nm up to 20 nm. From **Fig. 4.13(top-left)** it is possible to observe an evident decrease in the mean nanoparticle size with the growth of the discharge current. At the same time, the

argon flow rate has almost no influence on the nanoparticle size. The RMSR of the nanoparticle layers gradually increases with the growth of both parameters.

The distribution of nanoparticles on the surface of the substrate becomes nonuniform under the high discharge current and working gas flow rate corresponding to **Fig. 4.14(a,b)**. The samples we deposited under these conditions have a specific structure. In the middle of the sample we observed a round region with high reflectance. The dimension of this region approximately corresponds to the dimension of the plasma flow (10–12 mm). This region is surrounded by a black matt ring where we observed a presence of agglomerate clusters. In a centre of the sample agglomerate clusters were not found.

Agglomerates of nanoparticles have a grained surface morphology, see SEM image in 4.14 (b). The size of grains is in a range of several nanometres. Thus, we have all reasons to believe that the process of coagulation in the gas phase occurs when nanoparticles are already in a solid state. The inhomogeneous surface distribution of agglomerated particles on the substrate is facilitated by the increase in the working gas flow rate. A high working gas flow rate causes the higher pressure and flow velocity inside of the hollow cathode. This restricts both the radial diffusion of the sputtered titanium atoms to the axis of the plasma plume, and the time of flight of the particles growing near the axis to the substrate. It results in a highly concentrated titanium vapour close the cathode wall, which leads to a higher concentration of nanoparticles in the outer layers of the plasma flow, and subsequently to a significant number of collisions between the nanoparticles in this outer layer. In addition, clusters can be mechanically moved from the sample centre to its periphery by the intensive the argon flow. This effect has been studied and visualized in [55]. Since roughly estimated Reynolds number for the flow velocity 300 m/s, argon temperature of 400 K, and stream diameter of 20 mm is about 370, turbulences and therefore turbulent agglomeration [56] may start to occur. The amount of the agglomerate particles is small at discharge currents lower than 300 mA since the sputtering rate is low. It supports our assumption that agglomerated particles can be deposited only at a high working gas flow rate in conjunction with a high discharge current.

4.5. Chemical analysis of TiO_2 nanoparticle-rich films

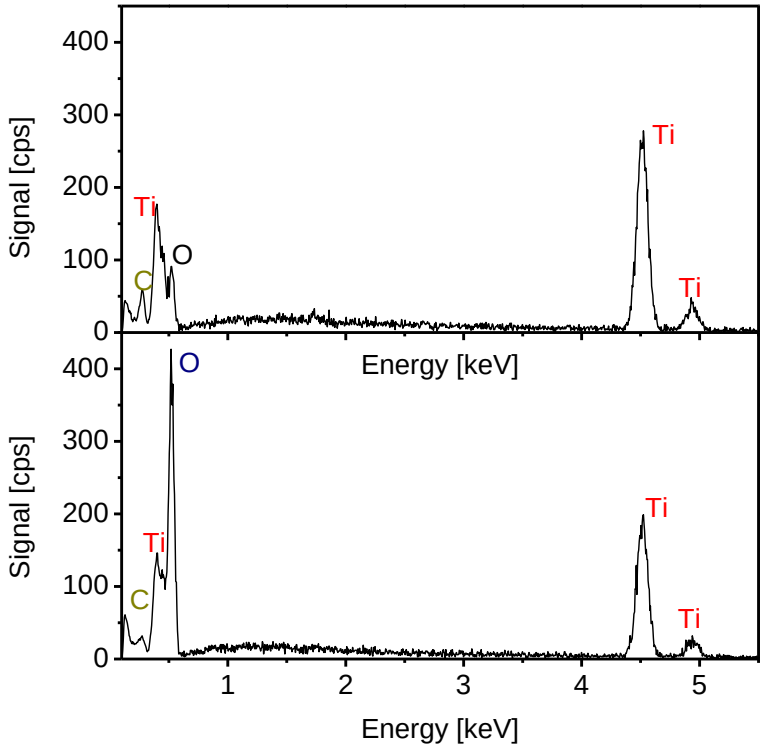

Fig. 4.15. EDX patterns of thick TiO_2 nanoparticle layers without (top) and with oxygen flow of 0.5 sccm (bottom).

The quantitative composition of the thin films measured by the EDX is shown in **Fig. 4.15**. Relatively thick samples with thickness of 3.5 μm that exceeds the electron penetration depth were prepared in order to exclude the influence of a silicon substrate on the EDX measurements.

The first sample deposited without introduction of oxygen into the main chamber was weakly oxidized (O 28 %, Ti 62 %). This was caused mainly by the exposure of the sample to the air atmosphere during transport to the EDX. The atmospheric oxygen reacts with titanium and creates an amorphous oxidized TiO_2 layer on the top which resists further oxidation. The oxidation depth is commonly 5–10 nm [54]. In our case, the oxidized layer can be much thicker due to the developed morphology of the film surface. The second sample shows the stoichiometry of O (63 %) and Ti (32 %), which corresponds to the titanium. In both samples we also found a small amount (4 %) of carbon impurities. The conclusion can be drawn that even a comparatively low oxygen flow rate (0.5 sccm) is enough for the complete oxidation of titanium.

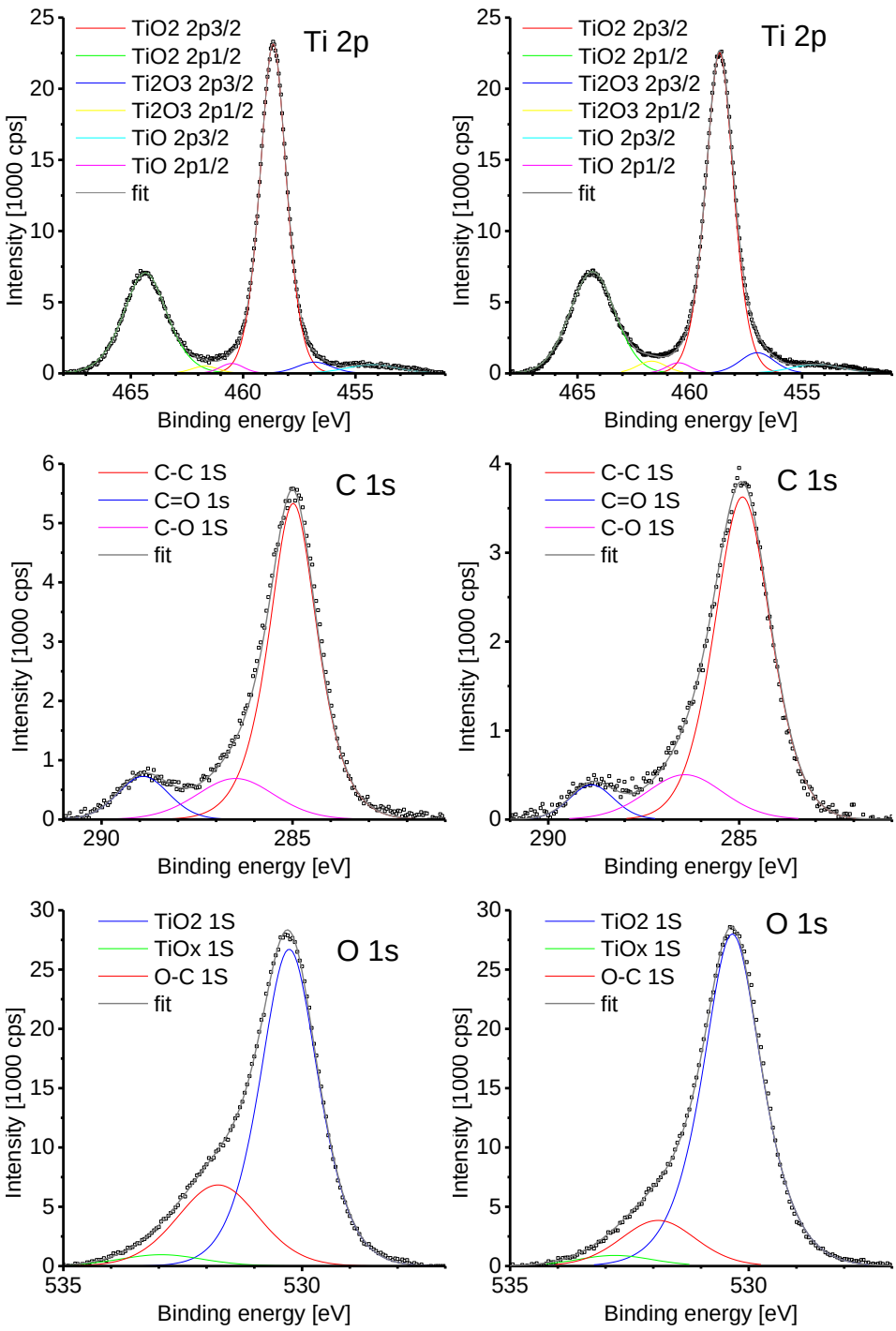

Fig. 4.16. XPS spectra of thick TiO_2 nanoparticle layers without (right) and with (left) oxygen flow of 0.5 sccm.

XPS spectra of the samples deposited with (left) and without (right) oxygen are depicted in **Fig. 4.16**. Results were processed in a program CasaXPS. The analysis of the carbon 1s photoelectron peak indicates that the carbon is not chemically bonded with the titanium. Since the experimental system was HV clean, the carbon is most probably caused by exposure of the sample to the atmosphere after deposition.

Titanium 2p spectrum consists of two major peaks because of spin–orbit splitting. These two peaks correspond to TiO_2. The peaks of other titanium oxides such as TiO or Ti_2O_3 are present but are small with respect to TiO_2. The XPS spectrum of the film deposited with introduction of oxygen shows similar results.

4.6. Crystalline structure of TiO_2 nanoparticle-rich TiO_2 films

TEM characterization of sample that corresponds to the **Fig. 4.12(c)** was performed on Philips CM120ST microscope, working at 100kV high voltage. Electron diffraction technique (SAED) was used to verify the crystallinity of sample and crystal size from Debye-Scherrer formula, see **Fig. 4.18**.

TEM image of the single agglomerated particle is depicted in **Fig. 4.17(right)**. Nanostructure of agglomerated particles consists of spherical nanoparticles embedded in the amorphous matrix. Electron diffraction has shown the amorphous crystalline structure with traces of anatase.

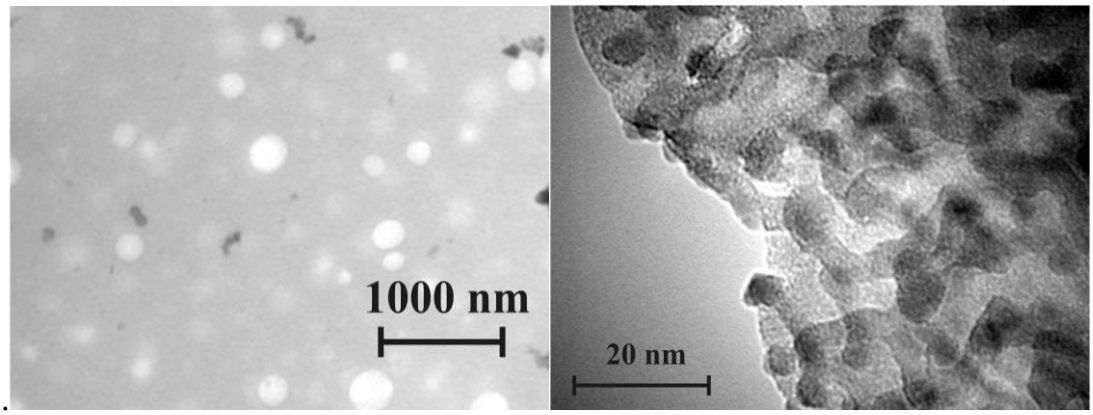

Fig. 4.17. TEM scans of the agglomerated particle region (left) of the sample that corresponds to the **Fig. 4.12(c)** and high resolution structure of agglomerated particle (right).

Electron diffraction measurements exhibit complex mix of phases, part of this can be associated with cubic structure of Si and also with tetragonal structure of anatase. Sample has a polycrystalline structure represented by traces of anatase mixed with amorphous TiO_2 phase and silicon (111) substrate. The estimated size of domains is about 4 nm.

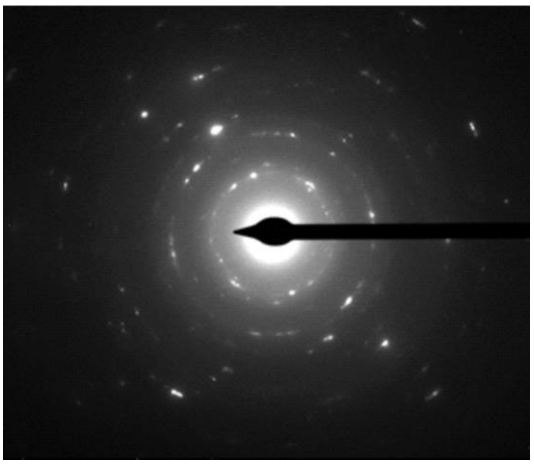

Fig. 4.18. Electron diffraction for zone in **Fig. 4.17(right)**.

In order to carry out more detailed diagnostics of the crystalline structure of deposited TiO_2 films we deposited several samples with thicknesses of several micrometres on the glass substrates for XRD analysis. Deposition pressure, oxygen flow rate and distance from the cathode to substrate coincided with the samples in **Fig. 4.12–4.14**.

Sample	$Flow_{Ar}$ [sccm]	I_d [mA]	T_a [ºC]	t [min]
S1	100	200	-	180
S2	100	200	400	180
S3	300	200	-	120
S4	300	200	400	120
S5	300	400	-	45
S6	300	400	400	45

Tab. 4.3. Deposition conditions of the samples Symbol meaning: $Flow_{Ar}$ – argon flow rate, I_d – discharge current, T_a – annealing temperature, t – deposition time.

Deposition conditions are given in **Tab. 4.3**. Some of samples were annealed in a muffle furnace in the atmosphere at the temperature of 400 °C. The crystalline structure of the samples S1–S6 was analysed by means of Seifert XRD7 diffractometer with parallel-beam geometry, Cu K_α radiation and fixed angle of incidence of x-rays $\omega = 5°$. The non-annealed samples S1 and S3 exhibited amorphous structure as it is shown in **Fig. 4.19(a)**. Annealing of the samples at the temperature of 400 ºC activated the processes of crystallization (samples S2, S4) in a

form of pure anatase phase. Such results are in agreement with previous reports on crystallization of TiO_2 [57]. The crystalline phase of anatase was confirmed by (101), (004), (200), (105) and (204) diffraction peaks. The interesting result is the asymmetrical crystallization of samples S2 and S4. The highest peak of sample S4 is at $2\theta = 37.8^{\circ}$ which corresponds to the plane (004), while the highest peak of the sample S2 is at $2\theta = 25.3^{\circ}$ which corresponds to the plane (101).

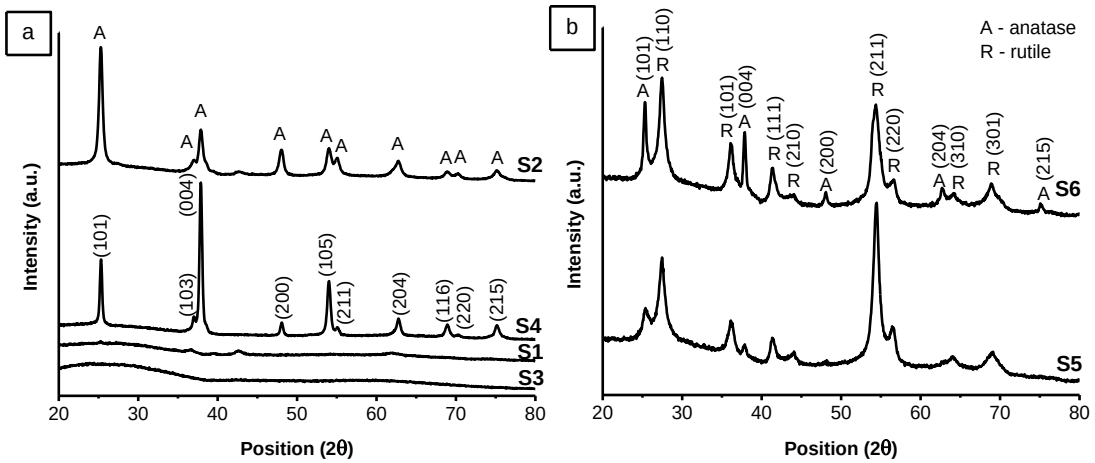

Fig. 4.19. XRD patterns of the samples S1–S4 (a) and S5–S6 (b). The Miller indices of anatase and rutile phases are given.

The samples S5 and S6 exhibit qualitatively different XRD spectrum, see **Fig. 4.19(b)**. The presence of rutile and anatase crystalline forms was detected in both samples regardless of annealing. The crystalline rutile phase is the dominant and was confirmed by (110), (101), (111), (211) and (220) diffraction peaks. The highest peak is at the $2\theta = 54.3^{\circ}$ and corresponds to the plane (211). Anatase is the less abundant phase in the samples S5 and S6. It is represented by (101), (004), (200), (204) and (215) diffraction peaks, where (101) is the highest one. We assume that such mixture of phases can be explained by plasma-enhanced annealing of the samples. From the reported TiO_2 phase diagrams, e.g. in [58], we can conclude that samples were affected by the heightened temperature of incoming plasma flow, since rutile phase shows itself under the temperatures over 600 ºC. However, this transition temperature, in our case, can be different since the processes in HCPJ system, which under these conditions is operated in the supersonic flow regime [53], are much more complicated then annealing in the muffle furnace. Rutile is the equilibrium crystalline form of TiO_2, hence the annealing at a temperature of 400 ºC can only

result in a crystallization of the amorphous part of the samples into anatase phase which was observed on diffraction spectrum of sample S6.

5. Detection of nanoparticles in a HCPJ

HCPJ is not originally constructed as nanoparticle source thus we have to find the optimal conditions for nanoparticle deposition. Several scientific works related to the deposition of nanoparticles by means of gas flow sputtering systems e.g. [3,39] claim that nanoparticles occurs in a gas phase but there are no proofs of this theory by now. This motivated us to investigate the plasma plume – the place from where nanoparticles may originate.

The method is based on the detection of the light scattered on nanoparticles. As incident light sources served diode lasers and detectors were the photodiode, the optical spectrometer and the digital photo camera. Rayleigh and Mie theory were used as a basis for description of the results. Instant data acquisition, extremely low cost [17] and measurement in-situ makes this method favourable to the other nanoparticle detection methods such as microscopy that was also used in this work. This investigation was focused on the detection and spatial distribution of nanoparticles in plasma of HCPJ.

Three lasers with wavelength 446, 632 and 661 nm were used as sources of polarized, narrow bandwidth light. 2D maps of the scattered light intensity were assembled from the photo camera pictures at different discharge parameters. Dependencies of the signal intensity on the O_2 flow rate and wavelength are discussed. Direct measurements of particle size on the substrate were carried out by means of scanning electron microscope (SEM) in order to prove the agreement with theory. Aside from nanoparticles we detected TiO_2 columnar structures in deposited samples. Crystalline structure of the samples was investigated using X-ray diffraction analysis (XRD).

5.1. Analysis of the discharge optical spectrum

The first idea was to detect continuous thermal spectrum of nanoparticles in plasma. We assumed that relatively hot nanoparticles will irradiate electro-magnetic waves in infra-red range of wavelengths. According to Wien's displacement law the maximum of the continuous spectrum should be at the range of 3 – 5 μm under

assumption that temperature of nanoparticles close to the nozzle could be around 1000 ºK.

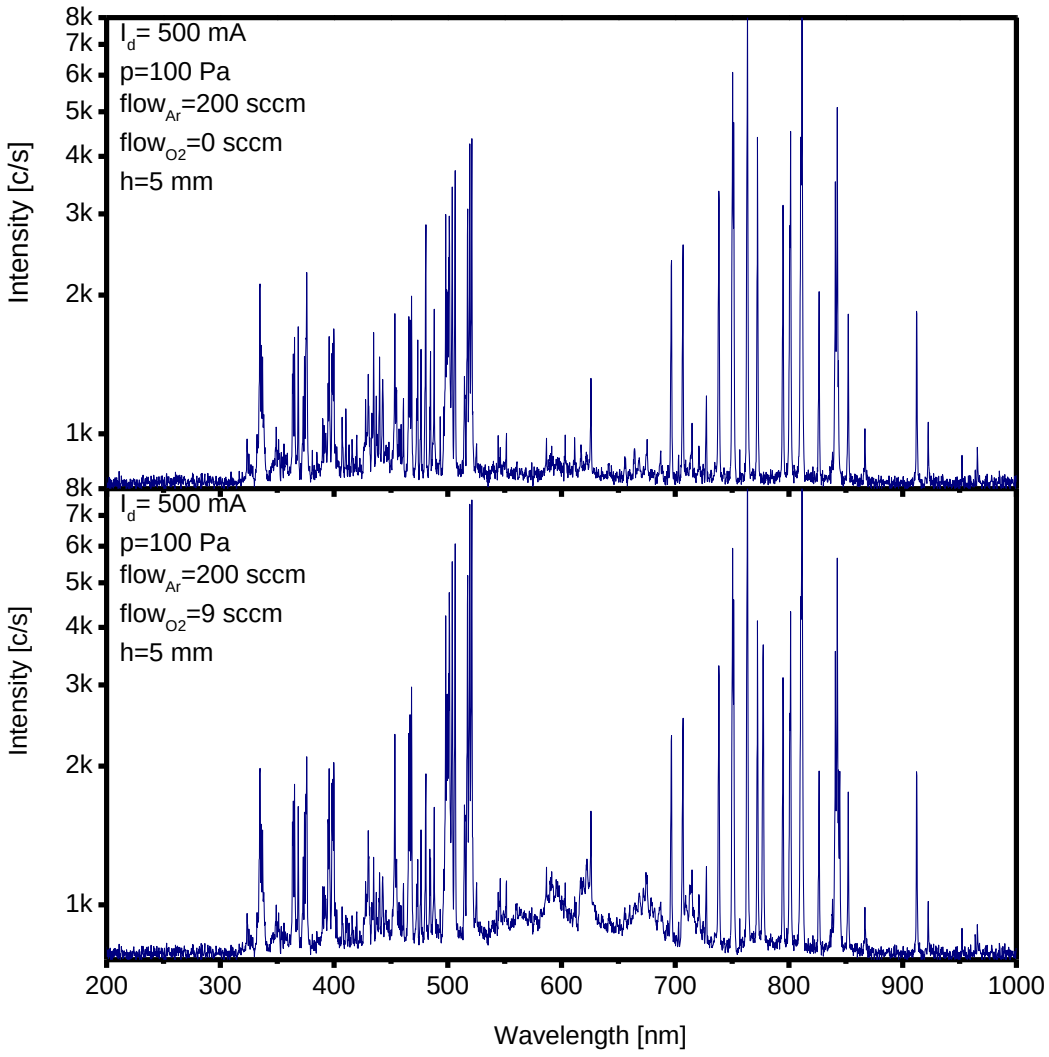

Fig. 5.1. The optical spectra of the HCPJ plasma without (top) and with (bottom) introduction of oxygen inside of the main chamber. Plasma parameters and distance from the cathode nozzle to the measured point are given in the description to each figure.

According to another theory nanoparticles effectively irradiate light in optical spectral range. This property is originated from the resonant radiation of free atoms. For many elements this radiation corresponds to spectral lines located in the optical spectrum range. The joining of atoms into molecules and nanoparticles lead to splitting and broadening of these spectral lines, and they are transformed in spectral bonds for bulk material [59].

To check this theory we used low resolution optical spectrometer connected via the optic fibre to optical lens. The position of lens was adjusted to capture the signal

from the middle of the plasma plume. Since spectrometer is limited by the range of wavelengths from 200 nm up to 1100 nm we were expecting to see at least the "tail" of the spectrum. The results of the measurements are depicted in **Fig. 5.1**. Experiments were carried out with and without oxygen since we assume that presence of oxygen facilitate nanoparticle nucleation. The conditions of the discharge are given in a legend, see **Fig. 5.1**.

Spectra represent superposition of two components – line spectrum of Ar, Ti and O atoms and developed molecular spectrum of TiO_2, O_2 and other molecules and, probably, nanoparticles. Molecular/nanoparticle spectrum is characterized by much higher density of spectral lines in comparison with atoms. Sometimes these lines are hardly distinguishing and line density depends on the amount of atoms in molecule. After a brief analysis of spectra the conclusion can be drawn that the "tail" of thermal radiation of nanoparticles cannot be detected probably because of the low sensitivity in IR range. The broad molecular/nanoparticle component of the optical discharge spectrum is more intensive in a case when oxygen was introduced into the main chamber. We assume that it can particularly correspond to nanoparticles.

5.2 Detection of the scattered at nanoparticles laser light

Another idea was to detect laser beam scattering at nanoparticles in plasma. We used red laser diode (632 nm) and photodiode for these purposes. Although the scattered light was visible by eye, the problem was to separate it from the rest of the electromagnetic radiation detectable by the photodiode. We modulated the laser current at the frequency of 1 kHz in order to exclude this radiation, see **Fig. 3.7**. The signal was filtered and amplified by means of the electric scheme shown in **Fig. 3.12**. Low pass and high pas filters changed the shape of originally rectangular pulses. The detected signal had a sinusoidal shape, since only the main harmonic (1 kHz) can be amplified. The value of the scattered signal was measured peak-to-peak by means of oscilloscope.

Dependencies of the scattered signal intensity on pressure in the main chamber and discharge current were measured and are shown in **Fig. 5.2**. In a case of the pressure dependence the value of the discharge current was 500 mA; dependence on the discharge current was measured at the pressure of 100 Pa. Error bars characterize

the scattered signal fluctuations which are comparably small with respect to the absolute value of the signal.

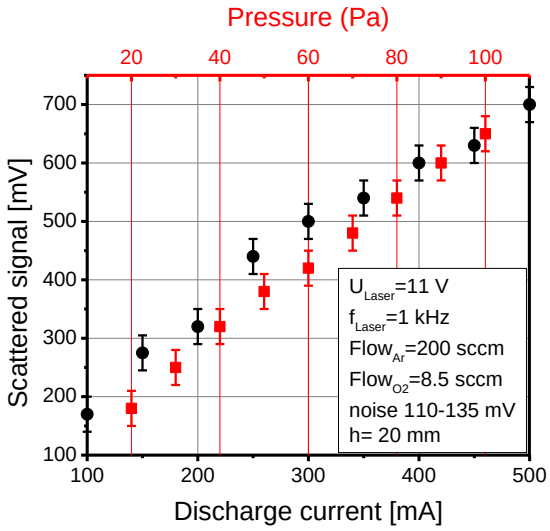

Fig. 5.2. The first results of the nanoparticles detection by means of the laser beam scattering. Dependencies of the scattered signal on the discharge current (black) and the pressure in the main chamber (red). Mutual laser and discharge parameters are given in the description at the figure.

We tried to minimize the value of the stray light signal which is caused by the scattering of the laser beam on the surface of the window and reflections from the chamber walls. The opaque tube around the laser beam insulated it from the detector field of vision. Orifice that was made of rough black paper was attached to the window in order to cut the halo of the laser beam caused by the propagation of it through the optical lens and scattering on the window. The relatively low value of constant background noise was subtracted from the signal value to obtain the part which corresponds to the light scattered on nanoparticles.

Results have shown almost linear increase of the signal with both discharge current and pressure. Discharge current affects the sputtering rate, subsequently higher concentration of sputtered titanium atoms facilitates nucleation of nanoparticles overall. Increased pressure positively affects thermalization of hot nanoparticles and decreases their velocity. These results are in agreement with our previous results described in section 4.

Measurements that were focused on the change of the scattered signal in time are depicted in **Fig. 5.3**. The HCPJ was operated at the discharge current 500 mA, the Ar flow rate 200 sccm and the pressure 100 Pa. We used an oxygen flow rate as a parameter to check if it has an influence on the signal.

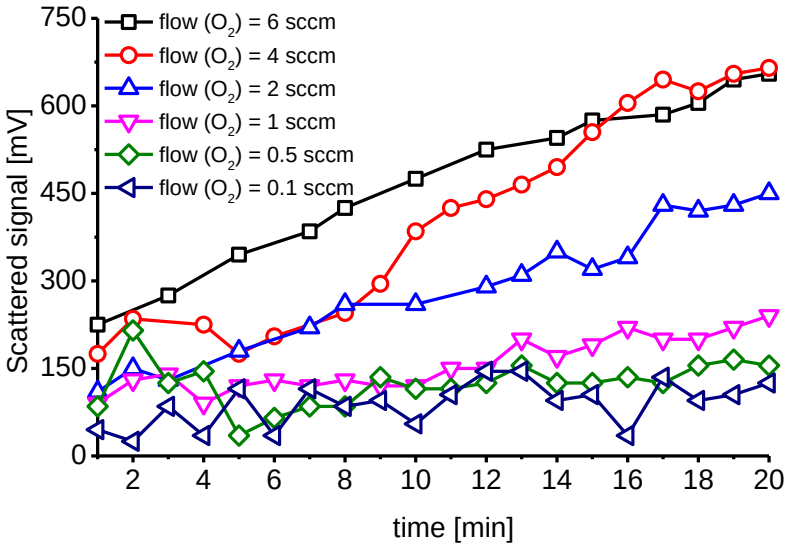

Fig. 5.3. The change of scattered signal during 20 minutes of continuous sputtering under different values of oxygen flow rate.

Results show the signal growth in time independently from the oxygen flow. The reasons can be similar as were given in explanation of the change of ion signal detected by the mass spectrometer in time, see **Fig. 4.8**. The oxidized surface of the cathode should be cleaned by the ion sputtering. The work function of the cathode decreases and we have higher emission of electrons and subsequently positive ions that serve as a driving force in sputtering process. The increase of the signal with oxygen flow is caused by higher concentration of material that is involved in nucleation since titanium reacts with oxygen and creates bigger clusters. However, these dependencies were measured for the red 632 nm laser. Probably, the behaviour of the signal can be different for another wavelength. The detailed investigation of the oxygen influence will be discussed further.

Optical spectrum of the scattered blue laser beam (446 nm) is depicted in **Fig. 5.4**. Detector was placed at the angle of 160º with respect to propagating laser beam to detect the back scattered light. HCPJ was operated at discharge current 175 mA, argon flow rate of 200 sccm and 3.5 sccm oxygen flow rate. Measurements were taken 20 mm below the nozzle at the plasma plume axis. From both curves with laser beam on the spectra with laser beam off were already subtracted as the background. The noise around the laser peak on the spectrum with both laser and discharge on is caused by fluctuations in the discharge. The small peak on the curve with discharge off corresponds to the stray light that originates from reflections on the parts of the main chamber (window faces, chamber walls etc.) and can be easily

subtracted since it has a constant value. From the measured data we conclude that the detected scattered light has the same wavelength as incident laser light and is connected with presence of the discharge with nanoparticles. Small shift of the maximum is explained by the device measurement accuracy. The scattered signal is mostly given by Rayleigh-Mie scattering. Thomson, Raman and other scattering mechanisms cannot be measured due to the low resolution and sensitivity of measuring device.

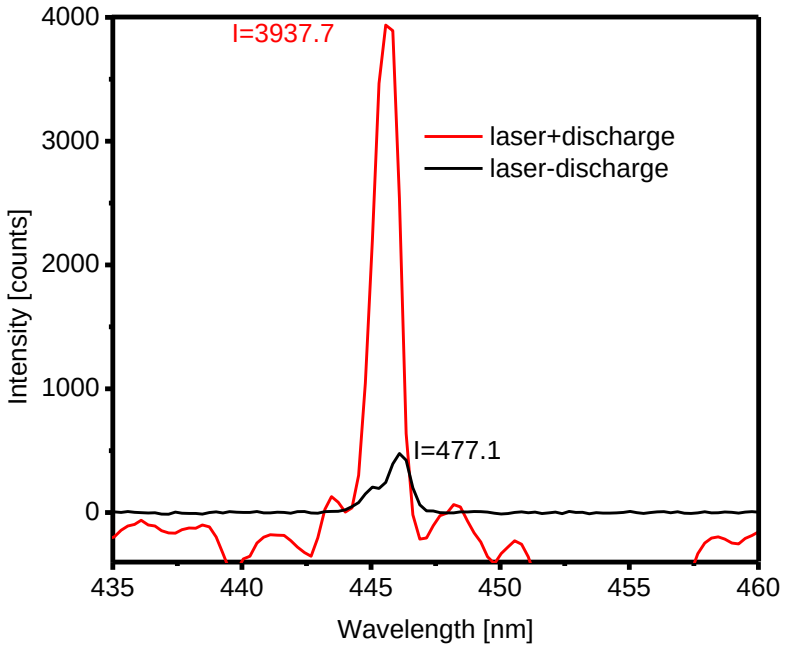

Fig. 5.4. Optical spectra of the scattered laser beam with discharge switched on and off.

Simulated polar diagrams of scattered light intensity for nanoparticle sizes 30, 100 and 450 nm and for both parallel and horizontal polarizations are shown in **Fig. 5.5**. Diagrams were simulated in MiePlot [27] software using Mie scattering theory. The intensity is normalized to the maximum that is different for each diagram. The position of laser and direction of polarization vector is shown in the diagram that corresponds to nanoparticle size 30 nm. We chose three angles – 20º, 160º and 90º for qualitative characterization of the scattered signal. The refractive index value of 3.0+0i was used in this simulations, which approximately corresponds to the titanium dioxide [60].

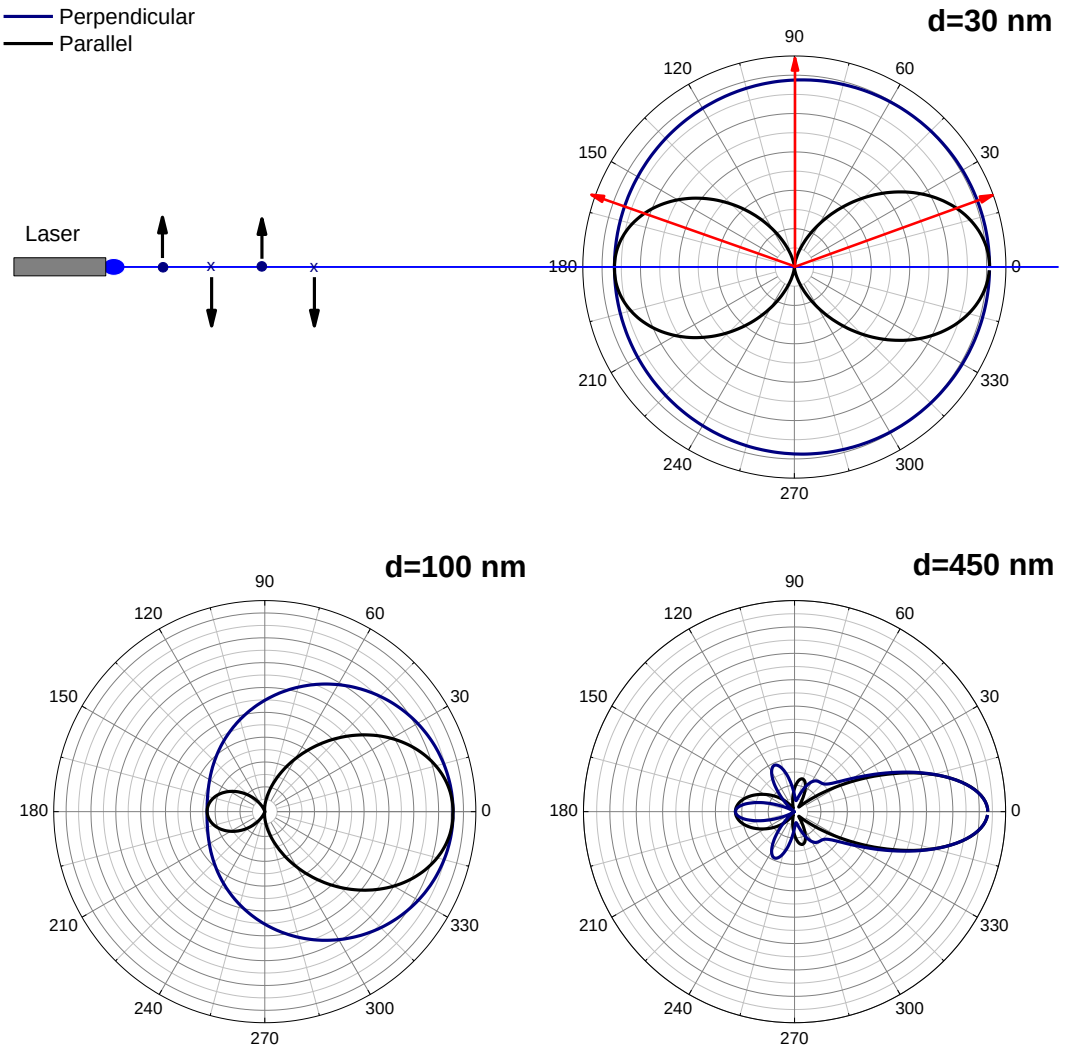

Fig. 5.5. Polar diagrams of scattered light (both perpendicular and parallel polarisations) intensities with graphical explanation of the experiment. Simulation conditions: particle diameters - 30 nm, 100 nm, 450 nm; wavelength - 446 nm (corresponds to the blue laser we used); refractive index - 3.0 (taken from the database). Scattered angles which we used in experiments are described as red arrows. The centre of polar diagrams is a particle geometrical centre.

The usage of the blue laser in experiments is preferable since the scattering mechanism is much more sensitive on the short wavelengths even at the lower sensitivity of the photodiode in a blue range of wavelengths. Results of the measurements of the dependencies of the scattered signal intensity on the oxygen flow rate by means of photodiode are shown in **Fig. 5.6**. The depicted measured signal is proportional to the scattered light intensity which can be expressed as the sum over all diameters of particles:

$$I(\theta) = \sum_{d_{\min}}^{d_{\max}} n(d) \cdot I(d, \theta), \tag{5.1}$$

where $n(d)$ and $I(d,\theta)$ are concentration and scattering intensity of particles with diameter d to angle θ.

Our efforts were focused on determination of the optimum conditions for deposition – when oxygen concentration is not enough for complete titanium oxidation and not excessively high. Distance from the nozzle outlet to the measuring place, i.e. distance to the detector was the same as for experiment with optical spectrometer. Pressure and argon flow rate were 60 Pa and 200 sccm, respectively.

Dependencies are characterized by the presence of the clearly distinguished maximum. Position of the maximum was almost the same for three different values of the discharge current and varied in a range of 0.7–1.3 sccm. The position of the maximum was constant for all experiments. The shape of dependencies is affected by two competing processes: nanoparticle growth and decreasing of the sputtering rate. Second process is caused by the electronegativity of oxygen [61]. It is described by the dissociative attachment of the O_2 molecules by electrons $O_2 + e \rightarrow O^- + O$ and the recombination of negative oxygen with positive argon ions [62]. The decrease of the electron density dumps ionization which directly affects the sputtering rate.

One more process that has a negative impact on sputtering rate is oxidation of the hollow cathode surface – so called "cathode poisoning" [63] that leads to the increased temperature of the emitting surface and higher cathode work function.

Even in the pure argon we detected a low but clearly distinguishable signal which indicated that nucleation of nanoparticles occurs even without oxygen. The process of nanoparticle formation was probably enhanced by the small amount of oxygen that can be still present in a main chamber, because the oxygen greatly intensifies the creation of particle seeds.

In a case of pure titanium or weakly oxidized particles the theory becomes more complicated since metallic particles become nontransparent when their size exceeds the skin depth described by formula $\delta = 1/\sqrt{\pi\mu\sigma f}$. For the titanium with resistivity $\sigma = 4 \cdot 10^{-7}$ Ωm·cm the skin depth calculated for blue laser wavelength is 12 nm and for red laser wavelength 15 nm.

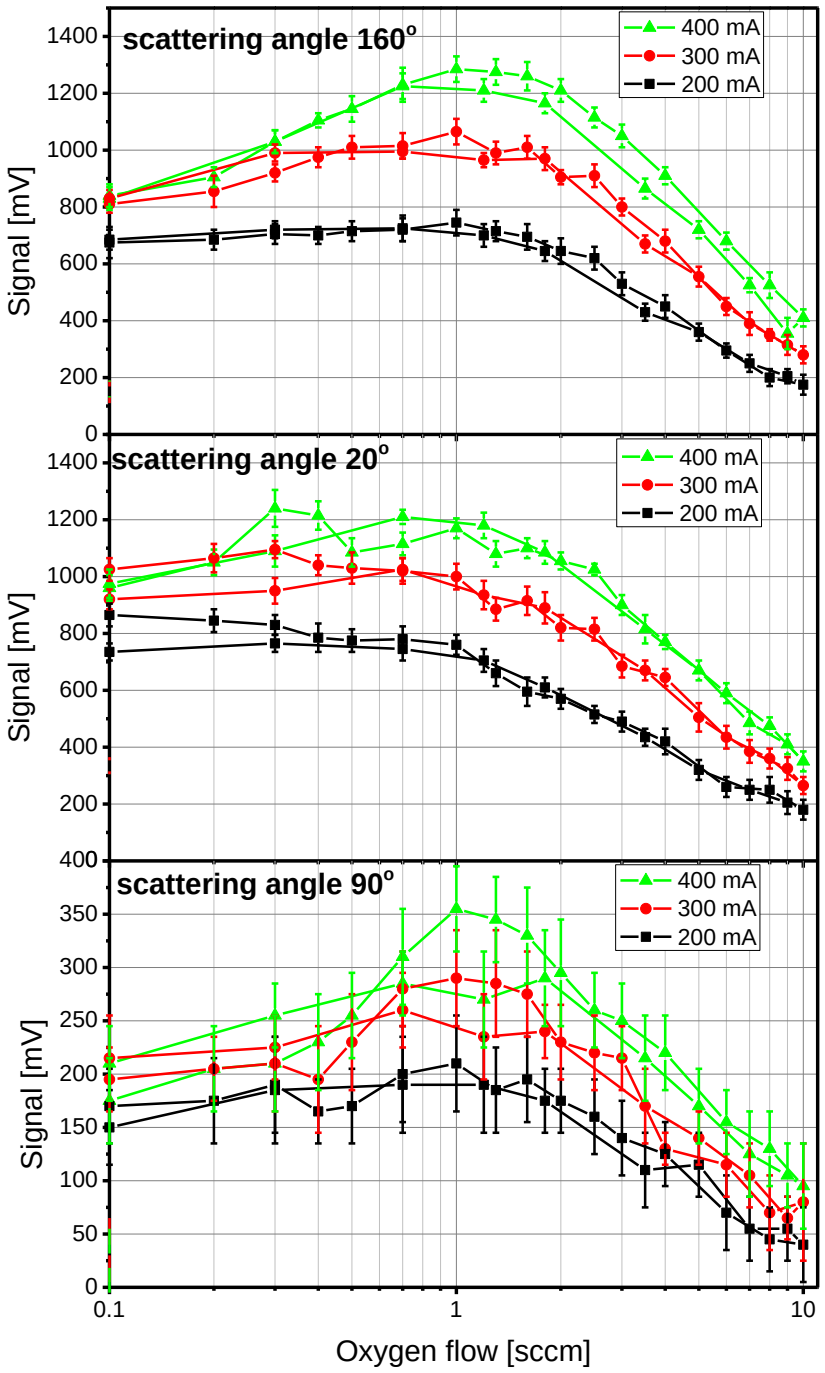

Fig. 5.6.The dependencies of scattered signal on oxygen flow rate for different discharge currents at the different scattering angles and vertical laser polarization. Laser parameters: 1 kHz modulation with 50 % duty cycle, average power 140 mW, wavelength 446 nm.

The hollow cathode was weighted before and after several days of exploitation in order to estimate the approximate titanium sputtering rate and compare it with the oxygen flow rate. The titanium sputtering rate calculated from the cathode weight

losses is 5×10^{13} atoms·s^{-1} while oxygen flow rate is 1.57×10^{15} atoms·s^{-1} (recalculated from 3.5 sccm) hence it exceeds the titanium concentration approximately 30 times.

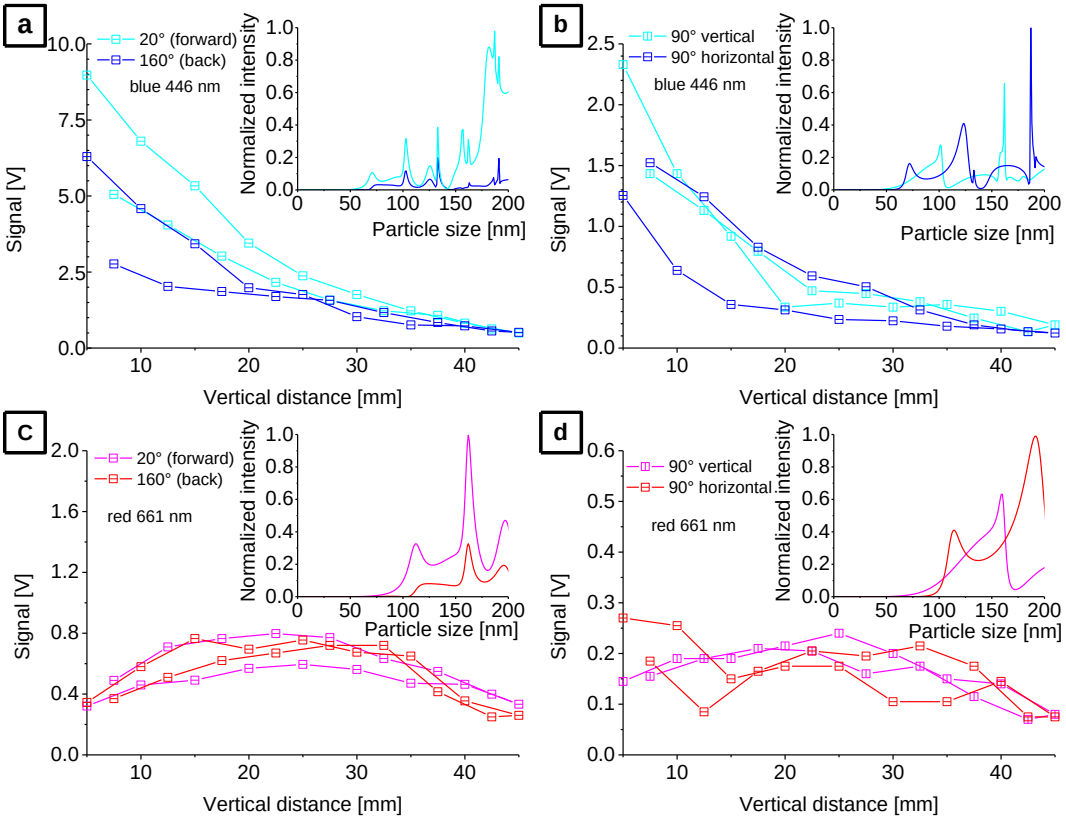

Fig. 5.7. Dependencies of the scattered signal measured by means of photodiode on the vertical position: scattering of horizontally polarized light to 20º and 160º for a) 446 and c) 661 nm; scattering of horizontally and vertically polarized light to 90º for b) 446 and d) 661 nm. Each dependency is supported by inset graph with an independent simulation of scattered intensity on particle size. Laser modulation parameters: duty cycle 70 %, mean power 110 mW. Signal from the blue laser was normalized to the red laser signal using photodiode sensitivity ratio.

From the formula 2.30 it follows that the light-scattering process is extremely sensitive to the change of both the nanoparticle size and the incident light wavelength (exponents 6 and 4 respectively). However, quantitative measurement of the particle diameter using formula 2.30 is complicated because of the relatively broad particle size distribution and unknown nanoparticle concentration, which is hard to evaluate with satisfactory tolerance. Moreover, for the horizontally polarized light the dependence of Rayleigh scattered light intensity on the scattering angle can be described as $I\sim I_0\cos^2\theta$. This motivated us to carry out the experiments with different scattering angles and incident laser light wavelengths. Although the construction of the vacuum system does not allow us to measure the full polar diagram of the scattered light intensity, we chose the most interesting angles – 90º for the

investigation of polarization influence and 20º and 160º for forward and backward light scattering comparison.

The dependencies of the measured scattered signal on the vertical position of the cathode outlet under different discharge glow conditions are depicted in **Fig. 5.7**. Each graph is supported by the simulated theoretical dependencies of scattered intensity of a single particle on particle diameter for the appropriate scattering angle and light polarization using MiePlot [27] software. Since we did not measure refractive index of the nanoparticles, we took 2.8+0*i* for 661 nm and 3.0+0*i* for 446 nm from [60] and assumed that nanoparticles have spherical shape, hence, the simulations may have only qualitative nature. The measurements along the vertical coordinate were carried out in both up and down directions to check the stability of the scattered signal. From **Fig. 5.7(a)** we concluded that intensity of scattered light signal is much higher at the beginning of sputtering process. It usually takes a few minutes for the discharge stabilization. The voltage that is necessary to maintain the constant value of the discharge current is several tens of volts higher at the beginning, the discharge voltage varies in a range 300±20 V. It is caused by presence of passive oxidized TiO_2 layer on the surface of the cathode. The common thickness of the layer is 5–10 nm [54] and depends on the surface porosity. Parts of the passive TiO_2 layer can be chipped off because of the cathode heating and affect the scattered signal. The presence of the oxygen atoms on the surface of the cathode also supports the nucleation at the initial stage of growth.

Close to the cathode outlet the backward scattered signal is significantly lower than that forward scattered. This indicates that nanoparticles size range at least partially exceeds the limits of Rayleigh approximation (upper limit is of ~0.07 λ). Both dependencies of scattering signal to the angle of 90º (**Fig. 5.7(b,d)**) show a comparable scattered light signal regardless of laser polarization. However, the behaviour of horizontal polarization is more unstable for the both red and blue lasers. We believe that it caused by the shape of the dependencies of scattered intensity on particles size since it is more flat for vertical polarization i.e. fluctuations in nanoparticle size affect horizontal polarization much stronger. If we compare **Fig. 5.7(a)** and **Fig. 5.7(c)** two main conclusions can be drawn: for blue laser the influence of higher concentration of nanoparticles in plasma near the nozzle outlet is more significant than the lesser particle size; for red laser the situation is completely opposite since the maximum occurs approximately in the vertical distance 25 mm.

The ratio between red and blue signal is not constant with respect to the vertical distance that is in contradiction with Rayleigh theory described by formula 2.36. Thus, we used Mie theory for the characterization of these results.

5.3 Determination of nanoparticle distribution function

We deposited a series of samples so as to carry out direct measurements of nanoparticle diameters. The samples were deposited under the same conditions we used in **Fig. 5.7** at the distance of 15, 25, 35 and 45 mm from the nozzle outlet. After analysis of the samples we can conclude that the deposited thin layers do not reflect the real picture of nanoparticle distribution in the plasma plume when there are no extraneous objects in contact with the plasma (substrate and substrate holder). The intensive working gas flow blows nanoparticles away from the centre to periphery of the sample.

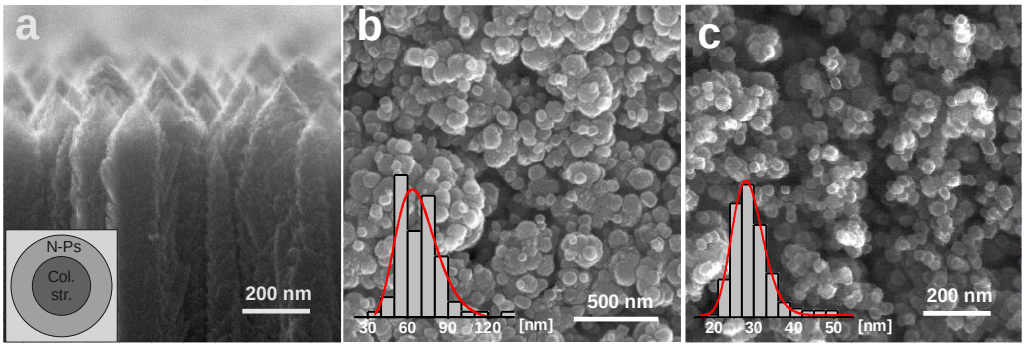

Fig. 5.8. SEM images of nanoparticles deposited at the distance of 35 mm from the nozzle. The histograms describe size distribution of nanoparticles fitted by log-normal function.

This effect manifests itself strongly for samples that were deposited close to the nozzle outlet. Nanoparticles were not found on the sample deposited at a distance of 15 mm from the nozzle. Other samples are characterized by the presence of two regions each with a different surface morphology: the nanoparticle region and the columnar structure [64] region. The formation of these structures occurs on the substrate and nanoparticles might be used as a building material. SEM image of columnar structures deposited at the distance of 15 mm from the nozzle is shown in **Fig. 5.8(a)**. The columnar structure region was observed in the centre and the nanoparticle rich region at the periphery of the sample, see the scheme in **Fig. 5.8(a)**.

SEM images of the sample deposited at the distance of 35 mm from the nozzle are shown in **Fig. 5.8(b,c)**. The measurements were taken in different places on the substrate; the position in **Fig. 5.8(b)** is closer to the centre of the sample than in **Fig. 5.8(c)**. The corresponding size distribution histograms with log-normal fit are added. These histograms will be used as references for comparison of calculated and measured size distribution functions (SDF).

For the estimation of nanoparticle SDF we used scattered ratio method which is similar to method described in [65]. The main advantage of this method is that it allows to exclude an absolute value of nanoparticle concentration as a parameter since it works with relative quantities. Instead of calculation of nanoparticle SDF from the ratio between scattered intensities at 90º for vertical and horizontal polarizations we made use of ratio between scattered intensities for 446 and 661 wavelengths from data in **Fig. 5.7**. The data were smoothed by the polynomial and then four ratios were obtained for angles 90º (both polarizations), 160º and 20º. The allowable error of the measurement was taken as 20 % of scattered intensity. Thus, the value of each measured scattered ratio r_m varied in a range from 0.8 I_{446} / 1.2 I_{661} up to 1.2 I_{446} / 0.8 I_{661}. The calculated scattered ratios r_c were obtained from the simulated dependencies of scattered intensity on nanoparticle size in **Fig. 5.7** and the log-normal SDF $f_{\ln}$ with mean nanoparticle size μ and standard deviation σ

$$f_{\ln} = \frac{1}{x\sigma\sqrt{2\pi}} \exp \frac{-(\ln x - \ln \mu)^2}{2\sigma^2}. \tag{5.2}$$

The value of r_c was estimated from the formula

$$r_c = \frac{\sum_{d_{\min}}^{d_{\max}} f_{\ln}(d) \cdot f_{I446}(d)}{\sum_{d_{\min}}^{d_{\max}} f_{\ln}(d) \cdot f_{I661}(d)}, \tag{5.3}$$

where $d_{\min}$ is minimal particle diameter, $d_{\max}$ is maximal particle diameter, f_{I446} and f_{I661} are dependencies of scattered intensity on nanoparticle size at the given scattering angle and polarization for scattered light wavelengths 446 and 661 nm, respectively. We were changing the parameters σ in a range from 0.01 up to 1 and μ from 1 up to 200 nm in search of the r_c which will match r_m within the taken error. The step of mean nanoparticle size and standard deviation was 1 nm and 0.01, respectively.

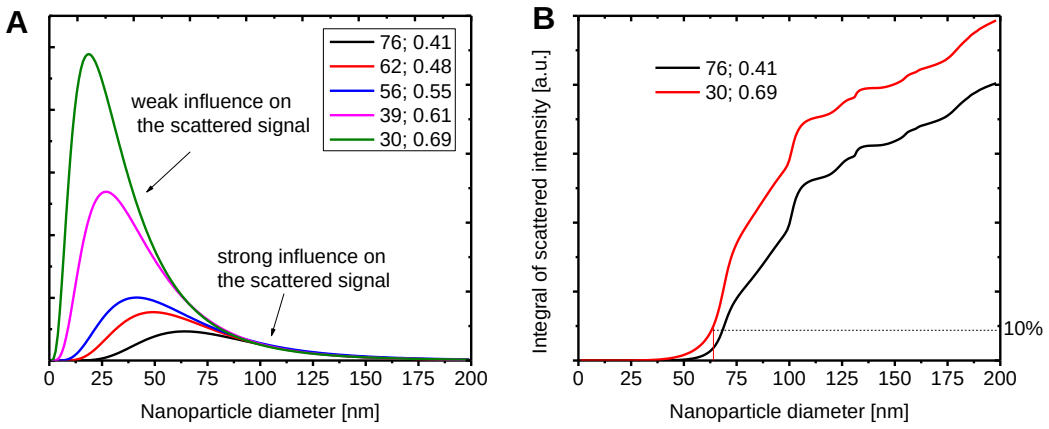

Fig. 5.9 Calculated nanoparticle size distribution functions (SDFs) for the data measured 35 mm from the cathode outlet (a) and the integral of the scattered intensity at 20º, horizontal polarization and λ= 446 nm for two different SDFs (b). The numbers in the legend correspond to the mean value of nanoparticle size (μ) and standard deviation (σ) of the log-normal SDF, respectively.

μ [nm]	σ	$r_{20\ hor}$	Error [%]	$r_{160\ hor}$	Error [%]	$r_{90\ hor}$	Error [%]	$r_{90\ vert}$	Error [%]
-	-	2.06	-	1.62	-	1.44	-	2.14	-
76	0.41	1.58	23	2.11	30	1.73	20	1.53	29
62	0.48	1.65	20	2.09	29	1.78	24	1.58	26
56	0.55	1.55	25	1.81	12	1.58	10	1.44	33
39	0.61	1.72	17	2.06	27	1.82	26	1.64	23
30	0.69	1.67	19	1.93	19	1.73	20	1.59	26

Tab. 5.1. Parameters of the nanoparticle SDFs with calculated scattered ratios and errors. Measured scattered ratios are given in a second row of the table. The lower indexes of the ratios *r* indicate the scattered angle and polarization.

Results of the calculated nanoparticle SDFs for data measured at 35 mm from the nozzle outlet are shown in **Fig. 5.9(a)**. The results consist of multiple solutions with different nanoparticle mean sizes and standard deviations that best match to the measured ratios. The more detailed information about calculated SDFs and errors of calculation is given in **Tab. 5.1**. The maximal error value of the calculation was 33 %. Calculated mean nanoparticle size varied in a range from 20 up to 80 nm. The interesting finding was that for the smaller mean nanoparticle size the standard deviation was bigger. SDFs were scaled to show that the "tails" of distributions are almost identical. We assume that these "tails" make the main contribution in a scattered signal and the signal from nanoparticles <50 nm can be neglected. In order to support this assumption we calculated the integral of scattered intensity at 20º and λ=446 nm as a function of maximal nanoparticle size for two different nanoparticle

SDFs, see **Fig. 5.9(b)**. The nanoparticles below 64 nm for the SDF with μ=30 and σ=0.69 generate only 10 % of the total scattered intensity. The similar results were obtained for SDF with μ=76 and σ=0.41, where the value of 10 % of intensity was generated by all particles with size <68 nm. The ratio between size distributions were kept as it is shown in **Fig. 5.9(a)**. The total scattered intensity at 20º for SDF with μ=76 and σ=0.41 is only 20 % lesser than one with μ=30 and σ=0.69.

The calculated results are rather in agreement with measured since the sizes of nanoparticles varied approximately in the same range. However, for the vertical distance <25 mm solutions were not found. It can be explained by the significant difference in the refractive index of nanoparticles since it is temperature dependent and, probably, the scattering light signal was affected by the discharge radiation or heightened temperature of the plasma flow. In latter case the imaginary part of the refractive index might be nonzero. The significant contribution in the light scattering can be made by the nanoparticles which stuck together in a process of collision creating agglomerates, which optically behave as one big particle with developed structure. Such processes caused the error in the characterization of nanoparticle SDF by Mie theory since it is valid only for spheroid particles

In some cases it is possible to obtain mean nanoparticle size and even SDF from the analysis of the XRD spectrum, using different methods [66]. All these methods are based on the shape of the diffraction peaks and are valid when crystalline domain sizes are identical to nanoparticle size. XRD spectra of the films deposited at the different vertical distances are shown in **Fig. 5.10** together with anatase and rutile reference lines. The crystallinity of the film decreases with the increase of the vertical distance until it becomes completely amorphous. Deposited crystalline films are mostly presented in the rutile phase (R110, R101, R111, R211). The ratio between anatase and rutile forms increases with increase of the vertical distance. Anatase shows itself more clearly in a sample deposited at the distance 25 mm from the nozzle (A101, A004). This indicates that the temperature of the plasma flow is high enough for crystallization since according to reports on TiO_2 phase transformation [57,58] the transition from anatase/amorphous film to rutile occurs at more than 600 ºC at low pressure conditions. Temperature measurements of the plasma plume by means of an optic fibre thermometer were discussed in section 4.2 and proved that temperature can exceed 300 ºC (the limit of the thermometer).

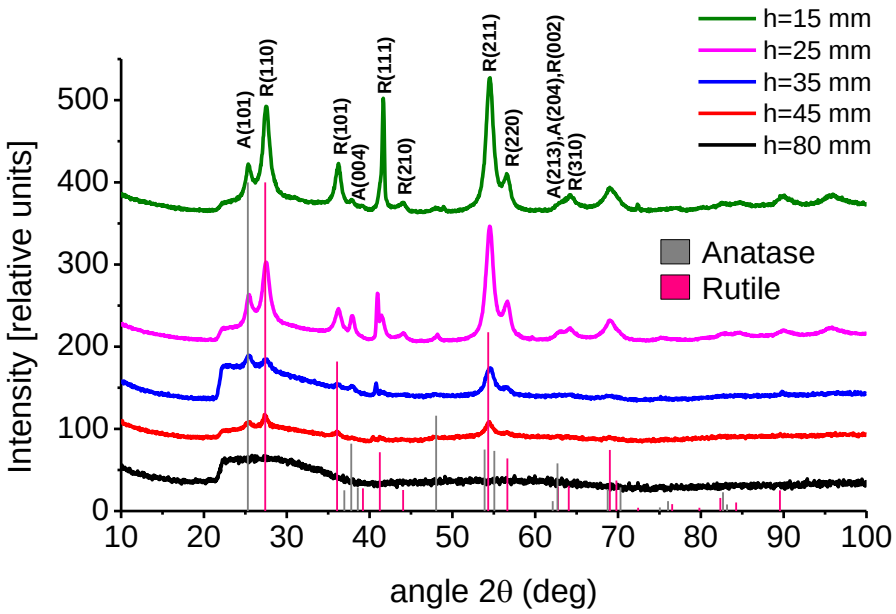

Fig. 5.10. XRD spectra of the films deposited at the different distances from the nozzle with reference lines of anatase A and rutile R.

Vertical distance [mm]	Anatase [nm]	Rutile [nm]
15	11	7
25	12	5.8
35	15	3
45	8	2.1

Tab. 5.2. Anatase and rutile crystalline domain sizes for the samples deposited at the different vertical distances.

The sizes of crystalline domains were determined for samples deposited at vertical distances of 15, 25, 35 and 45 mm. Instrumental resolution function was determined from the measurement of the lanthanum hexaboride (LaB_6) standard. The domain sizes were estimated in program FullProf by means of Reitveld method from the dimensional broadening of the diffraction peaks. Results are given in **Tab. 5.2**. The decreasing sizes of rutile domains and amorphous structure of the sample at the vertical distance of 80 mm indicate that crystallization probably takes place at the substrate and is more effective at higher temperature i.e. near to the nozzle. It indicates that the nanoparticle sizes and crystalline domain sizes in our case are not connected. Nevertheless, diffraction spectra confirmed titanium dioxide crystalline phase in the films.

5.4. 2D maps of the light scattered at the angle 90º

More detailed information about scattered light intensity distribution along the horizontal axis was obtained using digital photo camera. The complete 2D, i.e. vertical distance vs horizontal coordinate, intensity maps are shown in **Fig. 5.11**. Each 2D map was assembled from 10 horizontal profiles with the step of 5 mm. Profiles were extracted from photographs (see **Fig. 3.7(right)**) taken with different height of the laser beam. . The intensity scale was normalized to the maximum which is different for each 2D map. The intensity of the scattered light is colour-coded in the range from 0 (blue) to 1 (red) which corresponds to minimum and maximum of the intensity. The light from the discharge was subtracted using picture taken with laser switched off. Photos were saved in RAW format with 14 bit intensity

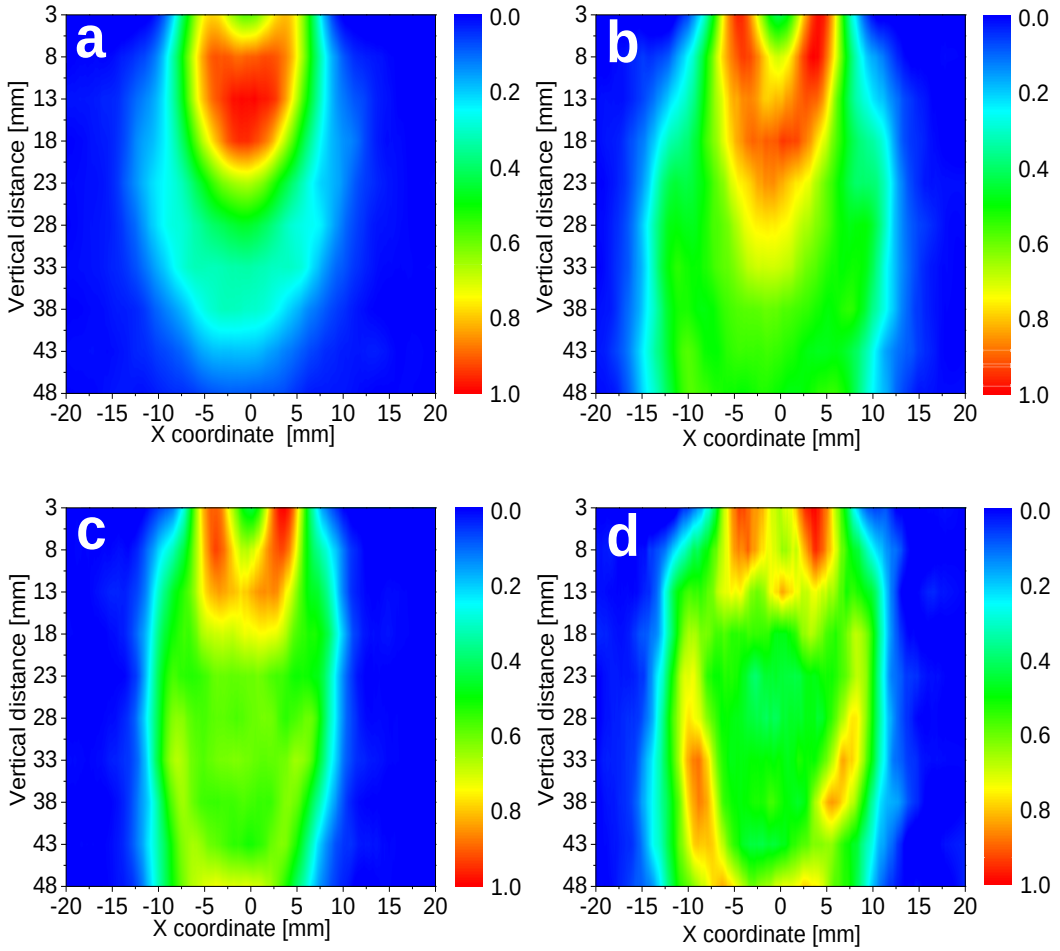

Fig. 5.11. 2D profiles of the scattered light intensity distribution measured under different discharge conditions: a) Discharge current 175 mA, pressure 60 Pa, argon flow 200 sccm, b) discharge current 175 mA, pressure 60 Pa, argon flow 400 sccm, c) discharge current 175 mA, pressure 100 Pa, argon flow 400 sccm, d) discharge current 400 mA, pressure 100 Pa, argon flow 400 sccm.

resolution. We used Origin 9.1 and Adobe Photoshop CS6 to extract the pixel lines along the laser beam, convert to grayscale and assemble a 2D map.

In each 2D map we observe the presence of the minimum in a proximity to plasma axis close to the nozzle outlet. The length of this minimum is mostly affected by the argon flow rate. Nanoparticles nucleation occurs further from the nozzle outlet because of high gas velocity near the plasma axis.

In **Fig. 5.11(c,d)** we observed a clearly distinguishable maximum of the scattered intensity at the outer layer of the plasma plume. Several physical processes may cause such particle distribution. The increased flow results in higher gas concentration inside of the hollow cathode. In this case the radial diffusion rate of sputtered titanium atoms is decreasing. Increased argon flow may also cause changes in flow regime that becomes more turbulent. The regime of the flow can be characterized by Reynolds number that is expressed as $R_e \sim \rho_g v$, where ρ_g and v is the gas density and velocity respectively. The measurements carried out under the relevant conditions by Bárdoš et.al. [53] by means of the Prandtl probe showed that flow velocity exceeded supersonic value in the proximity to the cathode.

Working gas density inside of the hollow cathode is hard to measure since the inner volume is very small. We assume that it is significantly higher than gas density inside of the main chamber. Increased turbulence leads to so called turbulent agglomeration [56] that strongly affects nanoparticle growth and clustering process. Better cooling of nanoparticles by means of working gas and cold oxygen atoms produces an additional impact that makes outer layer of plasma plume more favourable for synthesis of nanoparticles. This effect was discussed in [3] and section 4.4 where we found the reflection of such nanoparticle distribution in our deposited samples.

5.5. Titanium dioxide columnar structures in samples deposited for the nanoparticle size characterization.

The thin films structure of the samples with deposition parameters that correspond to **Fig. 5.11(a)** is depicted in **Fig. 5.12**. Morphology of the films which were deposited at the distances <35 mm from the nozzle is characterized by the spiky

columnar structures, see **Fig. 5.12(a)**. In **Fig. 5.12(b)**, which shows SEM image of the film deposited 45 mm from the nozzle, the spiky columnar structures are surrounded by the flat film. In the film deposited at a distance of 80 mm from the nozzle these spiky structures were not observed. We assume that the growth of spiky columns is facilitated by the interaction of a substrate with plasma plume.

The main factors of such growth are - in our opinion - intensive gas flow and heightened temperature. A gas flow greatly increases the migration of the deposited atoms/nanoparticles along the surface of the substrate. This helps them to find the place with the minimum of free energy i.e. launches processes of a self-organization. Probably, nanoparticles can serve as building blocks for the growth of these structures. In addition, the heightened temperature near the nozzle might cause the significant impact on the structure of the films. From the **Fig. 5.10** it is clear that the samples with a dominant region of the spiky columnar structures, especially for sample which was deposited at the distance of 10 mm from the nozzle, are highly crystallised and the dominant crystalline phase is rutile. It indicates that these columnar structures are represented by the rutile phase. The similar rutile columnar structures were deposited by RF magnetron sputtering in [64], which supports this assumption.

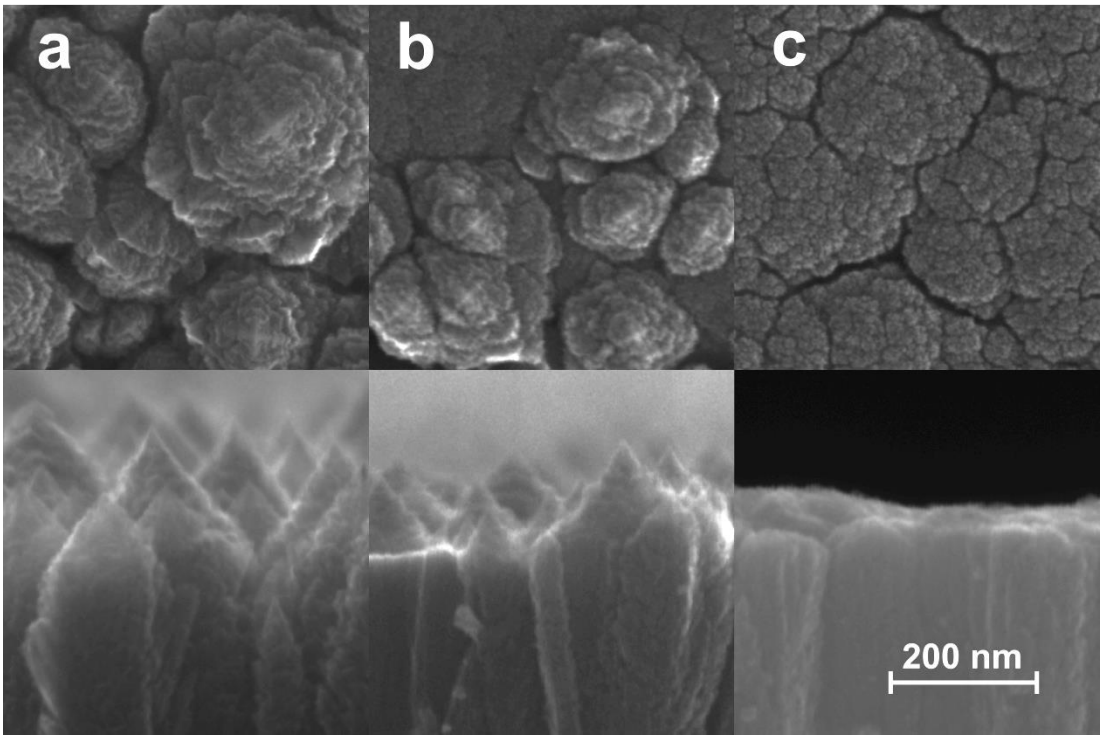

Fig. 5.12. Columnar structures we obtained under the same discharge conditions as in **Fig. 5.11(a)** under a different cathode-to-substrate separation: a - 15 mm; b - 45 mm; c - 80 mm.

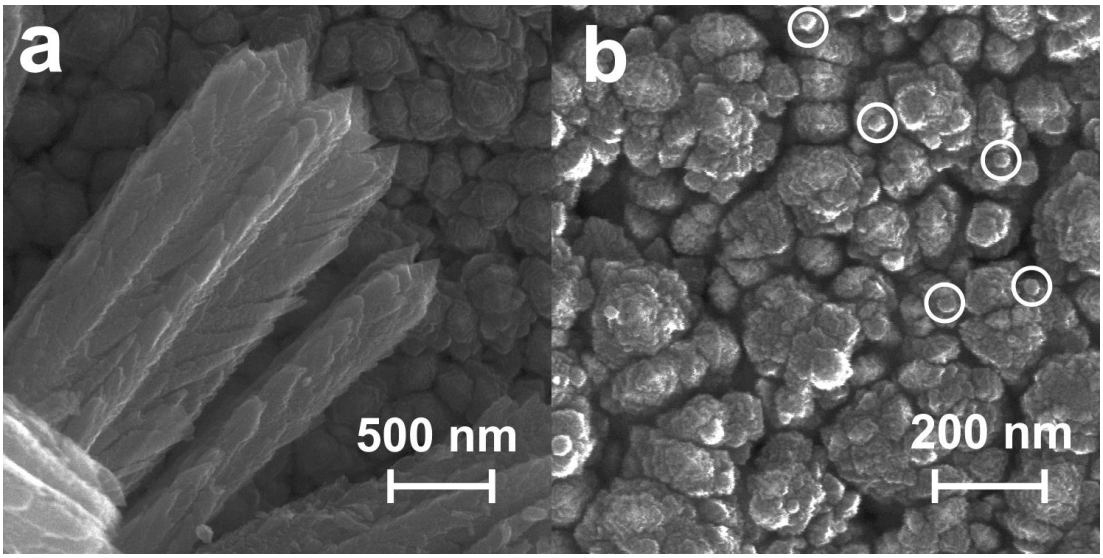

Fig. 5.13. SEM images of a) place near the scratch of columnar-structures-rich sample c) a transition region between the columnar-structure-rich and nanoparticle-rich regions of the sample.

The SEM image of the place near the scratch is given in Fig. 5.13(a). It shows that columnar structures have a bad adhesion to each other and can be easily detached. **Fig. 5.13(b)** exhibits the transition between columnar structure region and nanoparticle region. Nanoparticles are marked by the white circles.

6. The efficiency of titanium dioxide layers in dye-sensitized solar cells.

Dye sensitized solar cell (DSSC) technology provides an economical pathway to promote the photovoltaic technologies while conversion efficiencies reached up 13 % [7]. Semiconductors such as ZnO, SnO_2 and chalcogenides have been extensively studied as photoelectrodes due to their wide application in energy storage and environmental remediation. However, the titanium dioxide was recognized as a best solution for fabrication of the photo electrode in spite of its low electron transfer and enhanced charge recombination, because of its high stability and chemical resistance.

In DSSC system, a mesoporous TiO_2 thin layer provides a large surface area for the chemisorption of dye on the surface of the photo electrode. The typical thickness of a photo sensitive layer is in a range of units up to tens of μm. The most widely spread method of photo electrode production is sol-gel [67] process which allows to obtain mesoporous films with 20 nm diameter particles and porosity of 50 %, which can absorb the entire incident light and their power conversion efficiency can reach 11.2 % [13]. However, this is not single solution for the optimization of the surface area of the photo electrode [68]. The need for absorbing more light in DSSC was the driving force behind the development of mesoscopic semiconductor material.

The aim of this investigation was to evaluate the efficiency of TiO_2 thin layers deposited by means of the hollow cathode plasma jet in DSSCs produced from the low-cost materials. These results will show the perspective of the further investigation.

6.1. Deposition of the metal-oxide films in DC regime with supporting anode

For the deposition of non-conductive coatings the RF powered sputtering systems are commonly used because of several crucial advantages over DC powered systems. Among them is the possibility of the sputtering of non-conductive materials,

where there is no disappearing anode problem and the charge is not accumulating on the chamber walls or other inner parts of the vacuum system. However, DC discharge is much easier to exploit as it performs in stable deposition conditions with a well-defined cathode sputtering area and does not interfere with other electrical devices. In the case of short-term deposition of non-conductive thin films there were no issues with the HCPJ exploitation in DC regime (film thickness from several tens up to hundreds nanometres). The problems arose during a long-term deposition of titania thin film lasting several hours when the inner surfaces of the main chamber were gradually coated by a non-conductive layer. This resulted in the effective insulation of the anode followed by the interruption of a discharge. This effect was monitored as a decrease of the potential of any floating part immersed in the discharge, e.g. the floating sampling orifice of the mass-spectrometer. In some cases this resulted in the random migration of the anode's active part (i.e. the part carrying the discharge current) over the conductive parts inside of the main chamber, e.g. the sample holder, shutter, table, etc., depending on their distance from the cathode and the thickness of the insulation layer.

The TiO_2 photo electrode in DSSC has to be relatively thick, its thickness varies from units up to tens of μm. If we take into account the relatively low deposition rate, which reaches maximally several $nm \cdot s^{-1}$, the stability of the discharge during long deposition becomes an acute problem. To make the discharge stable, we introduced into the deposition chamber a supporting anode which was slightly positive with respect to the ground and therefore drained almost the whole

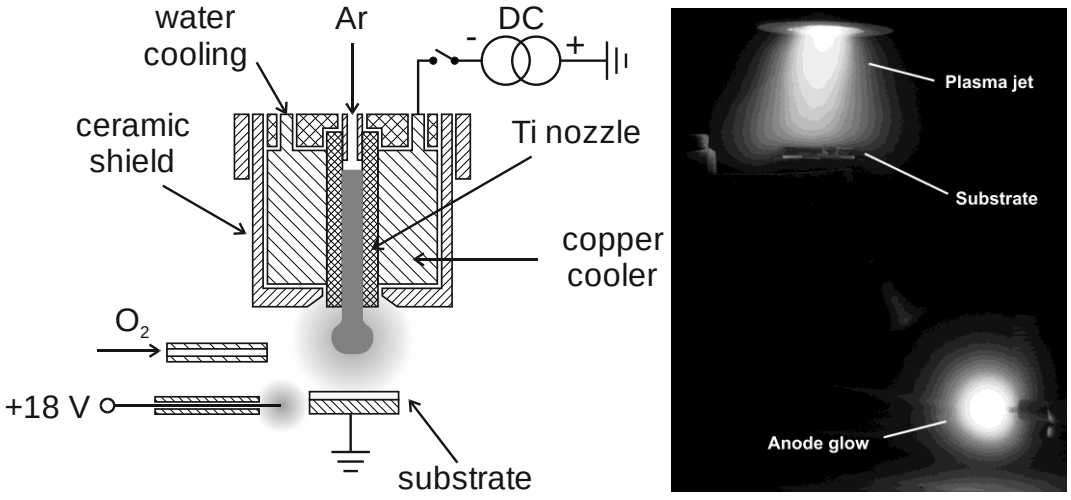

Fig. 6.1. The scheme of the HCPJ sputtering system with supporting electrode for deposition of metal-oxide films in DC mode (left) and photo of the system during the deposition (right).

electron current from the discharge.

The supporting anode was installed below the substrate holder as it is shown in **Fig. 6.1**. The supporting electrode is a cylindrical iron wire insulated by the ceramic shielding tube. The active part of the anode is 7 mm long and 1 mm in diameter. The anode was positively biased with respect to the ground (+18 V) by Agilent E3633A DC power supply that also enabled us to measure the supporting anode current separately from the cathode current. During the deposition the anode was continuously heated by the electron and, probably, negative ion (O-) currents which prevented the loss of conductivity. This supporting anode drained almost the whole current from plasma because of its positive bias and sharp geometry, which created the high electric field lines in front of its tip. The anodic instabilities due to the probable double layer formation around the supporting electrode did not cause fluctuations of the discharge current greater than 5 %. Consequently, we assumed that the influence of current fluctuations on the deposition process can be neglected.

The presence of the heated supporting anode may cause the uncontrolled doping of the TiO_2 thin layer by evaporated iron atoms (anode material). The EDX analysis was carried out in order to make sure that the elemental composition of the film corresponds to the pure titanium dioxide, see **Fig. 6.2**. The iron L_α, K_α and K_β lines are marked as references. The magnitude of the signal at the position of the iron reference lines remains at the level of noise. The presence of the silicon on the

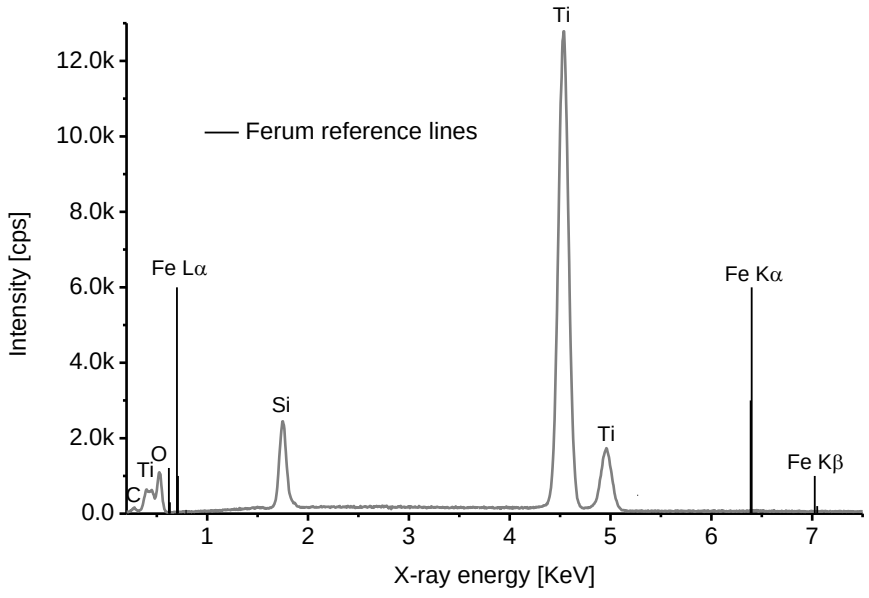

Fig. 6.2. EDX spectrum of the sample deposited with supporting anode with iron reference lines.

spectrum indicates that the penetration depth of this method is deeper than the thickness of the film and that we have detected the substrate. A small carbon peak corresponds to the impurities that emerged after the exposure of the sample to the atmosphere. It has been proven experimentally by XPS measurements of the samples deposited at the relevant conditions [3].

6.2. Investigation of factors which affect the efficiency of DSSCs

The main functional components of dye-sensitized solar cell are the photo electrode, dye-sensitizer, counter electrode and electrolyte.

First test TiO_2 photo electrodes we fabricated at the same conditions as were used in section 5.2 in order to make these experiments connected with the rest of results. The dimensions of electrodes we prepared were 17×15×2 mm. We deposited 4 photo electrodes at the distances 15, 25, 35 and 45 mm from the cathode nozzle, other conditions are given in the description of the **Fig. 5.9**. The closest sample had a problem with adhesion of the TiO_2 layer with electrode because it was overheated and as a result exfoliated. The layer of TiO_2 was inhomogeneous for the same reasons as were discussed in section 5.2. We tried to keep the constant thickness of the layers which was 18 μm.

The possible pigments to improve the photocathode sensitivity in a range of visible wavelengths are natural dyes, e.g. chlorophyll, carotenoid, flavonoid and anthocyanin, that are relatively easy to extract from natural products compared to synthetic dyes [69]. In our case the first photo electrodes were immersed in an aqueous solution of hibiscus for 10 minutes. The examples of the application of hibiscus in DSSC are given in [70–72].

An ideal counter electrode should have low electrical resistance and high electro catalytic activity towards the iodide/triiodide redox reaction, being stable and optionally transparent. For highly efficient DSSC the thin Pt layer is used as a catalyst for the reaction of reduction of iodine due to its superior catalytic activity and chemical stability. We made use of carbon (graphite) because it is cheap and the process of counter electrode fabrication is much easier.

The electrolyte provides the internal electric ion conductivity in DSSC by diffusing within the porous TiO_2 layer and therefore it plays an important role in

determining the cell performance. In our case we used ethylene glycol with addition of I^- ions.

Photovoltaic tests were carried out by measuring the I-V characteristic under simulated AM 1.5 G solar illumination at 100 $mW \cdot cm^{-2}$. Since the photocurrent is proportional the solar cell surface area the current density is plotted in I-V characteristics. The results are shown in **Fig. 6.3**.

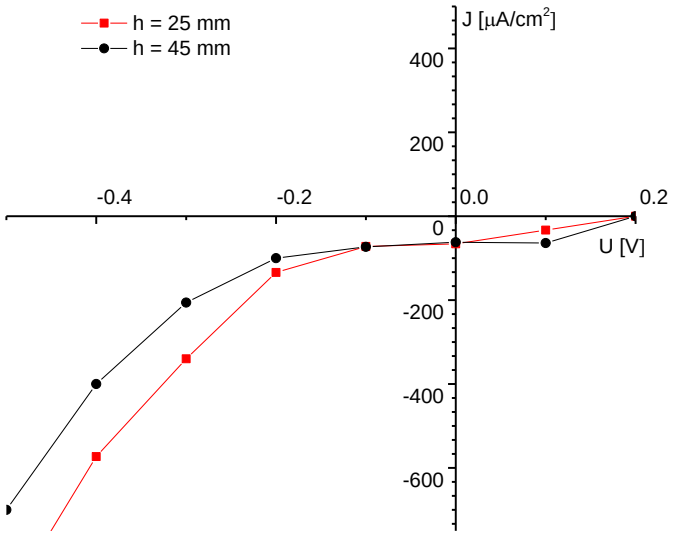

Fig. 6.3. I-V characteristics of the first assembled solar cells. The photo electrode of the solar cell was deposited 25 mm (red) and 45 mm (black) from the nozzle outlet.

The value of the short current density which was calculated from the solar cell active area and total cell current is $J_{sc} = 35\ \mu A/cm^2$ and open circuit voltage $U_{oc} = 0.2$ V for both solar cells. The calculated efficiency from formula (2.35) and the fill factor from formula (2.36) were $\eta \approx 0.0004$ % and $FF \approx 50$ % respectively. The calculations might have a high error since we had only three measured points in a forth quadrant of the characteristics.

The main problems we faced during the assembly and measurement of test cells were contacts between wires and transparent ITO electrodes and bad adhesion of TiO_2 film with ITO layer after the immersion of photo electrodes in a hibiscus solution.

To improve electric contacts the small part of photo electrodes was covered by Al foil during the deposition and remained clean. The contact with bigger area was created by aluminium foil pressed to this ITO area, which is marked as "*" in **Fig.**

6.4. We used the whole glass electrode to make it easier to assemble and manipulate. The photos of counter electrode (a), photo electrode (b) and dye sensitized photo electrode (c) are shown in **Fig. 6.4**. The results of photovoltaic tests with improved cells are depicted in **Fig. 6.5**.

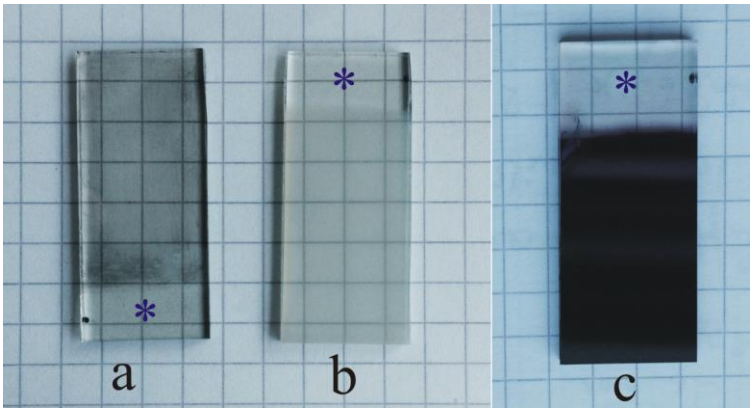

Fig. 6.4. The photo of counter (a) and photo electrodes (b). The photo electrode after immersion in hibiscus mixture (c). The places for electric contact are marked as "*".

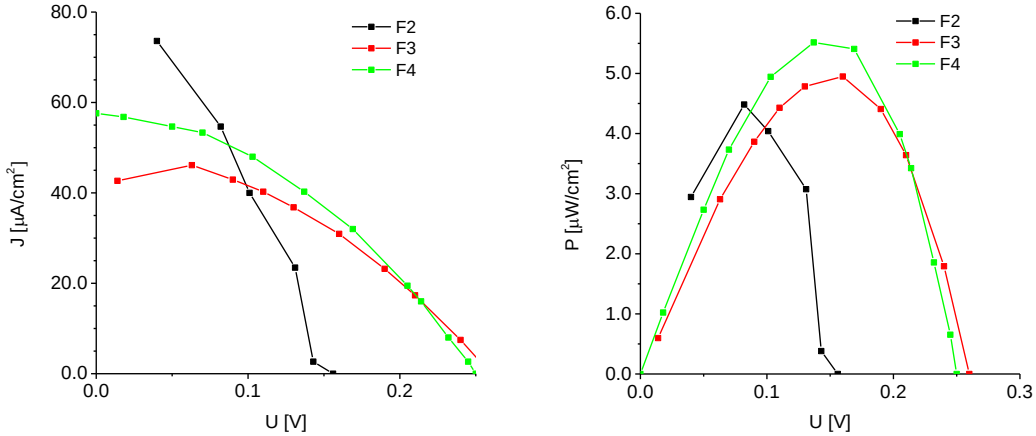

Fig. 6.5. I-V characteristics of the second series of solar cells (left) and dependencies of the produced power on cell voltage (right). Photo electrodes were deposited at the vertical distance of 25, 35 and 45 mm for DSSC samples F2, F3 and F4, respectively.

The sample F2 deposited at the vertical distance of 25 mm from the cathode did not perform well, probably, because of the bad adhesion of the TiO_2 with conductive ITO layer caused by the higher plasma temperature at this position. The efficiency of samples F3 and F4 was 0.009 % and 0.01 %; the fill factor 41 % and 38 %, respectively.

To achieve a higher cell efficiency an alternative counter electrode covered the by carbon soot was used instead of the graphite from the pencil lead. Carbon layer

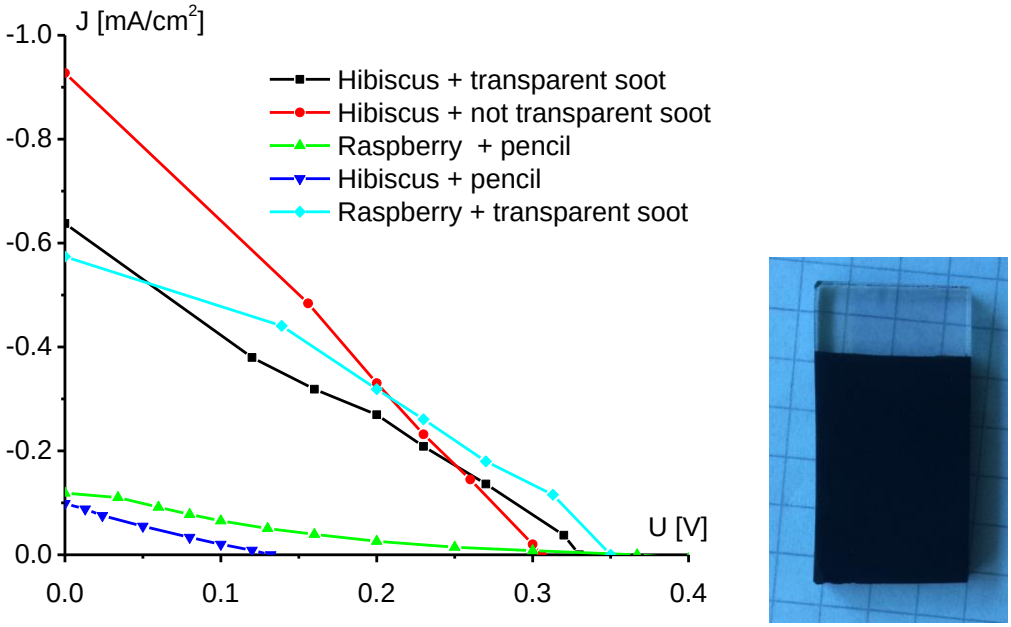

Fig. 6.6. The fourth quadrant of I-V characteristics with different dye sensitizer and counter electrode (left). The carbon black counter electrode (right).

was created on the counter electrode using the candle. The analysis of the candle soot produced from candle wax is given in [73]. The candle soot is treated as a cheap alternative to the carbon black. It is easy to produce in the laboratory but it contains unburned hydrocarbons as impurities. Examples of the carbon black application in DSSCs are given in review [74]. Samples of soot counter electrodes were prepared with two thicknesses: the nontransparent were 10 μm thick and the transparent 1 μm.

Sample	U_{oc} [V]	J_{sc} [mA/cm^2]	FF [%]	η [%]	R_s [Ω]
Hibiscus + pencil	0.132	0.098	21	0.0028	642
Raspberry + pencil	0.367	0.118	15	0.0066	2525
Hibiscus + transparent soot	0.330	0.630	26	0.054	414
Raspberry + transparent soot	0.350	0.573	32	0.064	490
Hibiscus + non transparent soot	0.306	0.927	27	0.0763	255

Tab. 6.1. Parameters of the solar cells with I-V characteristics described in **Fig. 6.6**.

The TiO_2 layers were deposited for 10 hours under the laminar flow conditions: p=20 Pa, $flow_{Ar}$=100 sccm, $flow_{O2}$=3 sccm, I=300 mA and h=30 mm. We also added

the second natural dye made of raspberries. Moreover, photo electrodes were annealed in muffle furnace at the atmospheric conditions under 400 ºC. In section 4.6 it was shown that such annealing causes the phase transformation to anatase which has better light absorption in UV region.

The fourth quadrant of the I-V characteristic and the photo of the carbon soot counter electrode are shown in **Fig. 6.6**. The combinations of counter electrode and dye used are marked in the legend.

From **Fig. 6.6** and **Tab. 6.1** we made a several significant conclusions. The dependence of the open circuit voltage on a type of counter electrode did not show a clear result. On the contrary, the use of different counter electrodes has shown the clear effect on the total cell current – with increase of a carbon thickness we achieved higher I_{sc} values which is in agreement with reported results [75]. It can be explained by the larger active surface of the electrode which affects the reduction rate of I_3^- ions, see section 3.5. A raspberry dye has shown slightly better conversion efficiency. Solar cells had a low fill factor which we explain by the higher electrode sheet resistance of used ITO electrodes. The series resistance of solar cells was calculated from the fourth quadrant using the area under I-V curve

$$R_{s,in} = 2 \cdot \left(\frac{U_{oc}}{J_{sc}} - \frac{A}{J_{sc}^2} - \frac{k_b T}{q} \cdot \frac{1}{J_{sc}} \right), \tag{6.1}$$

where A is an area under I-V curve in fourth quadrant, see **Fig. 6.7**. The second method of estimation of this quantity is calculation from the shift of the J_{sc} under the different illumination. The principle of the estimation is shown in the third quadrant of **Fig. 6.7**. The series resistance is estimated from the formula

$$R_s = \left| \frac{\Delta U_3}{\Delta J_{sc}} \right|. \tag{6.2}$$

Used quantities ΔU_3 and ΔJ_{sc} are graphically explained in **Fig. 6.7**. The third method is based on the estimation of dU/dI from the linear part of the I-V curve in the first quadrant at dark conditions, which was not measured. First two methods are in agreement with each other. Estimated values of series resistance and are similar: 391 Ω from the fourth quadrant and 386 Ω from the third quadrant. The series resistances of tested solar cells had high values and badly affected their efficiency.

Usual value of series resistance in high-efficient solar cells varies in a range from units up to several tens of Ohm.

Not only the serial but also the shunt resistance has an influence on the efficiency of solar cell. First we tried to improve the shunt resistance value which should be as high as possible. Shunt resistance characterizes the interconnection between conductive ITO layers of counter and photo electrodes. To make this resistance higher we defined the distance between electrodes by surrounding the photo-active layer by the insulation tape. The results are given in **Fig. 6.7**. The value of shunt resistance is estimated from dU/dI at U=0 (green line) using I-V characteristic measured under a dark conditions (red curve). Its value was ~100 kΩ (green line), which indicated the absence of interconnection between electrodes.

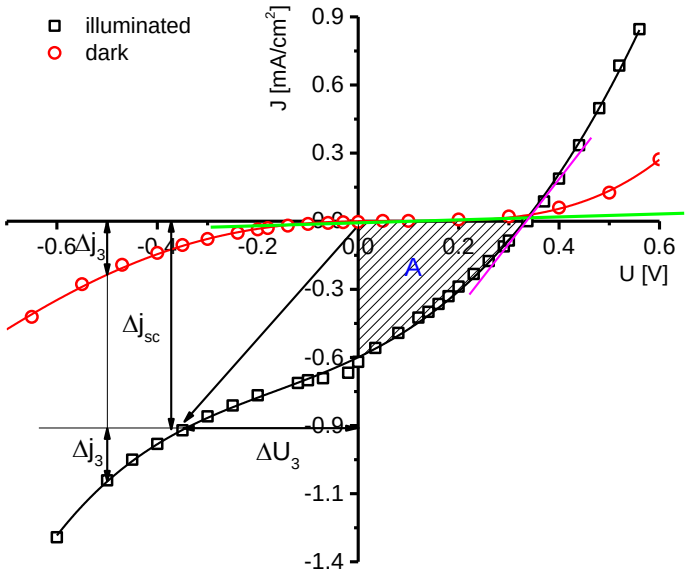

Fig. 6.7. The repetition of the measured hibiscus + non transparent soot I-V characteristic with improved parallel resistance.

The series resistance problem is much harder to solve. From the reported data [76] small size solar cells are used to obtain a high conversion efficiency in nonindustrial studies. Less than 1 % efficiency has been achieved when 10×10 cm^2 large-scale cell has been fabricated with the transparent conductive oxide film but without the collecting electrode [76]. Collecting electrodes are used to connect several smaller solar cells in parallel to decrease the series resistance of transparent conductive oxide layer. Therefore, the sheet resistance R_{ITO} of our ITO layer plays the important role. It represents additional series resistance in the cell

$$R_T = R_{ITO} \cdot \frac{L_{sc}}{W}, \tag{6.3}$$

where W is the width and L is the length of solar cell. The ITO layer on the top of the glass has the sheet resistance of 10 Ω. In order to minimize the series resistance effect the active area of solar cells was decreased which promised also to improve their *FF*. The active area varied from 0.21 cm^2 up to 0.49 cm^2.

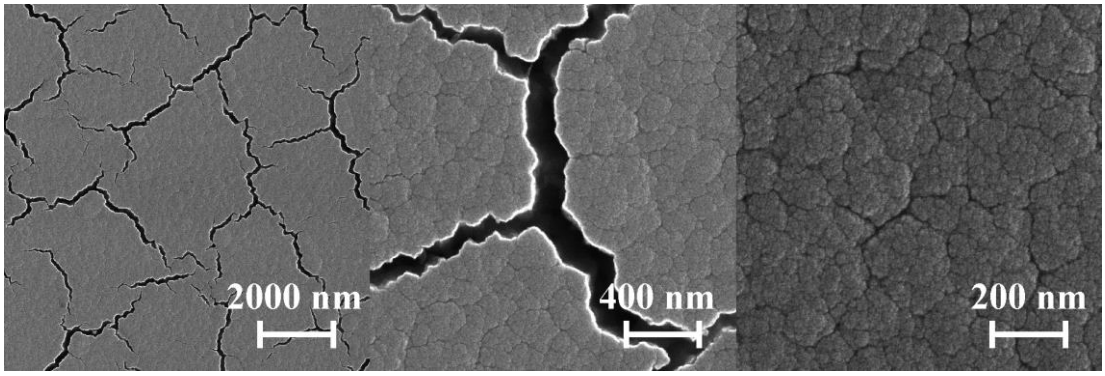

Fig. 6.8. SEM surface scans of the TiO_2 layer of the photo electrode deposited under I=300 mA, p=25 Pa, $Flow_{Ar}$=120 sccm, $Flow_{O2}$=3 sccm, h=35 mm. Deposition lasted 6 hours.

Surfaces of both photo and counter electrodes were investigated by means of SEM. Nanocracks were observed on the surface of photo electrode, as shown in **Fig. 6.8**. They were probably created by the thermal expansion of the glass substrate.

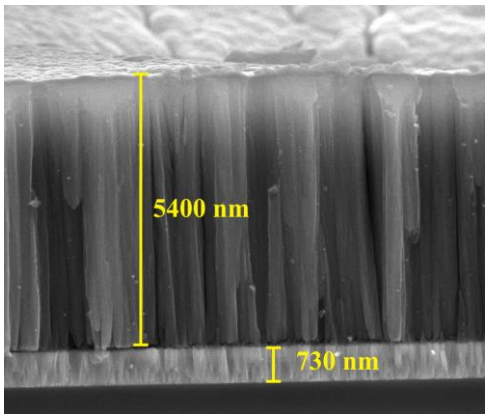

Fig. 6.9. SEM cross section scan TiO_2 layer of the counter electrode deposited by means of the candle.

The TiO_2 film was deposited in a form of columnar structures that are tightly connected with each other, see **Fig. 6.9**. The ITO layer was clearly distinguishable and had a thickness of about 730 nm. The scan of carbon black layer is depicted in **Fig. 6.10**. It consists of the thick layer of carbon nanoparticles with diameter of several tens of nm. Such nanostructure has an extremely high effective area and subsequently serves as a good catalyst for reduction of I_3^-.

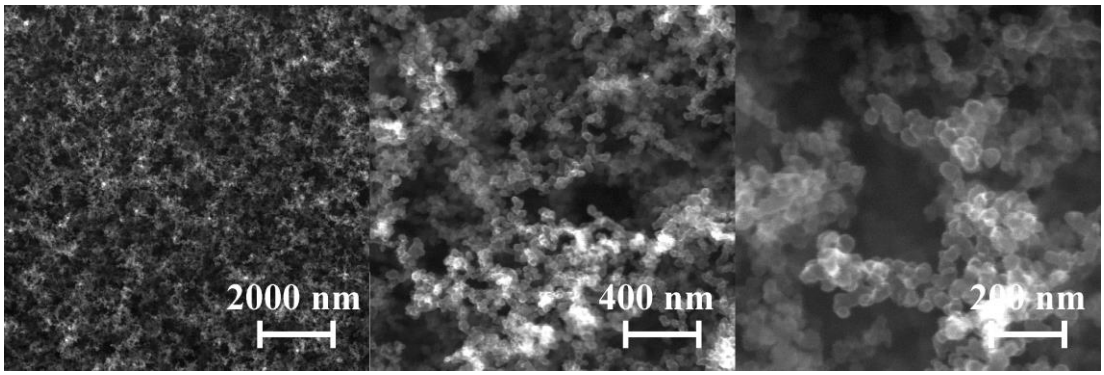

Fig. 6.10. SEM surface scans of the carbon black layer of the counter electrode deposited by means of the candle.

To check the purity of the carbon soot layer the EDX measurement was carried out, see **Fig. 6.11**. This method does not show the chemical bonds between atoms in the film, however, the rough concentration of each element can be obtained. The highest peak corresponds to the carbon (red reference line). The second highest peak belongs to the developed spectrum of indium and is overlapped with tin which both correspond to ITO layer. The presence of silicon indicates that the glass substrate was detected.

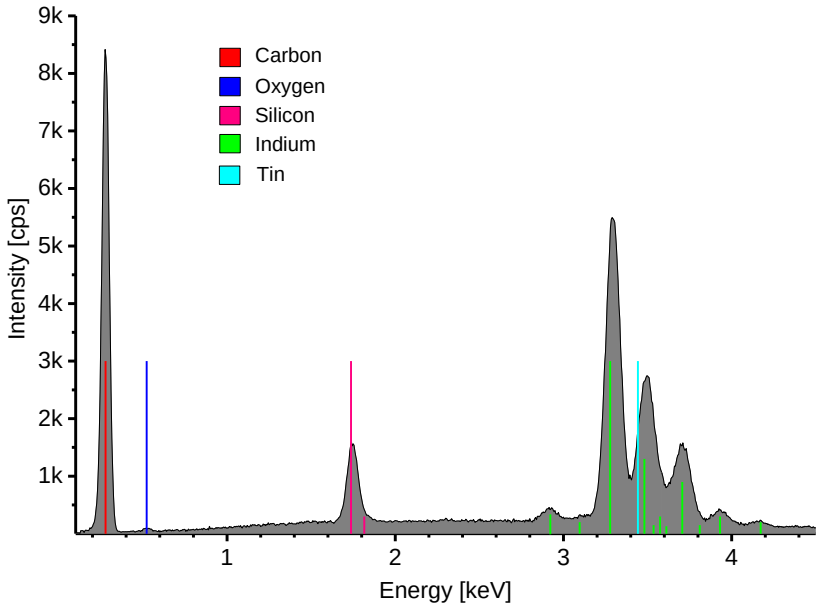

Fig. 6.11. EDX patterns of the carbon soot layer on the top of the counter electrode.

The method of the measurement of I-V characteristics was significantly improved using the precision source/measuring unit Keysight B2901A connected to PC. In this case the usage of the voltage divider in the electrical scheme shown in **Fig. 2.12** was not necessary.

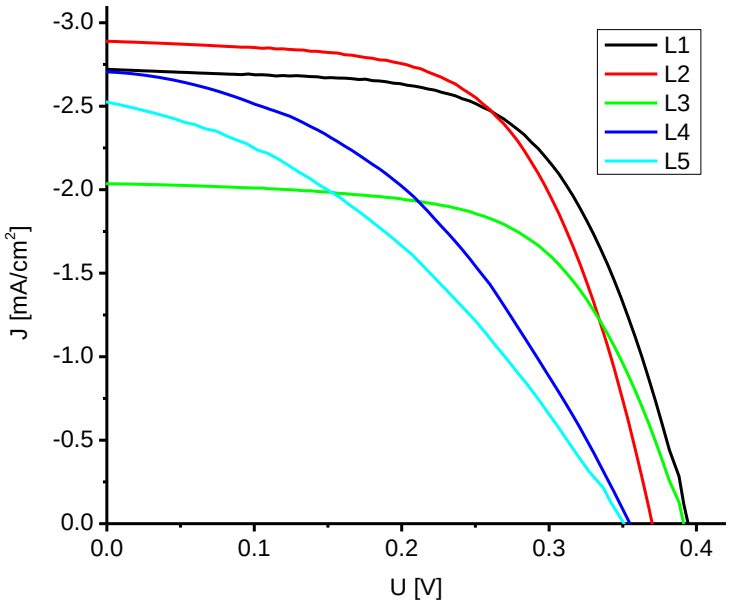

Fig. 6.12. Fourth quadrant of the I-V characteristics of DSSCsamples L1, L2, L3, L4 and L5.

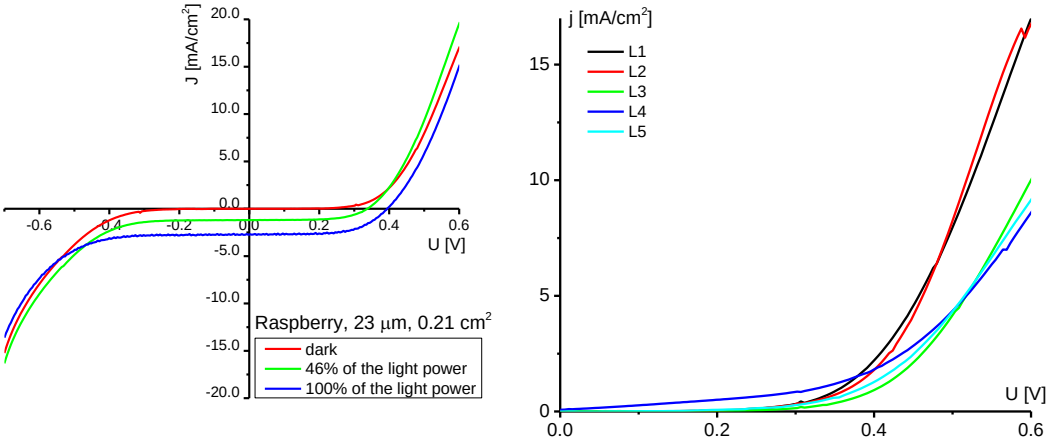

Fig. 6.13. I-V characteristics of the solar cell at dark, 46 % and 100 % of AM 1.5 G illumination power (left) and the first quadrant of I-V characteristics of the samples given in **Tab. 6.2** (right).

№	Dye-sensitizer	AA [cm^2]	TiO_2 thickness [μm]	I_{sc} [mA]	U_{oc} [V]	FF [%]	η, [%]	R_s, [Ω]
L1	rapsberry	0.21	20	2.72	0.393	61.7	0.66	10.9
L2	hibiscus	0.22	20	2.88	0.370	60.6	0.64	11.0
L3	hibiscus	0.48	20	2.03	0.391	61	0.48	18.5
L4	rapsberry	0.49	5.4	2.7	0.355	42.3	0.41	22.7
L5	hibiscus	0.36	5.4	2.53	0.350	37.4	0.33	21.4

Tab. 6.2. Parameters of solar cells with a different active area AA, TiO_2 thickness and improved series resistance.

TiO_2 photo electrodes were deposited with two thicknesses: 5.4 μm and 20 μm. Deposition lasted 6 hours and 22 hours, respectively, under I=300 mA, $flow_{Ar}$=120 sccm and p=25 Pa.

I-V characteristics of the DSSC samples with different surface area and improved series resistance are depicted in **Fig. 6.12** and **6.13**. The parameters of solar cells are shown in **Tab. 6.2**. The aforementioned improvements resulted in almost one order better conversion efficiency of the solar cells. The maximum of conversion efficiency was 0.66 % for the sample with 0.21 cm^2 active area AA, raspberry dye and thickness of 20 μm. In comparison with other relevant results with given natural dyes [70,71], higher results were achieved in [72], η = 1.5 % with raspberry dye and η = 0.75 % with hibiscus dye. However, in this work the Pt counter electrode was used which is much better but more expensive photo catalyst than carbon soot.

Samples with lower active area performed much better series resistance which was calculated from the slope of the linear part of I-V characteristics measured in the dark from the first quadrant, see **Fig. 6.13 (right)**. The series resistance was greatly improved in comparison with our previous samples with larger active area. Higher thickness of the TiO_2 film of 20 μm had also positive effect on the conversion efficiency. It is explained by the better light absorption. However, thicker films have higher probability of the electron recombination, thus the thickness of TiO_2 layer is the parameter that should be optimized to achieve the highest light conversion efficiency. Samples with TiO_2 layer thickness of 20 μm have much better fill factor which is comparable to commercial solar cells.

7. Conclusions

In this work we have investigated deposition of Ti and TiO_2 thin films by means of the DC hollow cathode plasma jet. The broad variety of parameters which are involved in the deposition process makes possible to obtain thin layers with different surface morphology. Unlike other deposition techniques based on the ion sputtering, the plasma jet has a continuous flow of gas. This allowed us to achieve higher chemical purity of the thin films and softer control of the deposition conditions.

The investigation of thin films was carried out from the point of view of processes in plasma, since plasma is a source of the sputtering matter. Experimental system was equipped by the cylindrical Langmuir probe and quadrupole mass spectrometer.

The Langmuir probe diagnostics was focused on turbulent regime of the flow since laminar regime has been already investigated in [50]. We were interested in a distribution of the electron density, charged particle temperature and plasma potential along the horizontal axis at the position of the deposited samples. The important conclusions about the impact of plasma on the surface morphology based on the measured ion and electron temperature and charge concentration are given in section 4. The electron energy is at rather low level (~0.3 eV) at the place of thin film deposition. At used pressure range the ion energy is much lower than the electron energy in HCPJ plasma since the momentum transfer between neutral atoms and ions is much more effective and is of the same order as the neutral gas temperature. We assume that plasma has more significant effect on nanoparticle charge since at high values of the discharge current the value of electron concentration reaches 10^{18} m^{-3} at the neutral pressure of 100 Pa. Nanoparticles which are located in a highly ionized plasma plume region can be negatively charged due to the higher electron mobility. In this case their dynamics is affected by the electric field.

The ion composition in the discharge was measured by quadruple mass spectrometer. Time resolved measurements of the plasma composition and positive ion mass spectrum were discussed in section 4.3. The main conclusion concerned the unstable behaviour of the sputtering rate during the first minutes of sputtering and the purity of the experiment. The signal from impurities was exponentially decreasing in time because pure titanium layers effectively absorb active gases.

Another important parameter of a deposition process is the neutral gas temperature. It plays a crucial role in formation of nanoparticles in plasma plume and affects the structure of deposited thin layers. The used fibre optic thermometer is described in section 3.3. We have measured neutral gas temperature in both laminar and turbulent regimes under the different values of the gas flow rate, discharge current, pressure and vertical position of HCPJ. The high value of the temperature gradient along horizontal plasma axis was observed in a turbulent regime of the flow. In some experiments the temperature was high enough to launch the process of annealing and crystallization of the thin films. The upper temperature of 300 ºC limits thermometer usage near the nozzle exit and at high discharge currents.

The thin films investigation was focused on characterization of the morphology, chemical composition and crystalline structure of titanium and titanium dioxide thin layers. We have confirmed that HCPJ can be used as a nanoparticle source. Morphology was studied by means of AFM and SEM. Results which were obtained in pure argon have shown a presence of nanoparticles with the mean diameter of several tens nm. In some of samples we observed the presence of bigger group of nanoparticles with diameter 80–110 nm.

The dependencies of the root mean square roughness and nanoparticle size of thin films on the working gas flow rate and discharge current were investigated. Both particle size and root mean square roughness gradually increased with argon flow rate. Dependencies on discharge current have shown the decrease of particle size with current and undefined root mean square roughness dependency. Explanation of these results was based on the influence of high temperature; the respective considerations were discussed in detail in section 4.3. Samples deposited at high flow rates were inhomogeneous. In the centre of the sample small nanoparticles (several tens of nm in diameter) were observed while large agglomerated particles (several hundreds of nm in diameter) were found in the periphery of the sample. The possible reasons of such structure were discussed in terms of flow dynamics and temperature at the end of section 4.3.

The chemical composition of the surface of samples deposited by Ti and TiO_x layers was studied by X-ray photoelectron spectroscopy. Together with the titanium and oxygen the carbon atoms were detected but the peak corresponding to chemical bond of carbon with titanium was not present. From this fact we concluded that the carbon content originated from the exposure of the sample to air atmosphere after

deposition. Consequently, the deposited films were of high purity. The pure Ti and TiO_x deposited layers showed almost identical XPS spectra since the Ti sample surface was oxidized almost instantly after the exposure to the air.

Energy dispersive analysis was carried out in order to prove that stoichiometry of thin films corresponds to titanium dioxide. The results have shown that even relatively small oxygen flow rate of 0.5 sccm is enough for complete oxidation of titanium. Results of XPS and EDX measurements are given in section 4.5.

The crystalline structure of the films was studied using XRD technique. The results indicated that crystallisation occurred when the deposited film was in contact with plasma at the high values of the discharge current and working gas flow rate. At these conditions TiO_2 films contained both rutile and anatase phases. Rutile phase was dominant. The films which were deposited at the low flow rates below 120 sccm were amorphous. However, after annealing in a muffle furnace they turned into pure polycrystalline anatase. The crystallinity studies were discussed in detail in sections 4.6 and 5.4.

During long depositions of titanium dioxide thin films we faced with a problem of discharge stability. It was caused by covering of anode, represented by the grounded discharge chamber and its internal metal parts, by the nonconductive TiO_2 layer. This caused a problem with the charge outflow. Sometimes the current was concentrated on a small area which was heated by this flow. To prevent uncontrolled migration of this anode active part along the surface of the main chamber we introduced the supporting anode with a small positive bias which was preferred by the discharge.

The aggregation of nanoparticles in a plasma plume was studied using a new technique based on scattering of the laser beam on nanoparticles in plasma. We have constructed comparatively cheap and simple experimental set up which consisted of red or blue laser diode powered in pulsed regime at 1 kHz and three detectors: photodiode, optical spectrometer and digital photo camera. We detected the polarized light scattered to characteristic directions, compared results with the scattering theory and found out how different parameters affect the intensity of scattered signal. We also attempted to estimate the particle sizes from the measured scattered light intensities using scattering ratio method.

The presence of nanoparticles on samples deposited at the same conditions as were used for experiments with laser light scattering was investigated by means of

SEM. From SEM images the sizes of nanoparticles were calculated and compared with sizes from the laser scattering. We concluded that calculated results are rather in agreement with those measured by SEM. Nanoparticles were not detected on samples which were close to the cathode nozzle; presumably they were removed by the intensive argon flow. The observed rutile columnar structure motivated the structural analysis of the deposited thin films. The crystallinity was represented mostly by the rutile phase and had a tendency to decrease with increase of cathode-to-substrate separation. This was explained in terms of temperature influence. The results and discussions are given in section 5.

The majority of photo electrodes for dye-sensitized solar cells use titanium dioxide layer, which is their main functional part. We tested thin TiO_2 layers deposited by HCPJ in solar cells. Samples of DSSCs for photovoltaic test were assembled from low-cost materials. The maximum of conversion efficiency and fill factor was 0.66 % and 62 %, respectively. These results indicated the high perspective of further investigation.

Bibliography

[1] Hubička Z 2012 *The Low Temperature Plasma Jet Sputtering Systems Applied for the Deposition of Thin Films* (Olomouc: Univerzita Palackého v Olomouci)

[2] Hippler R, Kersten H, Schmidt M and Schoenbach K-H 2008 *Low Temperature Plasmas: Fundamentals, Technologies and Techniques* vol 1 (Berlin: Wiley-VCH)

[3] Perekrestov R, Kudrna P and Tichý M 2015 The deposition of titanium dioxide nanoparticles by means of a hollow cathode plasma jet in DC regime *Plasma Sources Sci. Technol.* **24** 035025

[4] Tang Y, Zhang Y, Deng J, Wei J, Tam H L, Chandran B K, Dong Z, Chen Z and Chen X 2014 Mechanical force-driven growth of elongated bending TiO_2-based nanotubular materials for ultrafast rechargeable lithium ion batteries *Adv. Mater.* **26** 6111–8

[5] Wang L, Nie Z, Cao C, Khalid S, Wu Y and Xu X 2016 Carbon-wrapped TiO_2 nanocubes exposed with (001) active facets for high-rate and long-life lithium-ion batteries *J. Power Sources* **302** 259–65

[6] Li L, Yan J, Wang T, Zhao Z-J, Zhang J, Gong J and Guan N 2015 Sub-10 nm rutile titanium dioxide nanoparticles for efficient visible-light-driven photocatalytic hydrogen production *Nat. Commun.* **6**

[7] Mathew S, Yella A, Gao P, Humphry-Baker R, Curchod B F E, Ashari-Astani N, Tavernelli I, Rothlisberger U, Nazeeruddin M K and Grätzel M 2014 Dye-sensitized solar cells with 13% efficiency achieved through the molecular engineering of porphyrin sensitizers *Nat. Chem.* **6** 242–7

[8] Hashmi S G, Ozkan M, Halme J, Misic K D, Zakeeruddin S M, Paltakari J, Grätzel M and Lund P D 2015 High performance dye-sensitized solar cells with inkjet printed ionic liquid electrolyte *Nano Energy* **17** 206–15

[9] Ullmann M, Friedlander S K and Schmidt-Ott A 2002 Nanoparticle formation by laser ablation *J. Nanoparticle Res.* **4** 499–509

[10] Tabrizi N S, Ullmann M, Vons V A, Lafont U and Schmidt-Ott A 2009 Generation of nanoparticles by spark discharge *J. Nanoparticle Res.* **11** 315–32

[11] Jiang J, Chen D-R and Biswas P 2007 Synthesis of nanoparticles in a flame aerosol reactor with independent and strict control of their size, crystal phase and morphology *Nanotechnology* **18** 285603

[12] Haberland H, Karrais M and Mall M 1991 A new type of cluster and cluster ion source *Z. Für Phys. At. Mol. Clust.* **20** 413–5

[13] Grätzel M 2004 Conversion of sunlight to electric power by nanocrystalline dye-sensitized solar cells *J. Photochem. Photobiol. Chem.* **164** 3–14

[14] Thanh N, Rees H and Rosenzweig Z 2002 Laser-based double beam absorption detection for aggregation immunoassays using gold nanoparticles *Anal. Bioanal. Chem.* **374** 1174–8

[15] Miles R B, Lempert W R and Forkey J N 2001 Laser Rayleigh scattering *Meas. Sci. Technol.* **12** R33

[16] Bruno A, Ossler F, de Lisio C, Minutolo P, Spinelli N and D'Alessio A 2008 Detection of fluorescent nanoparticles in flame with femtosecond laser-induced fluorescence anisotropy *Opt. Express* **16** 5623–32

[17] Lin J-H and Tseng W-L 2015 Ultrasensitive detection of target analyte-induced aggregation of gold nanoparticles using laser-induced nanoparticle Rayleigh scattering *Talanta* **132** 44–51

[18] Chen F F 1984 *Plasma Physics* vol 1 (Springer)

[19] Raizer Y P 1991 *Gas Discharge Physics* (Berlin: Springer-Verland)

[20] van de Hulst H C 1981 *Light scattering by small particles* (New York: Dover Publications, inc.)

[21] Bohren C F and Huffman D R 1998 *Absorption and scattering of light by small particles* (New York: Wiley)

[22] Kerker M and Loebl E M 1969 *The scattering of light, and other electromagnetic radiation* vol 16 (New York: Academic Press)

[23] Sharifi M and Parvazian A 2015 Stimulated Raman scattering in nonextensive statistics *Phys. Stat. Mech. Its Appl.* **440** 176–84

[24] Seo B H, You S J, Kim J H, Seong D J, Shin Y H and Chang H Y 2013 Measurements of electron energy probability functions in helicon discharge by laser Thomson scattering *Thin Solid Films* **547** 52–6

[25] Wang X-D, Cui Z-X, Zhang H-J, Zheng X, Chen B and Wang Z-S 2013 A new proof of Mie effect in light scattering *Opt. - Int. J. Light Electron Opt.* **124** 6194–6

[26] Mie G 1908 Beiträge zur Optik tuber Medien, speziell kolloidaler Metallösungen *Ann. Phys.* **330** 377–445

[27] Laven P 2015 *MiePlot*

[28] Sauerbrey G 1959 Verwendung von Schwingquarzen zur Wägung dünner Schichten und zur Mikrowägung *Z. Für Phys.* **155** 206–22

[29] Miller J G and Bolef D I 1968 Sensitivity enhancement by the use of acoustic resonators in cw ultrasonic spectroscopy *J. Appl. Phys.* **39** 4589

[30] O'Regan B and Grätzel M 1991 A low-cost, high-efficiency solar cell based on dye-sensitized colloidal TiO_2 films *Nature* **353** 737–40

[31] Luque A, Hegedus S, Hara K and Arakawa H 2003 *Dye-Sensitized Solar Cells, in Handbook of Photovoltaic Science and Engineering (eds A. Luque and S. Hegedus)* (Chichester, UK: John Wiley & Sons, Ltd)

[32] Kudrna P 1997 *Sondová diagnostika nízkoteplotního plazmatu* doctoral thesis (Prague: Charles University in Prague)

[33] Kyuma K, Tai S, Sawada T and Nunoshita M 1982 Fiber-optic instrument for temperature measurement *Microw. Theory Tech. IEEE Trans. On* **30** 522–5

[34] Swihart M T 2003 Vapor-phase synthesis of nanoparticles *Curr. Opin. Colloid Interface Sci.* **8** 127–33

[35] Hosokawa M, Nogi K, Naito M and Yokoyama T 2007 *Nanoparticle Technology Handbook* (Amsterdam: Elsevier)

[36] Ostrikov K and Murphy A B 2007 Plasma-aided nanofabrication: where is the cutting edge? *J. Phys. Appl. Phys.* **40** 2223–41

[37] Ito Y, Sakai O and Tachibana K 2010 Study of plasma enhanced chemical vapor deposition of ZnO films by non-thermal plasma jet at atmospheric pressure *Thin Solid Films* **518** 3513–6

[38] Shimizu Y, Bose A C, Mariotti D, Sasaki T, Kirihara K, Suzuki T, Terashima K and Koshizaki N 2006 Reactive evaporation of metal wire and microdeposition of metal oxide using atmospheric pressure reactive microplasma jet *Jpn. J. Appl. Phys.* **45** 8228

[39] Sakuma H, Aoshima H and Ishii K 2006 Size-controlled Growth of Fe Nanoparticles in Gas Flow Sputtering Process *J. Magn.* **11** 103–7

[40] Sia P Z, Jiang W, Wang H X, Li Z F, Liu J J, Lee J G and Choi C J 2012 Large Scale Synthesis of Nitrogen Doped TiO_2 Nanoparticles by Reactive Plasma *Mater. Lett.* **68** 161–3

[41] Alexandrescu R, Morjan I, Dumitrache F, Scarisoreanu M, Fleaca C T, Morjan I P, Barbut A D, Birjega R and Prodan G 2013 Development of TiO_2 and

TiO_2/Fe-based polymeric nanocomposites by single-step laser pyrolysis *Appl. Surf. Sci.* **278** 305–12

[42] Ayati A, Ahmadpour A, Bamoharram F F, Tanhaei B, Mänttäri M and Sillanpää M 2014 A review on catalytic applications of Au/TiO_2 nanoparticles in the removal of water pollutant *Chemosphere* **107** 163–74

[43] Hossaini H, Moussavi G and Farrokhi M 2014 The investigation of the LED-activated FeFNS-TiO_2 nanocatalyst for photocatalytic degradation and mineralization of organophosphate pesticides in water *Water Res.* **59** 130–44

[44] Gupta S M and Tripathi M 2011 A review of TiO_2 nanoparticles *Chin. Sci. Bull.* **56** 1639–57

[45] Yu J, Low J, Xiao W, Zhou P and Jaroniec M 2014 Enhanced photocatalytic CO_2-reduction activity of anatase TiO_2 by coexposed {001} and {101} facets *J. Am. Chem. Soc.* **136** 8839–42

[46] Baránková H and Bárdos L 2013 Optimization and performance of atmospheric Fused Hollow Cathodes *Vacuum* **87** 128–31

[47] Klusoň J, Kudrna P, Kolpaková A, Picková I, Hubička Z and Tichý M 2013 Experimental study of the discharge in the low pressure plasma jet sputtering system *Contrib. Plasma Phys.* **53** 10–5

[48] Klusoň J, Kudrna P and Tichý M 2013 Measurement of the plasma and neutral gas flow velocities in a low-pressure hollow-cathode plasma jet sputtering system *Plasma Sources Sci. Technol.* **22** 15–20

[49] de Araújo F O, de Almeida E O, Alves C, da Costa J A P and Dumelow T 2006 Deposition of TiO_2 on silicon by sputtering in hollow cathode *Surf. Coat. Technol.* **201** 2990–3

[50] Klusoň J 2013 *Impulsní plazmatické systémy* (Praha: Univerzita Karlova v Praze)

[51] Leshkov S, Kudrna P, Chichina M, Klusoň J, Picková I, Virostko P, Hubička Z and Tichý M 2010 Spatial distribution of plasma parameters in DC-energized hollow cathode plasma jet *Contrib. Plasma Phys.* **50** 878–85

[52] Holden N E 1993 "Table of the Isotopes" in Lide D R ,Ed. *CRC Handbook of Chemistry and Physics* (Boca Raton Fl: CRC Press)

[53] Bárdoš L, Štěpánek I and Karwasz G 1990 Neutral gas flow velocity profiles in the jet plasma-chemical reactor *Vacuum* **40** 449–52

[54] Gemelli E and Camargo N H A 2007 Oxidation kinetics of commercially pure titanium *Matér. Rio Jan.* **12** 525–31

[55] Šícha M, Hubička Z, Tichỳ M, Novák M, Soukup L, Jastrabik L, Behnke J F, Kapička V, Kapoun K and Šerỳ M 1996 The Interaction of the Supersonic Plasma-Jet with the Substrate in the RF Plasma-Chemical Reactor *Contrib. Plasma Phys.* **36** 605–11

[56] Friedlander S K, Windeler R S and Weber A P 1994 Ultrafine particle formation by aerosol processes in turbulent jets: mechanisms and scale-up *NanoStmctured Mater.* **4** 521–8

[57] Miszczak S and Pietrzyk B 2015 Anatase–rutile transformation of TiO_2 sol–gel coatings deposited on different substrates *Ceram. Int.* **41** 7461–5

[58] Hanaor D A H and Sorrell C C 2011 Review of the anatase to rutile phase transformation *J. Mater. Sci.* **46** 855–74

[59] Smirnov B M 2000 *Clusters and Small Particles : In Gases and Plasmas* (New York: Springer)

[60] Devore J R 1951 Refractive Indices of Rutile and Sphalerite *J. Opt. Soc. Am.* **41** 416–7

[61] Lee J-B, Seo S-H and Chang H-Y 2010 Time evolution of electronegativity in a pulsed inductively coupled oxygen plasma *Thin Solid Films* **518** 6573–7

[62] Lee C 1995 Global model of Ar, O_2, Cl_2, and Ar/O_2 high-density plasma discharges *J. Vac. Sci. Technol. Vac. Surf. Films* **13** 368

[63] Polk J E and Capece A M 2015 Materials characterization of impregnated W and W–Ir cathodes after oxygen poisoning *Appl. Surf. Sci.* **338** 27–34

[64] Kang S H, Kang M-S, Kim H-S, Kim J-Y, Chung Y-H, Smyrl W H and Sung Y-E 2008 Columnar rutile TiO_2 based dye-sensitized solar cells by radio-frequency magnetron sputtering *J. Power Sources* **184** 331–5

[65] Praburam G and Goree J 1996 A scattering ratio method for sizing particulates in a plasma *Plasma Sources Sci. Technol.* **5** 84

[66] Dorofeev G A, Streletskii A N, Povstugar I V, Protasov A V and Elsukov E P 2012 Determination of nanoparticle sizes by X-ray diffraction *Colloid J.* **74** 675–85

[67] Kim K H, Utashiro K, Jin Z, Abe Y and Kawamura M 2013 Dye-Sensitized Solar Cells with Sol-Gel Solution Processed Ga-Doped ZnO Passivation Layer *Int J Electrochem Sci* **8** 5183–90

[68] Que L, Lan Z, Wu W, Wu J, Lin J and Huang M 2014 High-efficiency dye-sensitized solar cells based on ultra-long single crystalline titanium dioxide nanowires *J. Power Sources* **266** 440–7

[69] Ludin N A, Al-Alwani Mahmoud A M, Bakar Mohamad A, Kadhum A A H, Sopian K and Abdul Karim N S 2014 Review on the development of natural dye photosensitizer for dye-sensitized solar cells *Renew. Sustain. Energy Rev.* **31** 386–96

[70] Mary Rosana N T, Joshua Amarnath D, Vincent Joseph K L, Suresh A, Anandan S and Saritha G 2014 Natural sensitizers for dye sensitized solar cell applications *Int. J. Sci. Eng. Res.* **5**

[71] Abdou E M, Hafez H S, Bakir E and Abdel-Mottaleb M S A 2013 Photostability of low cost dye-sensitized solar cells based on natural and synthetic dyes *Spectrochim. Acta. A. Mol. Biomol. Spectrosc.* **115** 202–7

[72] Alhamed M, Issa A S and Doubal A W 2012 Studying of natural dyes properties as photo-sensitizer for dye sensitized solar cells (DSSC) *J. Electron Devices* **16** 1370–83

[73] Shooto D N and Dikio E D 2011 Morphological characterization of soot from the combustion of candle wax *Int J Electrochem Sci* **6** 1269–76

[74] Yun S, Hagfeldt A and Ma T 2014 Pt-free counter electrode for dye-sensitized solar cells with high efficiency *Adv. Mater.* **26** 6210–37

[75] Shalini S, Balasundara prabhu R, Prasanna S, Mallick T K and Senthilarasu S 2015 Review on natural dye sensitized solar cells: Operation, materials and methods *Renew. Sustain. Energy Rev.* **51** 1306–25

[76] Huang Y, Dai S, Chen S, Zhang C, Sui Y, Xiao S and Hu L 2009 Theoretical modeling of the series resistance effect on dye-sensitized solar cell performance *Appl. Phys. Lett.* **95** 243503

List of used symbols

d	particle diameter
d_f	density of film
d_n	the length of cathode voltage drop
d_q	density of quartz
E	electric field strength
e	electron charge
f	light frequency
$f(\varepsilon)$	electron energy distribution function (EEDF)
f_c	the resonant frequency of loaded crystal
FF	fill factor
$flow_{Ar}$	argon flow
$flow_{O2}$	oxygen flow
f_q	resonant frequency of unplated crystal
g	the ratio of the mean interparticle potential energy to the mean plasma kinetic energy
H	magnetic field strength
h	vertical distance between the sample/measuring point and the cathode nozzle
I	current
I	intensity of scattered light
$I(d,\theta)$	scattering intensity of nanoparticles with diameter d at the angle θ
I_d	discharge current
I_l	horizontally polarized intensity
I_{pe}	electron flow to the probe
I_{pi}	ion flow to the probe
I_r	vertically polarized intensity
I_{sc}	the short current
J	current density
J_+	ion current density
j_0	normal current density
J_e	electron current density
K	dimensionless shape factor

k_b	Boltzmann constant
L	the characteristic dimension of plasma
L_{sc}	length of solar cell
l_p	Langmuir probe length
l_q	thickness of quartz crystal
m_e	electron charge and mass
n	particle density
n	refractive index
$n(d)$	concentration of nanoparticles with diameter d
n_e	electron density
N_D	electron density in Debye sphere
n_i	ion density
n_o	density of neutral atoms
N_q	the frequency constant for quartz crystal
$\vec{p}$	induced dipole moment
p	pressure
P_{in}	the power input to the cell
P_m	the light power
R	resistance
r_d	Debye radius
R_e	Reynolds number
R_h	energy of the ground state of a hydrogen atom
r_p	probe radius
r_s	probe with electric sheath radius
R_{sh}	shunt resistance of solar cell
R_s	series resistance of solar cell
S_p	probe surface area
T	temperature
T_e	electron temperature
T_f	thin film thickness
T_i	ion temperature
T_o	neutral gas temperature
U	voltage
U_d	discharge voltage

U_{fl} floating potential

U_{oc} the open circuit voltage

U_p probe potential

U_{sp} plasma potential

V particle volume

V_a anode fall

V_{cn} is normal cathode voltage drop

V_k cathode fall

W width of solar cell

α polarizability of the particle

β the line broadening at half the maximum intensity

γ the angle between the scattered dipole moment and the direction of observation

γ_i the ion-electron secondary emission coefficient

δ skin effect thickness

ε electron energy

ε particle permittivity

ε_0 permittivity of the vacuum

η conversion efficiency

θ scattering angle

λ wavelength

λ_D Debye length

μ particle permeability

μ_+ the ion mobility

μ_f shear module of deposited film

μ_q shear module of quartz crystal

$\bar{\upsilon}$ mean electron velocity

υ gas velocity

ν_{en} electron-neutral collision frequency

ν_{pe} plasma frequency

ρ charge density

ρ_g gas density

σ particle conductivity

τ mean size of the ordered (crystalline) domains

φ	electrical potential
ω	angular frequency
ω_{pe}	plasma frequency

Authors' publications

A) Publications in impacted journals:

A1. Perekrestov R, Kudrna P and Tichý M 2015 The deposition of titanium dioxide nanoparticles by means of a hollow cathode plasma jet in dc regime *Plasma Sources Sci. Technol.* **24** 035025

A2. Perekrestov R, Kudrna P, Tichý M, Khalakhan I, Daniš S, Prodan G and Vladoiu R 2016 Crystalline structure and morphology of TiO_2 thin films deposited by means of hollow cathode plasma jet with supporting anode *Surf. Coat. Technol.* **291** 123-129

B) Proceedings in conference books

B1. R. Perekrestov, P. Kudrna, M. Tichý, I. Khalakhan, TiO_2 Nanoparticles Detection by Means of Laser Beam Scattering in Hollow Cathode Plasma Jet, book of abstracts, *32nd ICPIG, July 26-31*, **2015***, Iași, Romania*

B2. Perekrestov, R.; Kudrna, P.; Klusoň, J.; Tichý, M.. Ti/TiO_2 Thin Films Deposition by Means of Hollow Cathode Plasma Jet. In J. Šafránková and J. Pavlů. *WDS'12 Proceedings of Contributed Papers: Part II – Physics of Plasmas and Ionized Media.* : Matfyzpress, **2012**. s. 38–43. ISBN 978-80-7378-225-2

B3. Klusoň, J.; Perekrestov, R.; Kudrna, P.; Tichý, M.. Energy Resolved Ion Mass Spectroscopy of the Pulsed Magnetron Discharge. In J. Šafránková and J. Pavlů. *WDS'12 Proceedings of Contributed Papers: Part II – Physics of Plasmas and Ionized Media.* : Matfyzpress, **2012**. s. 81–86. ISBN 978-80-7378-225-2.

B4. Perekrestov, R.; Kudrna, P.; Tichý, M.. Deposition of TiO_2 Nanoparticles by Means of Hollow Cathode Plasma Jet. In J. Šafránková and J. Pavlů. *WDS'13 Proceedings of Contributed Papers: Part II – Physics of Plasmas and Ionized Media.* : Matfyzpress, **2013**. s. 139–143. ISBN 978-80-7378-251-1.

B5. Perekrestov R., Kudrna P., Tichý M.. Deposition of TiO_2 Nanoparticles by Means of Hollow Cathode Plasma Jet in DC Regime. In J. Šafránková and J. Pavlů. *WDS'14 Proceedings of Contributed Papers — Physics*: Matfyzpress, **2014**. s. 275–279. ISBN 978-80-7378-276-4.

Attachments

1. Perekrestov R, Kudrna P and Tichý M 2015 The deposition of titanium dioxide nanoparticles by means of a hollow cathode plasma jet in dc regime *Plasma Sources Sci. Technol.* **24** 035025
2. Perekrestov R, Kudrna P, Tichý M, Khalakhan I, Daniš S, Prodan G and Vladoiu R 2016 Crystalline structure and morphology of TiO_2 thin films deposited by means of hollow cathode plasma jet with supporting anode *Surf. Coat. Technol.* **291** 123-129

IOP Publishing Plasma Sources Science and Technology

Plasma Sources Sci. Technol. **24** (2015) 035025 (10pp) doi:10.1088/0963-0252/24/3/035025

The deposition of titanium dioxide nanoparticles by means of a hollow cathode plasma jet in dc regime

R Perekrestov, P Kudrna and M Tichý

Charles University in Prague, Faculty of Mathematics and Physics, V Holešovičkách 2, 180 00 Prague 8, Czech Republic

E-mail: mr.perekrestov@gmail.com

Received 10 February 2015, revised 27 April 2015
Accepted for publication 14 May 2015
Published 8 June 2015

Abstract

TiO_2 nanoparticles are being investigated in this work. Nanoparticles were obtained in Ar plasma on monocrystaline Si(111) substrate by means of a gas-phase deposition using a low pressure hollow cathode plasma jet. The material of the cathode is pure titanium. Oxygen was introduced separately from argon through an inlet in the chamber. The nanoparticle growth mechanism is qualitatively discussed. The morphology of the surfaces of thin films was investigated by an atomic force microscope. The chemical composition of the thin films was investigated by means of an energy-dispersive x-ray analysis and x-ray photoelectron spectroscopy. A cylindrical Langmuir probe and a fiber optic thermometer was used for measurements of plasma parameters and neutral gas temperature respectively. The relationship between plasma parameters and the films' morphology is particularly explained.

Keywords: nanoparticles, hollow cathode plasma jet, Langmuir probe, titanium dioxide, fiberoptic thermometer

(Some figures may appear in colour only in the online journal)

1. Introduction

The synthesis of nanoparticles is currently the basis of nanotechnology. Generally particles with a size ranging from 1 to 100 nm are called nanoparticles. The application of nanoparticles is growing rapidly in nanoscale science and engineering. Such properties of nanoparticles as surface to volume ratio, quantum confinement, and surface atom arrangement are of great importance. By controlling the size of nanoparticles in materials we can obtain new properties.

In recent years a number of techniques for nanoparticle synthesis have been developed. The most widespread techniques of gas-phase nanoparticle synthesis using evaporation of solid material are: pulsed laser ablation, spark discharge generation, inert gas condensation and ion sputtering. Gas-phase methods are based on achieving the supersaturation necessary to start the nucleation of nanoparticles [1, 2]. A review on plasma nanofabrication can be found in [3]. In plasma jets have been, e.g. deposited the ZnO [4], WO [5] or Fe films [6].

Because of their photocatalytic properties which can be tested by e.g. dye decomposition [7], TiO_2 nanoparticles have applications in different fields of technology. They are used in biomedical research [8], as well as in environmental applications for the photocatalytic treatment of wastewater [9] and pesticide degradation [10]. Nanoparticles of TiO_2 dissociate the water molecule to produce hydrogen. The TiO_2 is used for dye production in industry [11]. The crystalline structure of TiO_2 has three polymorphs: anatase (tetragonal), rutile (tetragonal), and brookite (orthorhombic). The investigation of anatase photocatalytic activity is of great interest, e.g. for CO_2 reduction [12]. Experiments have shown that using TiO_2 as a photocatalyst in the form of nanoparticles is more effective than bulk material [11]. Nanostructured TiO_2 films have been modified using plasma in [13].

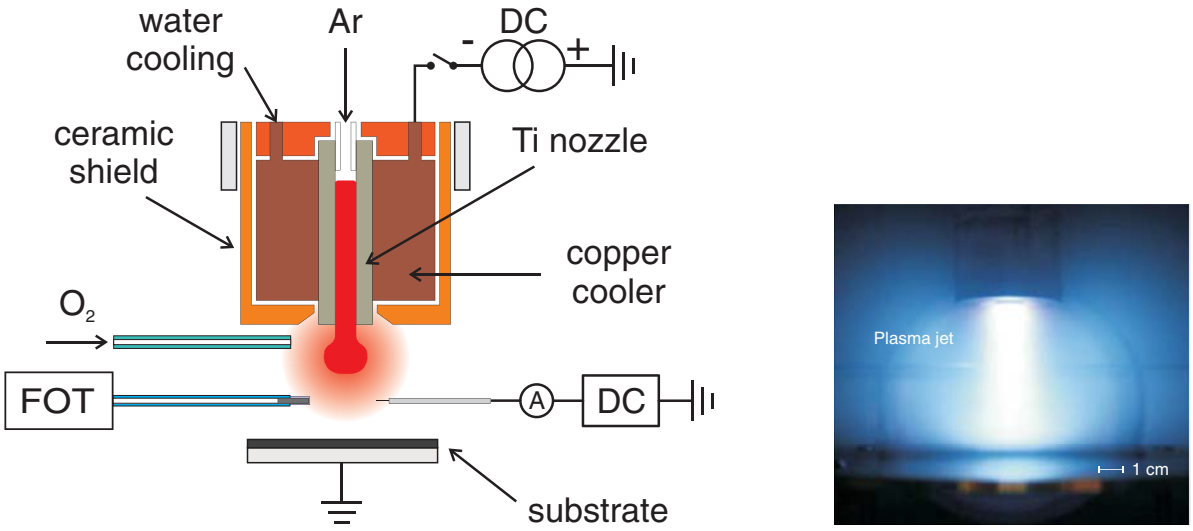

Figure 1. The scheme of the vacuum system for plasma diagnostics and thin film deposition by means of a hollow cathode plasma jet in the dc regime (left) and a photograph of the burning discharge (right). The UHV chamber is not shown.

This article deals with the ion sputtering deposition of TiO_2 nanoparticles by means of a hollow cathode plasma jet (HCPJ). The key part of the HCPJ is the tubular electrode—a nozzle that works as a hollow cathode—through which the working gas, typically argon flows, and which is attached to a power source. The HCPJ utilizes the hollow cathode effects, namely pendulum electrons and the uv-radiation, to create a high density plasma discharge. HCPJ can be utilized in wide range of pressures: from low (0.1 Pa) up to atmospheric pressure [14]. The advantage of *low pressure* HCPJ is the possibility to use the dc discharge, which is more simple with respect to RF. The use of HCPJ for nanoparticle deposition is based on sputtering the material from the inner cathode surface by ions which gain energy from the cathode fall. In comparison with the more commonly used magnetron sputtering it has some significant advantages in the production of nanoparticles. The space inside the hollow cathode with its heightened pressure serves as a space for nanoparticle nucleation. To achieve this with a magnetron an aggregation chamber provided by differential pumping is necessary [15]. Moreover, the velocity of a working buffer gas can be adjusted via its flow rate [16, 17]. This influences the resident time of nanoparticles inside and outside of the hollow cathode and, consequently, influences the size of the nanoparticles deposited on the substrate. The deposition process by means of HCPJ is covered in more detail in [18, 19].

This work describes our investigation of the relationship between the inhomogeneous parameters of the plasma plume generated by HCPJ and the properties of the nanomaterial deposited onto the substrate. Similar conditions were used in [6] for the deposition of Fe nanoparticles. The processes of deposition were partially explained. In our work we studied the distribution of nanoparticles on the substrate and added plasma diagnostics which is important since the nanoparticle growth occurs in the plasma. The stress is focussed on conditions favourable for the formation of nanoparticles before they reach the substrate.

2. Experimental setup

The scheme of HCPJ is shown in figure 1. The hollow cathode is made of titanium and serves as the sputtering target. It has a tubular shape and forms a nozzle through which the working gas flows. The hollow cathode is powered by the negative pole of a dc power supply, the Advanced Energy MDX 500, operating in constant current mode. The upper limits of current and voltage of the power supply are 500 mA and 1200 V respectively. The titanium nozzle is cooled by a water flow via the copper blocks surrounding it. The outer surface of the nozzle is isolated from the discharge volume by a cylindrical shield made of a Lava ceramic that prevents the burning of the discharge in any other part of the nozzle except the hollow cathode. The ultra high vacuum chamber is pumped by a turbo-molecular pump down to the ultimate pressure of 10^{-5} Pa. Argon with a purity of 99.999% serves as a working gas. We use a load lock for the manipulation with samples. It consists of a small vacuum chamber connected to the main system via two gate valves and is equipped with a the moveable feedthrough with a fork at the end which grips the substrate holder and sets the position of the substrate.

The process of TiO_2 deposition by HCPJ is governed by several macroparameters. Among the most important are discharge power, pressure, working gas flow rate, and the cathode to substrate separation. Each of these influences the physical quantities that are important for the properties of the deposited material: the degree of ionization, the gas temperature, plasma flow dynamics, etc. An important advantage of our HCPJ system is its ability to vary the distance between the hollow cathode as a source of nanoparticles and the substrate without the necessity of breaking vacuum conditions. In this work we concentrated on the effects of the discharge current and argon flow rate. The other experimental conditions we tried to keep constant in order to reveal the more apparent dependencies on the two selected parameters.

A tungsten cylindrical Langmuir probe is used for plasma diagnostics. The diameter of the probe is $2r_p = 50$ μm and the length $l_p = 2.2$ mm. A step motor with a linear vacuum feedthrough is used for the change of the radial probe position. Measurements with a Langmuir probe were provided by a multimeter Siemens B 3220 and a voltage calibrator Siemens B 3050. A fiberoptic thermometer Optocon FOtemp1 was used for measuring the neutral gas temperature; this principle is described in [20, 21]. It consists of a GaAs probe on the tip of the optical fiber connected to the small spectrometer and a source of light. The principle of this device is based on the shift of probe band gap edge with a change in its temperature. According to the spectrometer data this shift is about 0.4 nm K^{-1}. The device's temperature range is from −200 up to 300 ℃ with the accuracy of ±0.5 ° C. The upper limit is given by the fiber and tip plastic jacket.

The thin films were analyzed by an atomic force microscope (AFM) NT-MDT Ntegra Prima with Multi75-DLC cantilevers in semi-contact mode, by a scanning electron microscope (SEM) Tescan Mira 1 LMH with energy-dispersive x-ray analysis (EDX) detector Bruker AXS, and by x-ray photoelectron spectroscopy (XPS) Specs Phobios 100 with Al Kα x-ray source at the incidence angle of 45°.

3. Results

We deposited several samples under different discharge currents and argon flow rates on a monocrystalline silicon (111) substrate in order to investigate how these parameters influence the thin film surface morphology.

Our original idea was to use a passive $TiO_2/Ti_2O_3/TiO$ layer on the top of the cathode as the main source of oxygen which appears after each exposure of the cathode to the atmosphere, or after introducing oxygen together with argon into the HCPJ nozzle [22]. This method, however, has many disadvantages: restriction in thickness, a high degree of impurities, chemical inhomogeneity, and difficult reproducibility. If we introduced oxygen directly to the hollow cathode together with the argon flow the discharge became very unstable because of intensive cathode surface oxidation. To avoid those problems we introduced the oxygen separately from argon into the main discharge chamber in the amount of 0.5 sccm, see figure 1.

Relatively high pressure (100 Pa) was used to create favorable conditions for cluster synthesis. Samples were deposited at 40 mm cathode-to-substrate separation. While conventional systems for the synthesis of nanoparticles use separate pumping of aggregation and deposition chambers [15] we made use of a pressure gradient between the hollow cathode's inner volume and the vacuum chamber. Thus, the hollow cathode acts as an aggregation chamber because of the heightened pressure inside it. Examination of the inner surface of a hollow cathode that had been in use for approximately one year revealed that sputtering was not uniform and that there was a region close to the nozzle exit where erosion had reached its maximum. The position of this region was flow dependent and had a tendency to migrate along the inner surface of the hollow cathode. This migration is evident from those rare cases when discharge accidentally changes its shape and voltage. The working gas flow rate directly influences plasma dynamics. With an increase in the argon flow rate the plasma plume becomes longer and obtains a well-defined columnar shape.

3.1. Thin films diagnostics

AFM scans of the samples' surfaces deposited under different experimental conditions are given in figure 2. The scans were performed approximately in the sample center. From vertical scales it is possible to observe that the roughness of the film is gradually increasing with the argon flow rate. The samples deposited under a working gas flow rate of 100 sccm, see figures 2(a) and (d), are out of the plasma region; therefore, the plasma's influence is almost negligible and the temperature of the substrate surface remains at a relatively low value (from 50 up to 130 ℃). Measurements of the neutral gas temperature are described in more detail in section 3.3. On the other hand, samples deposited under argon flow rates 200 sccm and higher were in direct contact with the plasma. Under these conditions nanoparticles have a tendency to form bigger agglomerates.

In a first approximation nanoparticles have a spherical shape. Using this assumption we measured particle diameters. We used approximately 70–100 randomly chosen nanoparticles from each scan and complemented figure 2 with corresponding histograms.

The dependencies of mean nanoparticle size and root mean square roughness (RMSR) on discharge current and argon flow rate are given in figure 3. Nanoparticle sizes vary in the range of from 10 nm up to 20 nm. From figure 3(a) it is possible to observe an evident decrease in the mean nanoparticle size with the growth of the discharge current. At the same time, the argon flow rate has almost no influence on the nanoparticle size. The RMSR of the nanoparticle layers gradually increases with the growth of both parameters.

The surface distribution of nanoparticles becomes inhomogeneous under the high values of discharge currents and working gas flow rates corresponding to figures 2(b) and (c). Samples deposited under these conditions have a well-defined structure. In the middle of the sample we observed a round mirror-like region. The diameter of the region approximately corresponds to the diameter of the plasma plume (10–12 mm). Around this region is a black matt ring where we observed agglomerate clusters. In a center of the sample agglomerate clusters were not found.

In figure 4 two AFM measurements carried out on the same sample in two positions outside its center are given. These results show that the surface distribution of agglomerate clusters is not uniform and is symmetric with respect to the sample center. The morphology of agglomerate clusters is shown in a high resolution SEM scan in figure 4(b).

The quantitative composition of the thin films carried out by the EDX is shown in the top graphs of figure 5. Relatively thick samples of 3.5 μm exceeding the electron penetration depth of several hundreds of nm were prepared to exclude the influence of a silicon substrate on the EDX measurements. The first sample deposited without oxygen is weakly oxidized

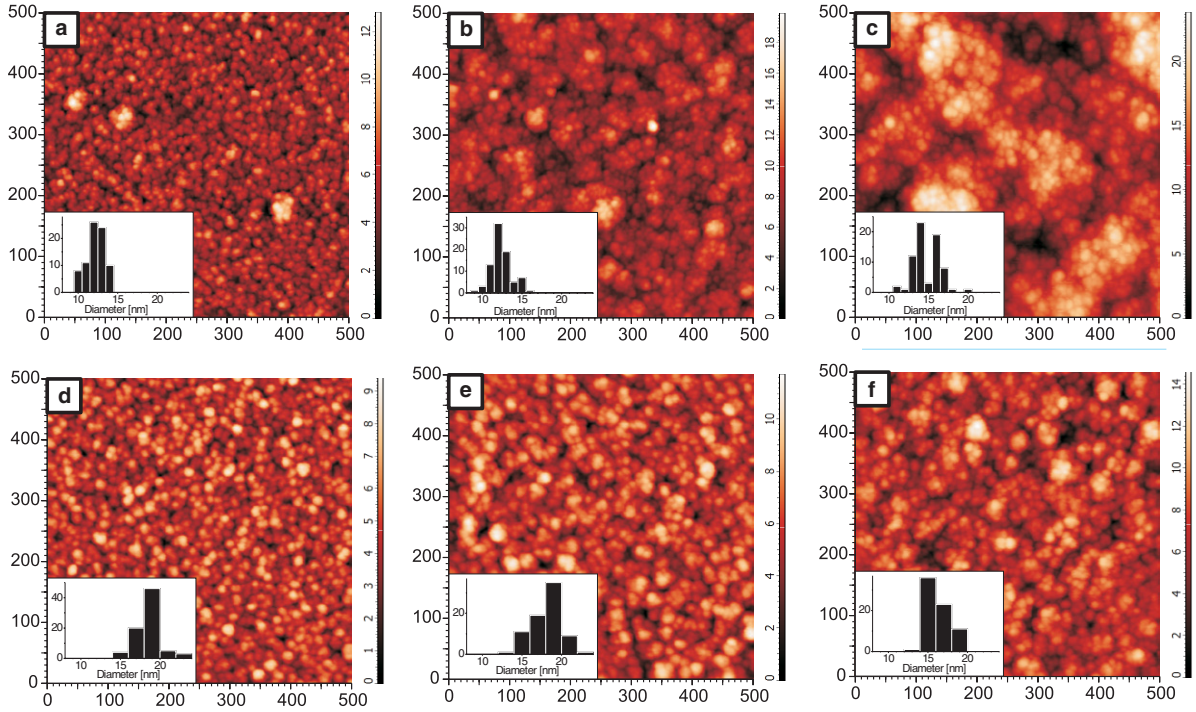

Figure 2. AFM scans of TiO_2 nanoparticle layers under different values of discharge currents and argon flow rates:(a)–(c) $I_d = 400$ mA, $f_{Ar} = 100$, 200, 300 sccm respectively; (d)–(f) $I_d = 100$ mA, $f_{Ar} = 100$, 200, 300 sccm respectively. Dimensions on the scales are given in nanometers.

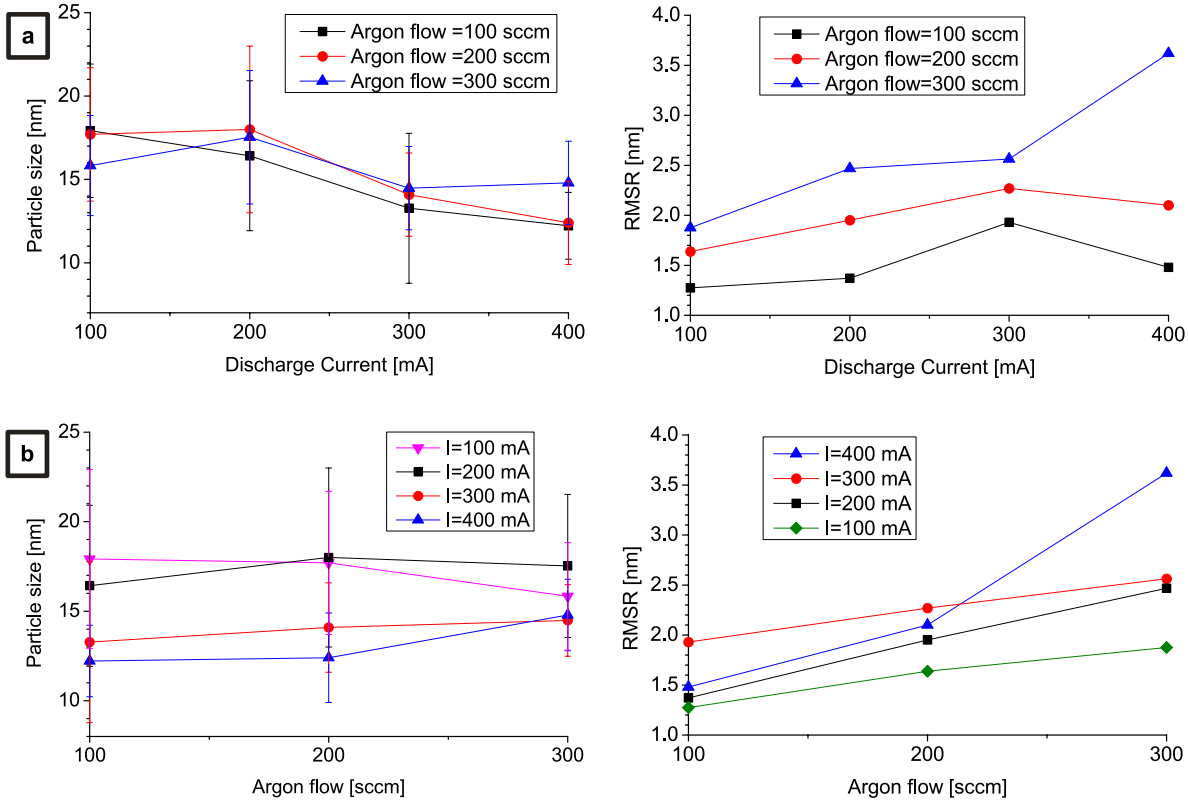

Figure 3. Dependences of the average nanoparticle size (left) and root mean square roughness (right) on: (a) discharge current, (b) argon flow rate. The error bars denote the whole span of the particle diameters identified on the sample.

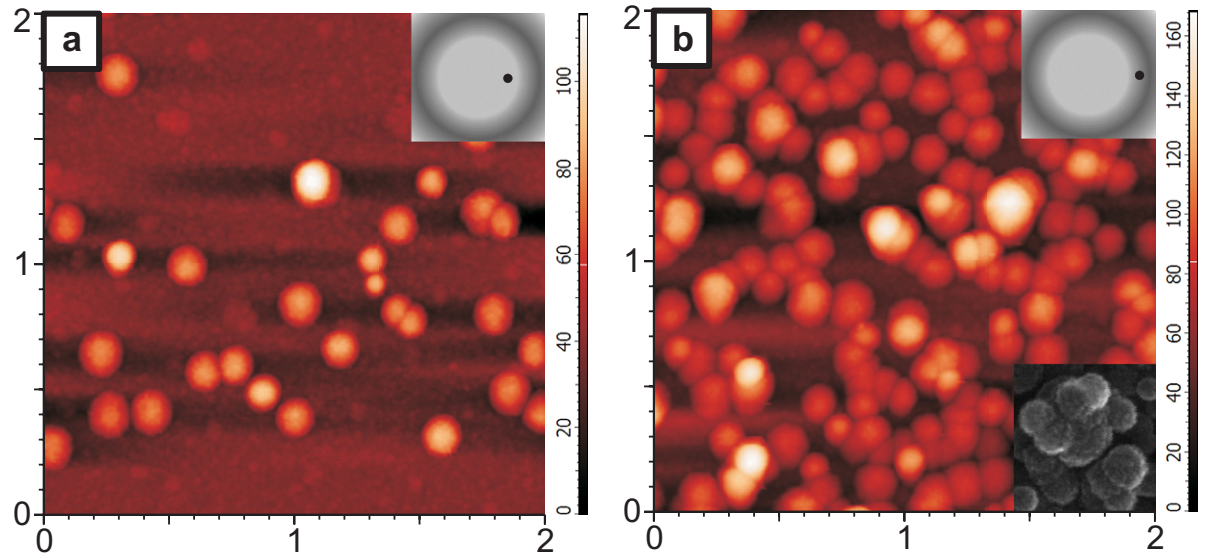

Figure 4. AFM scans of the sample deposited under $I_d = 520$ mA and $f_{Ar} = 300$ sccm (a) at 5 mm from the sample center, (b) at 7 mm from the sample center. The positions of the scans are indicated in pictures located in the top right-hand corner. The higher resolution SEM scan in (b) shows the morphology of particles. Area dimensions are given in micrometers, color height scale in nm.

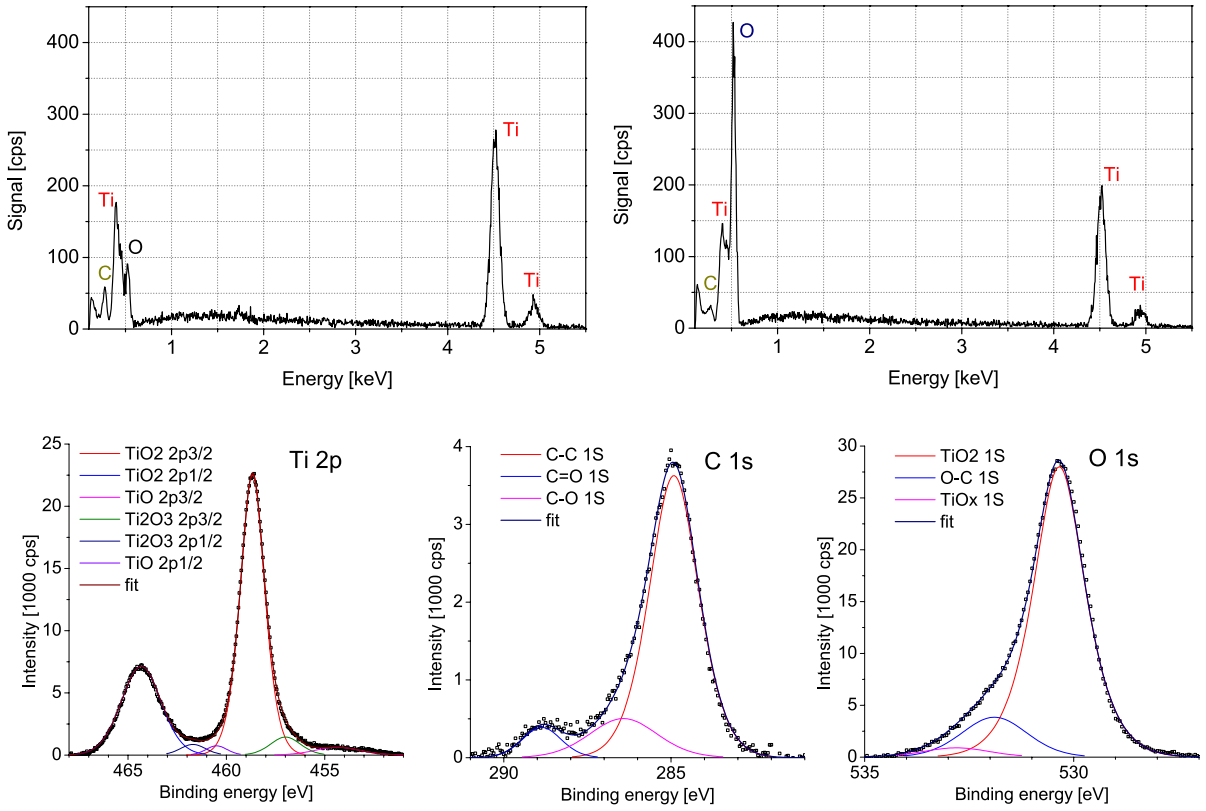

Figure 5. EDX patterns of thick TiO_2 nanoparticle layers without (top left) and with oxygen flow of 0.5 sccm (top right). XPS spectra of Ti 2p, C 1s and O 1s peaks of the layer deposited without oxygen (bottom). The deposition lasted 20 min at a discharge current of 520 mA, pressure 140 Pa, and argon flow rate 400 sccm.

(O 28%, Ti 62%). This is caused when the sample is exposed to the atmosphere during transport to the EDX. The atmospheric oxygen creates an amorphous oxidized layer on the top which resists further oxidation. The depth of oxidation is usually 5–10 nm [22]. In our case, the oxidized layer can be thicker because of the developed morphology of the film surface. The second sample shows the composition of O (63%) and Ti (32%), which approximately corresponds to a the titanium dioxide chemical formula. In both samples we also found a small amount (4%) of carbon impurities. The bottom three graphs of figure 5 show an XPS analysis of the sample deposited without oxygen. The analysis of the C 1s photoelectron

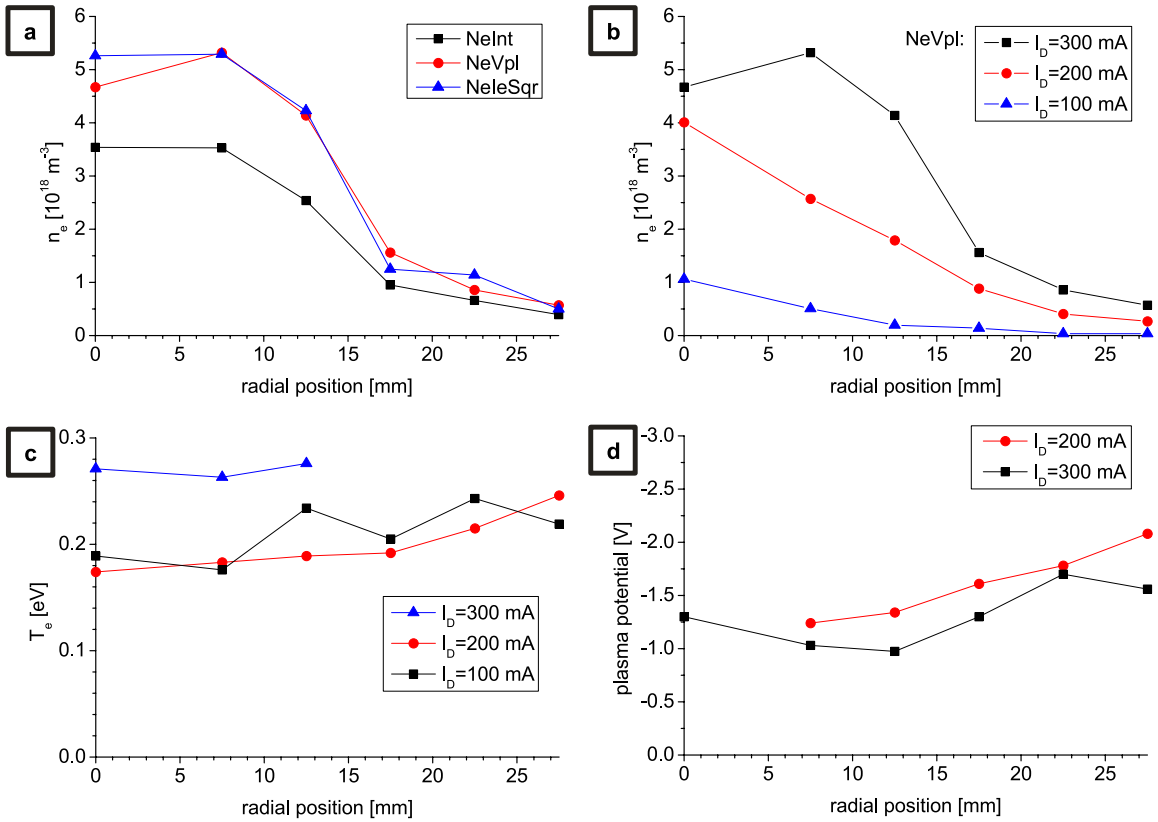

Figure 6. Dependences of electron density, electron temperature and plasma potential on the distance between probe and discharge axis at a vertical position $h = 42$ mm below the cathode outlet. The electron density (a) calculated by three different methods at $I_d = 300$ mA and (b) NeVpl for different values of discharge current. Dependence of electron temperature (c) and plasma potential (d) on the probe radial position. The values of pressure and argon flow rate were 100 Pa and 200 sccm, respectively.

peak shows that the carbon is not chemically bonded with the titanium. Since the experimental system is UHV clean, the carbon is most probably caused by exposure of the sample to the atmosphere after deposition. Titanium 2p spectrum consists of two major peaks because of spin–orbit splitting. These two peaks correspond to TiO_2. The peaks of other titanium oxides such as TiO or Ti_2O_3 are present but are small with respect to TiO_2. The XPS spectrum of the film deposited with the introduction of oxygen shows similar results. We can conclude that a comparatively low oxygen flow rate (0.5 sccm) is sufficient for the complete oxidation of titanium.

3.2. Plasma diagnostics

When the formation of nanoparticles occurs in a gas phase, information about plasma is of great importance. We focused on the Langmuir probe measurement of the electron temperature T_e and electron density n_e at the approximate position where the sample is located during the deposition. Experimental conditions were chosen to be similar to those applied for the deposition. The aim of these measurements was to evaluate the influence of the plasma plume on the deposition since the samples were in contact with plasma. There are several ways of evaluating these two parameters from the probe current-voltage characteristics [23]. We assumed that energy distribution function is Maxwellian-like:

$$f_{\mathrm{Max}}(eV) \propto \sqrt{eV}\exp\frac{-e(V-V_{pl})}{k_{\mathrm{B}}T_e} \tag{1}$$

$$\frac{\mathrm{d}^2 I_p(V)}{\mathrm{d}V^2} = \frac{e^3 n_e S}{4}\sqrt{\frac{2}{m_e}}\sqrt{\frac{1}{eV}} f_{\mathrm{Max}}(eV)\,. \tag{2}$$

In equations (1) and (2) the symbols have their usual meaning. The electron temperature T_e was estimated from the slope of the second derivative of probe characteristics in a semilog scale. The electron density was estimated (i) from the integral of the second derivative of current-voltage characteristics equation (2) (denoted as NeInt in figure 6), (ii) from the electron current at the plasma potential $I(V_{pl})$ (NeVpl) and (iii) from the slope of the plot $I_e^2(V)$ (NeIeSqr). The electron current at the plasma potential is given by

$$I_p(V_{pl}) = \frac{1}{4} n_e v_a e_0 A_p, \tag{3}$$

where $v_a = [(8k_{\mathrm{B}}T_e)/(\pi m_e)]^{\frac{1}{2}}$. From equation (3) the electron density can be calculated. Furthermore, the n_e can be estimated from the slope of the plot of the square of the electron current $I_e^2(V)$ versus the probe voltage

$$I_e^2(V) = \frac{2e^3 A_p n_e^2}{\pi^2 m_e}\cdot V + \mathrm{const.} \tag{4}$$

We used all of these methods in order to assess the error of the electron density measurement. Measurements were taken in proximity to the vertical position where the substrate was placed during depositions. The dependencies of electron density on the radial position of the probe are shown in figures 6(a) and (b). A comparison of the results obtained by means of the three different methods are presented in figure 6(a). The method based on an integration of the second derivative of current-voltage characteristics shows, as expected, somewhat lower values of plasma density because of the error in the second derivative caused by the numerical differentiation near the V_{pl}.

The third approach based on the electron current square works under the assumption of the thick sheath which can be approximated by several Debye lengths $\lambda_D = [(\varepsilon_0 k_B T_e)/(e^2 n_e)]^{\frac{1}{2}}$. Closer to the axis, i.e. at higher plasma densities the λ_D becomes smaller, which is associated with higher error. Nevertheless, it is seen from figure 6(a) that the $I_e^2(V)$ method agrees well with the $I(V_{pl})$ method. In figure 6(b) we show the dependencies of electron density on the radial position of the probe measured under different discharge currents. Here, the n_e is calculated from $I_e(V_{pl})$. It is evident, especially from the dependence that corresponds to discharge current 300 mA, that plasma has a well-defined border approximately at a distance of 15 mm from the discharge axis. Outside of this border the ionization level falls dramatically. The electron temperature and plasma potential stay almost independent on the radial probe position. The values of the electron temperature for the discharge currents 100, 200, 300 mA are 0.27, 0.21, 0.2 eV, respectively. The low electron temperature is typical for this discharge type because almost the whole cathode fall is located inside or in the vicinity of the cathode. These values are in agreement with [16] and [24], but in the second reference much higher oxygen to argon ratios were used. The plasma potential is slightly negative when the probe is used in pure argon as in [16, 24]. The negative value of the plasma potential can be explained by the low radial diffusion to the chamber walls at the working pressure of 100 Pa and the low electron temperature. This leads to the confinement of the discharge channel that carries the discharge current mostly to the substrate holder, causing the role of chamber walls as the anode to be nearly unimportant. The measurements were performed without oxygen flow. Even the smallest oxygen flow rate (0.1 sccm) causes a rapid oxidation of the tungsten Langmuir probe surface, after which the probe loses its conductivity and its further use becomes impossible until it is cleaned by an electron bombardment in pure argon.

3.3. Neutral gas temperature measurements

In the measurements of the neutral gas temperature we tried to cover a wide range of argon flow rates so as to obtain a complex of information about the temperature in proximity to the substrate. As mentioned in section 2 the fiberoptic thermometer Optocon FOtemp1 was used for this purpose. However, at some points too close to the plasma plume axis under the high values of a working gas flow rate it was not possible to measure because of the thermometer's upper limit (300 °C). The results of these neutral gas temperature measurements are presented in figure 7. In the case when the argon flow rate is relatively low (i.e. plasma does not touch the substrate) the dependence of the neutral gas temperature on the probe radial position is flat even at high discharge currents. Increasing the flow rate leads to an inhomogeneous distribution of the temperature with a maximum at the axis of the plasma column. On the other hand, we observed the presence of agglomerate clusters under high values of the argon flow rate. According to the aforementioned AFM results these clusters are concentrated mostly at the periphery of the sample, where the temperature is significantly lower than in the middle. We assume that this can explain the abundance of agglomerate clusters at the periphery of the sample since at lower temperatures the tendency of agglomerate clusters to reform into bigger clusters is lower. The surface morphology of the deposited layers is treated in more detail in the Discussion section.

Dependencies of the neutral gas temperature on the discharge current at the plasma axis are given in figure 7(a). The temperature distribution of the neutral gas is strongly flow dependent. We can see in figures 7(b)–(d) a similar strong flow dependence. In these dependencies some points were not measured because of the temperature limit. However, extrapolation of the dependence that corresponds to an argon flow rate of 300 sccm shows that the temperature can easily exceed 300 °C at discharge currents of 300 mA.

4. Discussion

From the AFM scans presented in figures 2 and 4 it is possible to observe how basic mechanisms of nanoparticle growth in a gas phase show themselves under different conditions of deposition. Among these, we distinguish two of the most important: *coagulation* and *single atom attachment* [25–27]. The process of single atom attachment is present in both cases, while the coagulation of nanoparticles into agglomerates appears at higher values of discharge current and working gas flow rate. The mean nanoparticle size at discharge current 100 mA is bigger than at 400 mA. The first explanation is a higher neutral gas temperature and ionization of the plasma plume at a discharge current of 400 mA. The low electron temperature in the proximity of the substrate indicates that plasma is only slightly anisothermic in this region and affects only nanoparticle charges. Their floating potential is low and therefore the electric drift of nanoparticles is negligible. On the other hand, the ion energy inside of the hollow cathode is much higher and can reach 300 eV if the ions receive the full energy of the cathode fall. The sputtered titanium atoms gain a part of the energy of the positive ions which is high to create a chemical bond between them. We assume that the nucleation process under higher discharge currents and consequently, the residence time of particles in plasma is shorter. It can result in higher amount of nucleation centers at the expense of the particle size before reaching the substrate. In our case the cathode to substrate separation is 3.5 cm only. Thus, the dependence of particle size on the working gas flow rate is different in comparison with [6]. We explain that by a higher gas temperature

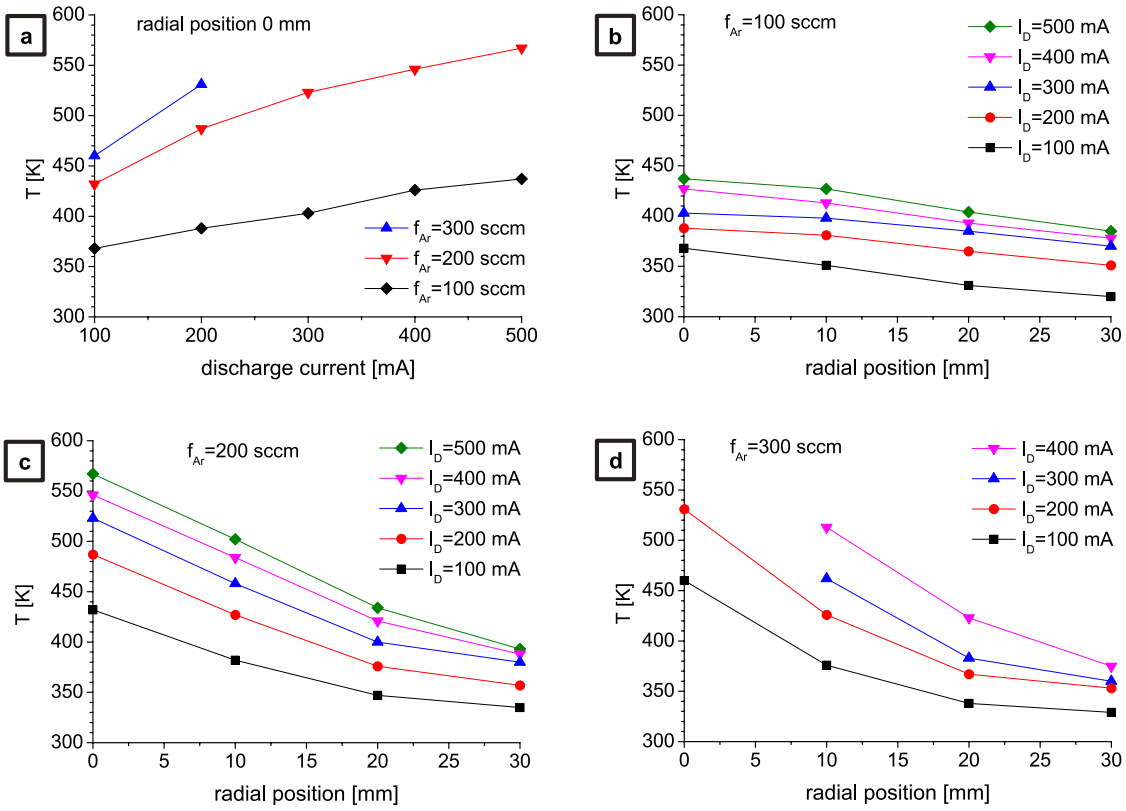

Figure 7. Measurements of neutral gas temperature at a constant pressure of 100 Pa, oxygen flow 0.5 sccm and vertical position $h = 42$ mm below the cathode outlet. Dependence on the discharge current and argon flow rate at the plasma axis (a). Dependences on the radial position and discharge current for the three different values of argon flow (b)–(d).

and higher ionization of the plasma plume at a discharge current of 400 mA. We expect that the ion energy inside the hollow cathode can reach a comparatively high value (hundreds eV). The sputtered titanium atoms can gain part of the energy of the positive ions by collision (the pressure in the hollow cathode is higher than in the discharge chamber). As a result, the energy of the sputtered Ti atoms is too high to create a chemical bond (to nucleate). However, after leaving the hollow cathode the Ti neutrals lose their energy and further downstream can nucleate.

We assume therefore, that the nucleation process under higher discharge currents and consequently higher temperatures of gas starts further downstream (closer to the substrate). Hence, the residence time of particles in plasma is shorter and the mean nanoparticle size is smaller. In addition, the high concentration of sputtered Ti atoms at the moment when nucleation starts caused by higher discharge current can result in higher amounts of nucleation centers at the expense of the particle size. This result seems to apparently contradict the results presented in [6], where a slight increase in the mean nanoparticle size with increasing the discharge current was found. However, this difference can be explained by the substantially greater distance of the substrate from the hollow cathode in [6] (17 cm) compared to ours (4 cm) and the consequently higher residence time before reaching the substrate.

In [6] there was also observed the increase in the mean nanoparticle size with the decrease in the working gas flow rate. The authors in [6] explained this effect by the increase in the residence time of the nanoparticles before reaching the substrate. We did not observe the significant dependence of the mean nanoparticle size with the working gas flow rate, as seen in figure 3(b). Since we have a shorter distance between the hollow cathode and the substrate, we believe that the mean nanoparticle size is influenced by two competing effects: (i) the shorter residence time at a higher gas flow rate leading to the creation of smaller nanoparticles and (ii) better Ti atoms thermalization at higher gas flow rates that is beneficial for creating larger nanoparticles. As follows from experiment, at a distance of 4 cm between the hollow cathode and the substrate used in our experiment, these two effects apparently cancel each other out. We assume that the thermalization of vaporized titanium is slower in the case of a higher discharge current. The thermalisation of sputtered titamium is a necessary condition for the beginning of the nucleation of a nanoparticle.

Agglomerates of nanoparticles have a grain-like surface morphology, as shown in figure 4(b). Hence, the process of coagulation in the gas phase occurs when nanoparticles are already in a solid state. The inhomogeneous distribution of agglomerates on the sample is mainly caused by the increase in the working gas flow rate. A high working gas flow rate is connected with the higher pressure and a higher flow velocity inside the hollow cathode. This reduces both the radial diffusion of the sputtered titanium atoms to the axis of the flow,

and the time during which particles growing near the axis reach the substrate. This results in a high concentration of titanium atoms near the cathode wall, which leads to a higher concentration of nanoparticles in the outer layer of the plasma plume, and subsequently to a significant number of collisions between the nanoparticles in this outer layer. In addition, clusters can be mechanically moved from the sample center to its periphery by the impinging argon flow. This effect has been studied and visualized in [28]. Since the calculated Reynolds number for the flow velocity 300 m s^{-1}, argon temperature of 400 K, and stream diameter of 20 mm is about 370, turbulences and therefore turbulent agglomeration [29] may start to occur. The amount of the agglomerate particles is small at discharge currents lower than 300 mA since the sputtering rate is low. This confirms that agglomerate particles can be deposited only at a high working gas flow rate in conjunction with a high discharge current.

5. Conclusions

TiO_2 nanoparticles have found applications in various areas of industry and science. HCPJ gives us an opportunity to obtain nanoparticles from the gas phase and gives us control over the process of their creation. By varying plasma parameters such as the discharge current and working gas flow rate, it is possible to affect the size of nanoparticles and the roughness of the thin film. Under high values of discharge current and a working gas flow rate, nanoparticles have a tendency to agglomerate in clusters (their diameter is more than 100 nm). This transition occurs approximately under an argon flow rate of 200 sccm and a discharge current of 400 mA. The Langmuir probe and fiberoptic thermometer give us complex information about the properties of the plasma plume during deposition. The plasma potential and electron energy were almost constant over the substrate dimensions. At the same, time we observed a high inhomogeneity of electron density under high values of the argon flow rate and discharge current. The effect of ion bombardment of the sample is negligible because of the low ion energy at the sample position. Of more significance can be the influence of charged nanoparticles, especially in a region with high plasma density. In the future we also plan to investigate the HCPJ with an RF and dc pulsed power supply.

Acknowledgments

The partial financial support by the Czech Science Foundation, grant No. 15-00863S and by Charles University Grant Agency, grant No. 604612 is gratefully acknowledged.

References

[1] Märk T S 2003 Vapor-phase synthesis of nanoparticles *Curr. Opin. Colloid Interface Sci.* **8** 127–33
[2] Hosokawa M, Nogi K, Naito M and Yokoyama T 2007 *Nanoparticle Technology Handbook* (Amsterdam: Elsevier)
[3] Ostrikov K and Murphy A B 2010 Plasma-aided nanofabrication: where is the cutting edge? *J. Phys. D: Appl. Phys.* **40** 2223–41
[4] Ito Y, Sakai O and Tachibana K 2010 Study of plasma enhanced chemical vapor deposition of ZnO films by non-thermal plasma jet at atmospheric pressure *Thin Solid Films* **518** 3513–6
[5] Shimizu Y, Bose A C, Mariotti D, Sasaki T, Kirihara K, Suzuki T, Terashima K and Koshizaki N 2006 Reactive evaporation of metal wire, microdeposition of metal oxide using atmospheric pressure reactive microplasma jet *Japan. J. Appl. Phys.* **45** 8228–34
[6] Sakuma H, Aoshima H and Ishii K 2006 Size-controlled growth of fe nanoparticles in gas flow sputtering Process *J. Magn.* **11** 103–7
[7] Sia P Z, Jiang W, Wang H X, Li Z F, Liu J J, Lee J G and Choi C J 2012 Large scale synthesis of nitrogen doped TiO_2 nanoparticles by reactive plasma *Mater. Lett.* **68** 161–3
[8] Alexandrescu R, Morjan I, Dumitrache F, Scarisoreanu M, Fleaca C T, Morjan I P, Barbut A D, Birjega R and Prodan G 2013 Developmentof TiO_2, TiO_2/Fe-based polymeric nanocomposites by single-step laser pyrolysis *Appl. Surf. Sci.* **278** 305–12
[9] Ayati A, Ahmadpour A, Bamoharram F F, Tanhaei B, Mänttäri M and Sillanpää M 2014 A review on catalytic applications of Au/TiO2 nanoparticles in the removal of water pollutant *Chemosphere* **107** 163–74
[10] Hossaini H, Moussavi G and Farrokhi M 2014 The investigation of the LED-activated FeFNS-TiO_2 nanocatalyst for photocatalytic degradation, mineralization of organophosphate pesticides in water *Water Res.* **59** 130–44
[11] Gupta S M and Tripathi M 2011 A review of TiO_2 nanoparticles *Chin. Sci. Bull.* **56** 1639–57
[12] Yu J, Low J, Xiao W, Zhou P and Jaroniec M 2014 Enhanced photocatalytic CO_2 reduction activity of anatase TiO_2 by coexposed 001, 101 facets *J. Am. Phys. Soc.* **136** 8839–42
[13] Kim H J, Kim J and Hong B 2013 Effect of hydrogen plasma treatment on nano-structured TiO_2 films for the enhanced performance of dye-sensitized solar cell *Appl. Surf. Sci.* **274** 171–5
[14] Baránková H and Bárdoš L 2013 Optimization and performance of atmospheric fused hollow cathodes *Vacuum* **87** 128–31
[15] Haberland H, Kavais M and Mall M 1991 A new type of cluster clusterion source *Z. Phys.* **20** 413–5
[16] Klusoň J, Kudrna P, Kolpaková A, Picková I, Hubička Z and Tichý M 2013 Experimental study of the discharge in the low pressure plasma jet sputtering system *Contrib. Plasma Phys.* **53** 10–5
[17] Klusoň J, Kudrna P and Tichý M 2013 Measurement of the plasma, neutral flow velocities in a low-pressure hollow-cathode plasma jet sputtering system *Plasma Sources Sci. Technol.* **22** 015020
[18] Hubička Z 2012 *The Low Temperature Plasma Jet Sputtering Systems Applied for the Deposition of Thin Films* (Olomouc: Univerzita Palackého v Olomouci)
[19] de Araújo F O, de Almeida E O, Alves C, da Costa J A P and Dumelow T 2006 Deposition of TiO_2 on silicon by sputtering in hollow cathode *Surf. Coat. Technol.* **201** 2990–3
[20] Grattan K T V and Zhang Z Y 1995 *Fiber Optic Fluorescence Thermometry* (London: Chapman and Hall) 0412624702
[21] Kyuma K, Tai S, Sawada T and Nunoshita M 1982 Fiber-optic instrument for temperature measurement *IEEE J. Quantum Electron.* **18** 676–9

[22] Gemelli E and Camargo N H A 2007 Oxidation kinetics of commercially pure titanium *Rev. Matér.* **12** 525–31
[23] Pfau S, Tichý M, in Hippler R, Kersten H, Schmidt M, Shoenbach K-H, 2008 *Low Temperature Plasma Physics* (Berlin: Wiley-VCH)
[24] Leshkov S, Kudrna P, Chichina M, Klusoň J, Picková I, Virostko P, Hubička Z and Tichý M 2010 Spatial distribution of plasma parameters in dc-energized hollow cathode plasma jet *Contrib. Plasma Phys.* **50** 878–85
[25] Woodruff D P 2007 *Atomic Clusters: From Gas Phase to Deposited* (The Chemical Physics of Solid Surfaces vol 12) (Amsterdam: Elsevier)
[26] Eggersdorfer M L and Pratsinis E S 2014 Agglomerates, aggregates of nanoparticles made in the gas phase *Adv. Powder Technol.* **25** 71–90
[27] Schmidt-Ott A 2010 *Aerosol Methods for Nanoparticle Synthesis, Characterization, in Handbook on Nanophysics* (New York: CRC)
[28] Šícha M, Hubička Z, Tichý M, Novák M, Soukup L, Jastrabík L, Behnke J F, Kapička V, Kapoun K and Šerý M 1996 The interaction of the supersonic plasma-jet with the substrate in the RF plasma–chemical reactor *Contrib. Plasma Phys.* **36** 605–11
[29] Friedlander S K, Windeler R S and Weber A P 1994 Ultrafine particle formation by aerosol processes in turbulent jets—mechanisms scale-up *Nanostruct. Mater.* **4** 521–8

Surface & Coatings Technology 291 (2016) 123–129

Contents lists available at ScienceDirect

Surface & Coatings Technology

journal homepage: www.elsevier.com/locate/surfcoat

Crystalline structure and morphology of TiO_2 thin films deposited by means of hollow cathode plasma jet with supporting anode

R. Perekrestov [a,*], P. Kudrna [a], M. Tichý [a], I. Khalakhan [a], S. Daniš [a], G. Prodan [b], R. Vladoiu [b]

[a] Charles University in Prague, Faculty of Mathematics and Physics, V Holešovičkách 2, 180 00 Praha 8, Czech Republic
[b] Ovidius University, Faculty of Applied Sciences and Engineering, Department of Physics, Mamaia bd. 124, Constanta 900527, Romania

ARTICLE INFO

Article history:
Received 30 November 2015
Revised 20 January 2016
Accepted in revised form 11 February 2016
Available online 15 February 2016

Keywords:
Plasma jet
DSSC
Columnar structure
Titanium dioxide
Anatase
Rutile

ABSTRACT

TiO_2 thin films with developed structure were deposited by means of a hollow cathode plasma jet (HCPJ) in a DC regime with a supporting anode. The influence of the plasma temperature on the surface morphology and crystalline structure of the thin films under different deposition conditions was studied. Diagnostics of the thin films structure was carried out using XRD, SEM, EDX and TEM methods. One batch of samples was annealed at a temperature of 400 °C in atmospheric conditions as a comparison with the crystalline structure and morphology of unannealed samples. The presence of two crystalline polymorphs of rutile and anatase in the films was discussed. The vacuum system was improved for an extended deposition of non-conductive materials without terminating the discharge and cleaning of the deposition chamber. The aim of this investigation was to prepare the vacuum system for the fabrication of photo electrodes which are the main functional part in dye-sensitized solar cells. The test DSSCs (dye-sensitized solar cells) were prepared from low-cost materials (raspberry/hibiscus natural dye-sensitizers and candle soot counter electrode) in order to check the quality of the films, with a highest conversion efficiency $\eta = 0.66\%$ and a fill factor $FF = 62\%$.

1. Introduction

Titanium dioxide (titania) is one of the most intensively used materials, especially in the energy sector of modern science and technology. There are a number of examples of its application in the fabrication of lithium ion batteries [1,2], visible light-driven photocatalytic hydrogen production [3] and photo electrodes for dye-sensitized solar cells (DSSCs) e.g. [4,5]. Titanium dioxide was recognized as the best solution for the fabrication of DSSC photo electrodes in spite of its low electronic transfer and enhanced charge recombination because of its stability, high chemical resistance and low cost. Titanium dioxide in anatase phase exhibits better light absorption efficiency and photocatalytic degradation of organic compounds under UV radiation which makes it preferable to the rutile phase [6]. The efficiency of TiO_2 as a catalyst or photo electrode active layer reaches its maximum when charge transport is significantly faster than the hole–electron recombination. When the titania is used as an electrode in dye sensitized solar cells, the charge transport is highly dependent on the film morphology and associated with the particle network, i.e. the number of inter-particle connections, or the lack thereof, can lead to the hole–electron recombination [7]. Planar thin film has shown negligible light conversion efficiency, therefore all efforts are focused on the optimization of the film surface morphology. Researchers managed to obtain TiO_2 nanostructures in a form of nanorods [8], nanoparticles [9], columnar structures [10], nanofiber networks, and porous matrix [7], etc.

A huge variety of synthesis methods is available for metal/non-metal doped and undoped TiO_2 thin film preparation. These methods include chemical vapor deposition [10,11], sol–gel [12], hydrothermal [13], electrophoretic deposition [14], and flame-aerosol [15]. The reactive sputtering by means of the low pressure HCPJ technique [16–18] belongs to the branch of plasma enhanced chemical vapor deposition (PECVD) methods. This method provides high purity, good adhesion with the substrate and control over the thickness and the morphology of the thin films. The basic principle of this method lies in sputtering the inner surface of a tubular hollow cathode with Ar^+ ions which is followed by oxidation and deposition of the sputtered material on the substrate. A more widely spread and through quite system for thin film deposition is planar magnetron, which can be operated in a DC [19,20], pulsed DC including HiPIMS [11,21,22] and RF [10,23,24] power regime. The magnetron sputtering system is operated under the glow and anomalous glow of discharge conditions. One of the significant advantages of HCPJ over magnetron sputtering is the continuous flow of the working gas which 1) helps to achieve a higher purity of the films and 2) gives us control over the divergence of the flow of the sputtered atoms. However, magnetron sputtering allows thin film deposition on larger areas with less difference in a thickness. Both the HCPJ and the planar magnetron can be powered in DC [16], pulsed DC [25] an RF [26] regime depending on the objectives. For the deposition of non-conductive coatings the RF powered sputtering systems are

* Corresponding author.
E-mail address: mr.perekrestov@gmail.com (R. Perekrestov).

http://dx.doi.org/10.1016/j.surfcoat.2016.02.026
0257-8972/

commonly used because of several crucial advantages over DC powered systems. Among them is the possibility of the sputtering of non-conductive materials, where there are no disappearing anode problems and the charge is not accumulating on the chamber walls or other inner parts of the vacuum system. However, DC discharge is much easier to exploit as it performs in stable deposition conditions with a well defined cathode sputtering area and does not interfere with other electrical devices. In the case of short-term deposition of non-conductive thin films there were no issues with the HCPJ exploitation in DC regime (film thickness from several tens up to hundreds nanometers). The problems arose during a long-term deposition of titania thin film lasting several hours when the inner surfaces of the main chamber were gradually coated by a non-conductive layer. This resulted in the effective insulation of the anode followed by the interruption of a discharge. This effect was monitored as a decrease of the potential of any floating part immersed in the discharge, e.g. the floating (i.e. not grounded) sampling orifice of the mass-spectrometer. In some cases this resulted in the random migration of the anode's active part (i.e. the part carrying the discharge current) over the conductive parts inside of the main chamber, e.g. the sample holder, shutter, table, etc., depending on their distance from the cathode and the thickness of the insulation layer.

The thickness of the photo electrode in DSSC varies from units up to tens of micrometer. If we take into account the relatively low deposition rate, which reaches maximally several nm s^{-1}, the stability of the discharge becomes an acute problem. In order to eliminate this negative effect we introduced, into the deposition chamber, a supporting anode which was slightly positive with respect to the ground and therefore drained almost the whole electron current from the discharge. The deposition conditions of the investigated films partially coincide with the conditions we used in [16], where the crystalline structure of films was not studied and deposition occurred without the supporting anode. This motivated us to improve our study using crystalline structure diagnostics since the crystallinity plays a crucial role for application purposes.

2. Experimental setup

2.1. Vacuum system

A hollow cathode plasma jet is installed in a grounded vacuum chamber that was designed for UHV conditions. The principal scheme of the HCPJ is shown in Fig. 1 (left). The main functional part of the system is cylindrically-shaped pure (99.995%) titanium hollow cathode with a through hole along the axis. The length of the cathode is 29 mm, and the inner and outer diameters are 5 and 8 mm, respectively. The hollow cathode was fixed by the water-cooled copper blocks and insulated from the rest of the system by means of a lava ceramic shield. Argon with the purity of 99.999% was introduced through the inlet at the top of the hollow cathode.

Oxygen was introduced into the main chamber via the separate inlet, since its direct introduction to the hollow cathode results in cathode poisoning [27] and discharge instability. The HCPJ was powered by an Advanced Energy MDX 500 power supply in the current stabilizing mode. The supporting anode was installed in a system below the substrate holder as it is shown in Fig. 1 (right). The supporting electrode is a cylindrical iron wire insulated by the ceramic shielding tube. The active part of the anode is 7 mm long and 1 mm in diameter. The anode was positively biased with respect to the ground (+18 V) by Agilent E3633A DC power supply that enabled us to measure the supporting anode current separately from the cathode current. During the deposition it was continuously heated by the electron and, probably, negative ion (O^-) current which prevented the loss of conductivity. This supporting anode drained almost the whole current from plasma because of its positive bias and sharp geometry, which created the high electric field lines in front of its tip. The anodic instabilities due to the probable double layer formation around the supporting electrode did not cause fluctuations of the discharge current greater than 5%. Consequently, we assumed that the influence of current fluctuations on the deposition process can be neglected.

2.2. Preparation of the TiO_2 thin films

In order to achieve the high purity of the films the vacuum chamber was pumped down to a base pressure of $1 \cdot 10^{-4}$ Pa before the start of the deposition. Pumping the system down to lower pressures adds no advantage considering the purity of the working gas and cathode material. The pressure in a main chamber during the deposition was sustained at the value of $p = 100$ Pa. The discharge ran for 20 min in order to purify the surface of the cathode from the absorbed active gases, water, etc. The samples were deposited on silicon (111) and glass substrates for the diagnostics of the morphology and crystalline structure of the films, respectively. The substrates were placed at the distance of 42 mm from the cathode. One batch of the samples was annealed in the muffle furnace in atmospheric conditions and at a temperature of 400 °C for 1 h. For all samples deposited for structural and surface diagnostics the oxygen flow rate was 0.5 sccm which was enough for complete oxidation of titanium. The deposition conditions of the samples are given in Table 1.

TEM characterization was performed on Philips CM120ST microscope, working at 100 kV high voltage. Transmission electron microscopy requires a very thin sample, obtained by a method of preparation that depends on the characteristics of the original sample. In these cases, we have thin films on a Si substrate. We selected a quick method, which allowed us to prepare TEM grids. The morphology of the deposited layers was examined by means of scanning electron microscopy (SEM) using a MIRA 3 Tescan microscope at 30 keV electron beam energy. XRD measurements were carried out to determine the crystalline structure of the deposited thin films using the Seifert XRD7

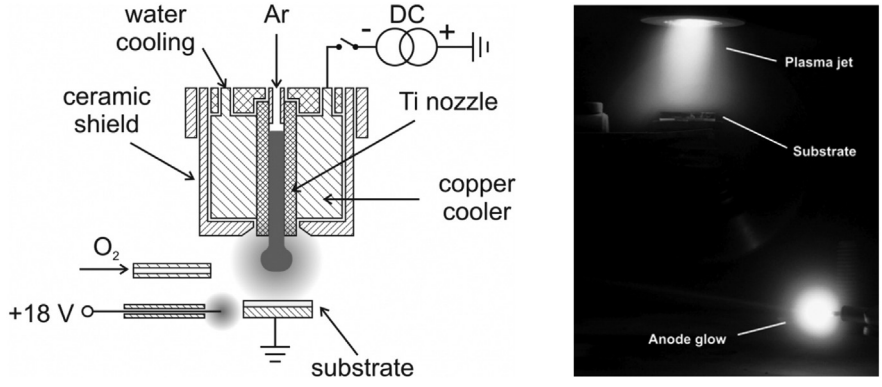

Fig. 1. The scheme of the HCPJ sputtering system with supporting electrode for deposition of metal oxide films in DC mode (left) and photo of the system during the deposition (right).

Table 1
Deposition conditions of the samples' symbol meaning: $Flow_{Ar}$ — argon flow rate, I_d — discharge current, T_a — annealing temperature, t — deposition time.

	$Flow_{Ar}$ [sccm]	I_d [mA]	T_a [°C]	t [min]
S1	100	200	–	180
S2	100	200	400	180
S3	300	200	–	120
S4	300	200	400	120
S5	300	400	–	45
S6	300	400	400	45

diffractometer with parallel-beam geometry, Cu K_α radiation and fixed angle of incidence of X-rays $\Omega = 5°$.

2.3. Preparation of the DSSCs for the quality control test of the TiO_2 films quality

We optimized the deposition conditions of the photo electrodes in order to achieve uniform thin films with a surface morphology similar to the samples S1–S4 at the higher deposition rates. The photo electrodes for DSSCs with a thickness of 5.4 μm and 20 μm were deposited on the glass substrate covered by ITO layer with a resistance of 10 Ω/square under the $Flow_{Ar} = 120$ sccm, $Flow_{O2} = 3$ sccm, p = 25 Pa, $I_d = 300$ mA and cathode-to-substrate separation of 30 mm. The deposition lasted for 6 h and 22 h for the samples with a thickness of 5.4 μm and 20 μm, respectively. The photo electrodes were annealed for 1 h in the muffle furnace at a temperature of 400 °C. We used hibiscus and raspberry [6] as low-cost dye-sensitizers. The photo electrodes were immersed in dye for 10 min. To fabricate the counter electrodes we placed the conductive glass over the candle flame for a few seconds, in this way we obtained a layer of black carbon soot. The frame, from the transparent scotch tape, was created around the photo active layer on the ITO electrode to prevent a short circuit between the electrodes. The solution of iodine in the ethylene glycol was used as an electrolyte. Photovoltaic tests were carried out by measuring the J–U characteristic of the solar cells under the AM 1.5 G sunlight (ASTM G-173-03 standard, 100 mW/cm^2, see http://www.nrel.gov/solar_radiation/) simulated by the metal halide 575 W lamp equipped by the UV filter (<390 nm). The average deviation of the lamp spectrum from the standard cited above in the wavelength region 400–1100 nm was 4%. The J–U characteristics were measured by the source meter KEYSIGHT B2901A.

3. Results and discussion

3.1. Characterization of the morphology of the thin films

The presence of the heated supporting anode may cause the uncontrolled doping of the TiO_2 thin layer by evaporated iron atoms (anode material). The EDX analysis was carried out in order to make sure that the elemental composition of the film corresponds to the pure titanium dioxide, see Fig. 2. The iron Lα, Kα and Kβ lines are marked as references. The magnitude of the signal at the position of the iron reference lines remains at the level of noise. The presence of the silicon on the spectrum indicates that the penetration depth of this method is deeper than the thickness of the film and that we have detected the substrate. A small carbon peak corresponds to the impurities that emerged after the exposure of the sample to the atmosphere. It has been proven experimentally by XPS measurements of the samples deposited at the relevant conditions [16]. The EDX patterns we obtained from other samples are almost identical.

Samples S1 and S2 were deposited at the laminar regime of the plasma flow in HCPJ due to the comparably low working gas flow rate (100 sccm). This flow regime is characterized by a gradual expansion of the plasma plume caused by the diffusion of ions and neutrals in the direction determined by the vector of the pressure gradient. Thin

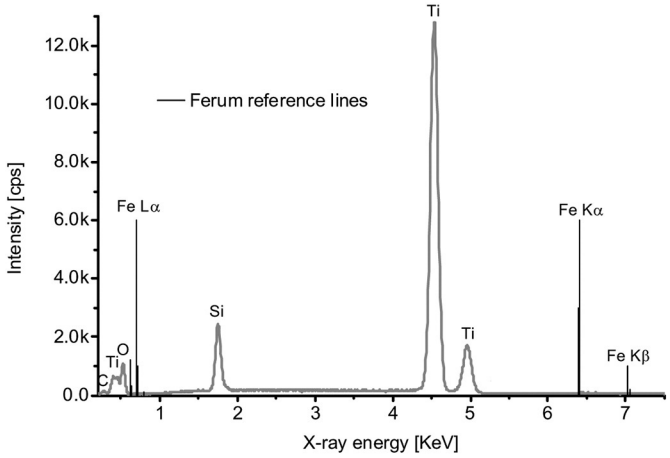

Fig. 2. EDX spectrum of the sample S6 with iron reference lines.

layers deposited at the low flow conditions are characterized by the good homogeneity and small difference in thickness over the area of the sample.

SEM images of the non-annealed S1 and annealed S2 samples are shown in Fig. 3. Annealing of the samples was carried out in order to demonstrate how the temperature affects the structure of the thin films, as annealing of a photo electrode is one of the steps in DSSC fabrication used to achieve film crystallization and better adhesion of TiO2 with the TCO layer. Numerous scientific reports on the crystallization of the titania films by annealing in a muffle furnace show that the pure anatase phase appears at an approximate temperature range from 300 up to 600 °C [7,28,29]. Anatase is preferable in the solar cell application over rutile, thus the temperature of annealing was kept at 400 °C.

The analysis of the surface morphology of the samples, see Fig. 3a, b revealed the presence of fine and ultrafine cracks in the films. A film deposited at a high temperature and then cooled will develop biaxial in-plane tensile stresses if the thermal expansion coefficient of the film differs from the substrate. The temperature of the samples S1 and

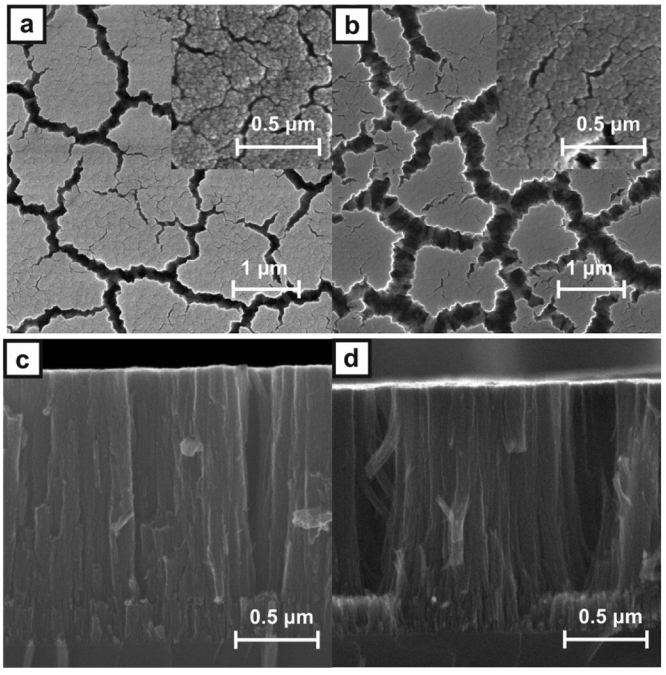

Fig. 3. SEM images of the surface of the unannealed S1 (a) and annealed S2 (b) samples as well as of the cross section of the samples S1 (c) and S2 (d).

S2 during deposition sustained at the constant value of 120 ± 5 °C, which might cause cracks after their cooling [16].

The presence of nanoparticles in the film is another effect that might contribute to the emergence of cracks [30]. Nanoparticles in thin TiO_2 films were investigated in detail on the thinner films deposited under relevant conditions [16]. The cracks exhibit a fractal structure which lies in the repetition of the film patterns at the higher magnification, see inserted images in Fig. 3a, b. Fine cracks of unannealed film are approximately 0.1–0.2 μm in width and were enlarged twice after the annealing. However, the thermal influence caused the opposite effect on the structure of ultrafine cracks. Their width remained the same and even a slight constriction was observed. The width of ultrafine cracks varied in a range from units up to several tens of nanometer. The decrease of the occurrence of ultrafine cracks and general ordering of the crystalline structure can explain the broadening of fine cracks after annealing. Samples S3 and S4 deposited at the higher working gas flow rate reveal a similar surface structure and the tendency of the fine cracks to broaden after the annealing.

The cross sections of the samples S1 and S2 are depicted in Fig. 3c, d. The structure of the film shows the tendency of columnar growth which results in good adhesion within the one "column" and weak interconnections between them. Both samples have good adhesion with a silicon substrate regardless of the annealing. The thicknesses of the films are 1.69 μm and 1.53 μm for the samples S1 and S2 respectively which indicate the slight deviation in the deposition rate (~10%) along the horizontal axis, as the samples were deposited during the same experiment. This is associated with the peculiarities of the deposition technique, which has much less divergence of the flow of sputtered matter in comparison with the more widely used magnetron sputtering. This divergence is mostly affected by such deposition parameters as the working gas flow rate and pressure in the main chamber.

High values of these parameters result in lesser divergence of the plasma flow and subsequently sputtered matter which is driven by plasma flow. The calculated deposition rate was 0.15 nm s^{-1} for the samples S1, S2 and 0.13 nm s^{-1} for samples S3, S4. Generally, the presence of the cracks in the films is an undesirable feature and a great deal scientific effort is focused on its elimination [31,32]. In our case it may cause a rather positive effect, as these cracks do not extend through the entire film as it is shown in Fig. 3 d and cannot cause a short circuit between electrodes in DSSCs. Moreover, they can effectively improve the efficiency of the photo electrode, since the absorption of the dye-sensitizer will occur not only on the surface but also in the bulk of the thin film on condition of their retaining stability during exposure to a steady stream of sunlight.

The regime of deposition under an argon gas glow of 300 sccm and a discharge of $I_d = 400$ mA is characterized by a higher turbulence and the well-defined cylindrical shape of the plasma plume. Samples S5 and S6 deposited in this regime can be conditionally divided into three different regions: (i) the columnar structures, Fig. 4a, d, (ii) the agglomerated particle-rich region Fig. 4c, e and (iii) transition region, Fig. 4b. Distribution of these regions on the surface of the substrate has an axial symmetry with respect to the plasma plume axis. For the better understanding we added the scheme of the sample regions in Fig. 4a, where symbols correspond to the designation of Fig. 4a–c and the bottom-right corner of the sample scheme is the nearest to the discharge axis. Region "b", Fig. 4b, is a transition region which is characterized by the presence of both aforementioned structures. The growth of the spiky columns is mostly caused by the interaction of the elevated-temperature plasma flow with the sample. The temperature measurements in [16] show the sharp temperature gradient under the high values the working gas flow rate and discharge current, since the discharge power under these conditions is concentrated in the relatively narrow plasma plume.

The temperature gradient value was in the order of 10^2 °C cm^{-1} along the horizontal axis. The absolute value of the temperature has an exponential dependence on the horizontal coordinate and exceeds 250 °C at the distance of 1 cm from the plasma plume axis under the conditions of deposition which correspond to the samples S5 and S6 (the limit of the fiber optic thermometer is 300 °C). The annealing caused the negligible influence on the morphology; the surface morphology of the sample S5 is almost identical to S6.

The agglomerated particles were found in regions "b" and "c". We assumed that the agglomeration occurred in a gas phase in a process of particle vs particle collision. This was confirmed by the high magnification TEM image of the single agglomerated particle, see Fig. 4f. The nanostructure of the agglomerated particles consists of spherical nanoparticles embedded in amorphous matrix. Electron diffraction has shown an amorphous crystalline structure with traces of anatase. A discussion on the growth mechanisms of the agglomerated particles is given in [16].

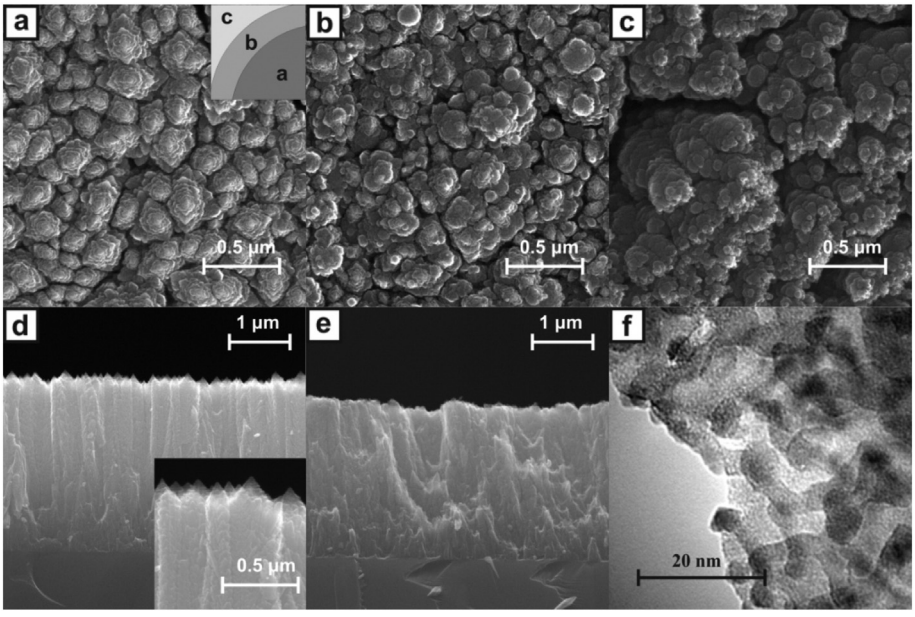

Fig. 4. SEM images of the surface of the sample S6 taken at different positions (a–c). The scheme of regions on sample S6 is shown at the top-right corner of the figure (a). The cross sections (d) and (e) of the same sample are measured in regions "a" and "c" respectively. The high magnification TEM image of the structure of agglomerated particle shows the panel (f).

The cross sections of the sample S6 from regions "a" and "c" are shown in Fig. 4d, e, respectively. The film has good adhesion with the substrate and a surprisingly low number of fine cracks, considering the high temperature of the substrate during deposition. The slight inhomogeneity in the thickness can be explained in a similar way as were the samples S1 and S2. The deposition process is characterized by the significantly higher deposition rate of 1.16 nm s^{-1}; in comparison with the samples S1–S4. Inhomogeneity of the samples makes them hardly applicable in the fabrication of solar cells, since it will be hard to analyze the results obtained. This problem was easily solved by adjusting the sample position within the center of the discharge axis and putting it closer to the discharge outlet. In this case we obtained the uniform thin film represented only by the spiky/columnar structure (region "a"). The problems arise with the reproduction of the results from the region "c", since the agglomerated particles are concentrated in the outer layer of the plasma plume.

3.2. Crystalline structure of the thin films

The crystalline structure of the samples S1–S6 was analyzed by means of the XRD method. The non-annealed samples S1 and S3 exhibited an amorphous structure as shown in Fig. 5 a. Annealing of the samples at a temperature of 400 °C launched the processes of crystallization (samples S2, S4) which is represented by the pure anatase phase. Such results are in agreement with previous reports on crystallization of TiO_2 [12]. The crystalline anatase phase was confirmed by (101), (004), (200), (105) and (204) diffraction peaks. The most interesting finding is the asymmetrical crystallization of the samples S2 and S4. The highest peak of the sample S4 is at $2\theta = 37.8°$ which corresponds to the plane (004), while the highest peak of the sample S2 is at $2\theta = 25.3°$ which corresponds to the plane (101).

The samples S5 and S6 show completely different crystalline structures, see Fig. 5b. The presence of rutile and anatase crystalline forms was detected in both samples regardless of annealing. The crystalline rutile phase is dominant and was confirmed by (110), (101), (111), (211) and (220) diffraction peaks. The highest peak is at the $2\theta = 54.3°$ and corresponds to the plane (211). Anatase is the less abundant phase in samples S5 and S6. It is represented by (101), (004), (200), (204) and (215) diffraction peaks, where (101) is the highest. We assume that such a mixture of phases can be explained by the elevated temperature of the samples due to the interaction with the plasma flow. This can also be inferred from the reported TiO_2 phase diagrams, e.g. in [33], since rutile phase shows up in temperatures over 600 °C. However, the temperature of this transition in our system can be different, since the processes in the HCPJ system, which is operated in the supersonic flow regime [34], are much more complicated than annealing in the muffle furnace in atmospheric conditions. Rutile is the equilibrium crystalline form of titania, hence the annealing at the temperature of 400 °C can only results in a crystallization of the amorphous part of the samples into anatase phase. This assumption is in agreement with the results in Fig. 5b, where the intensity of the anatase peaks is significantly higher in the pattern of the annealed sample S6. The crystalline structure and morphology of the films are strongly connected, therefore we assume that the columnar structures in Fig. 4a, d correspond to the rutile phase (region "a"). In the transition region "b", Fig. 4b, both phases are present, and region "c" is represented by a mixture of anatase and amorphous phase, Fig. 4c, e, which turned into anatase after annealing.

The results that correspond to Fig. 5a are in agreement with previous reports on the amorphous TiO_2 annealing in a muffle furnace at the atmospheric conditions e.g. [12] and reported pressure vs temperature phase diagrams [33,35]. In the work [11], the authors investigate the deposition of titania thin film by means of the HiPIMS technique. An XRD analysis of the investigated thin films revealed the presence of anatase and rutile phases as a function of the deposition pressure. The explanation was also based on the values of the energy influx on the substrate, however, the higher energy influx led to a growth of amorphous film. The reason for this discrepancy is not clear yet; it might be connected with the high energy electron content in HiPIMS plasma. Further discussion of the processes of crystallization during plasma processing is given in [36].

3.3. Characterization of the test samples of DSSCs

Test samples of DSSCs with different active areas (S_a), natural dye-sensitizers and thicknesses of the TiO_2 layer were assembled and tested under the AM 1.5 G conditions. It is hard to achieve high conversion efficiency using such low-cost materials as hibiscus/raspberry dye and candle soot. However, a comparison with other relevant results and an analysis of the parameters calculated from J–U characteristics can give us a general idea about the quality of the TiO_2 thin films as well as perspective of their further application.

We used an EDX technique to carry out the elemental analysis of the carbon soot layer. Carbon, indium, tin, oxygen and silicon peaks were detected. They correspond to the black carbon soot, ITO layer and glass substrate. Nevertheless, we assumed that this film could contain unburned hydrocarbons e.g. paraffin from the candle which is not possible to detect by EDX. It may affect the conductivity of the carbon and reduce the efficiency of the solar cells. Another disadvantage of the carbon soot lies in its weak adhesion with the conductive glass, which resulted in the destruction of the carbon layer at the slightest longitudinal shear of the electrodes. The SEM image of the carbon soot is shown in Fig. 6b. The film consists of fine carbon nanoparticles with a mean diameter of several tens of nm. Such developed highly-porous

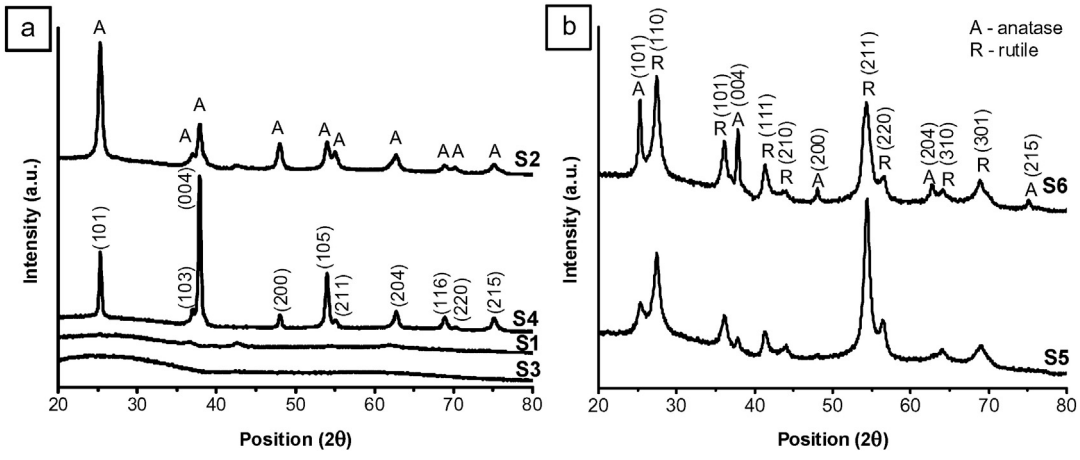

Fig. 5. XRD patterns of the samples S1–S4 (a) and S5–S6 (b). The Miller indices of anatase and rutile phases are given.

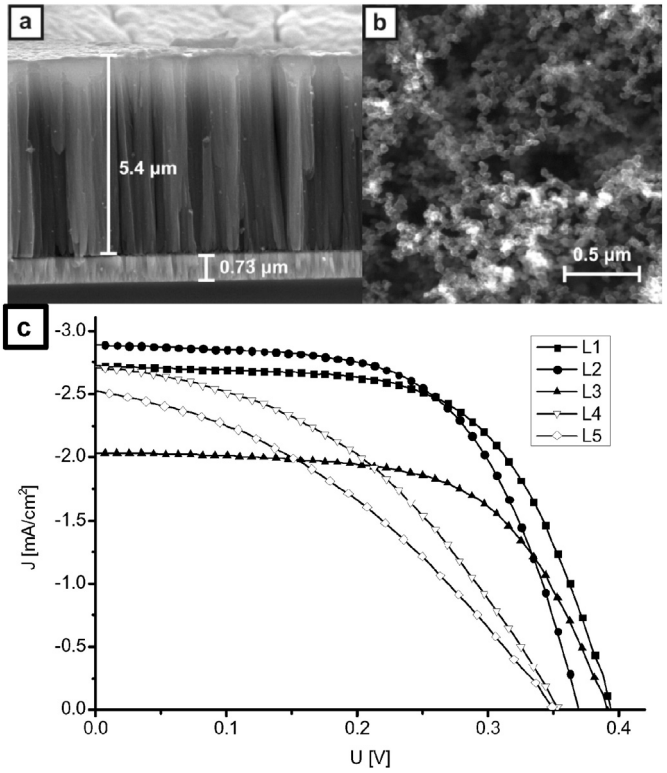

Fig. 6. SEM images of the cross section of the photo electrode with the thickness of 5.4 μm (a) and the structure of the black carbon soot layer of the counter electrode (b). Current density versus voltage of the DSSC samples L1–L5 under the AM 1.5 G conditions (100 mW cm^{-2}).

structures can greatly improve the I_3^- reduction efficiency. Moreover, there are examples of when the high efficiency of solar cells was achieved using carbon soot solution e.g. in perovskite solar cells [37].

The cross section of the photo electrode with TiO_2 thickness of 5.4 μm is shown in Fig. 6a. It exhibits a similar structure as samples S1–S4 (Fig. 3). The thickness of the conductive ITO layer is 0.73 μm. The parameters of the DSSCs estimated from the J–U characteristics in Fig. 6c are given in Table 2. Raspberry dye gave a slightly better conversion efficiency (η) in comparison with hibiscus. The value of the short-circuit current was greatly improved by the decrease of the S_a of photo electrodes. This might be connected with the lower series resistance (R_s) which was measured from the first quadrant of the J–U curves in the dark and is half as much for the samples with smaller area (L1, L2). The samples L1–L3 have shown a much better fill factor (FF) than L4–L5 due to the thicker TiO_2 layers which has better light-absorption in comparison with the thinner samples. A relatively high FF value indicates good adhesion between TiO_2 and the ITO layer and the absence of holes in the film, which may result in a short circuit between electrodes (low shunt resistance). The highest conversion efficiency was obtained at the sample L1 with FF = 62% and η = 0.66%.

Table 2
The parameters of test samples of DSSCs.

Sample	Dye-sensitizer	Sa [cm2]	TiO2 thickness [μm]	Isc [mA]	Uoc [V]	FF [%]	η [%]	Rs [Ω]
L1	raspberry	0.21	20	2.72	0.393	62	0.66	10.9
L2	hibiscus	0.22	20	2.88	0.370	61	0.64	11.0
L3	hibiscus	0.48	20	2.03	0.391	61	0.48	18.5
L4	raspberry	0.49	5.4	2.7	0.355	42	0.41	22.7
L5	hibiscus	0.36	5.4	2.53	0.350	37	0.33	21.4

4. Conclusions

The vacuum system with HCPJ was modified in order to achieve a stable and continuous deposition of the metal-oxide films in the DC regime. The efficiency achieved by the introduction of the supporting anode to the main chamber was proven by the deposition of the DSSC TiO_2 photo electrode for 22 h without termination of the discharge. Deposited thin titania films were checked for the contamination of iron dopants, which can be present due to the high temperature of the iron supporting anode. The peaks that correspond to Fe were not found at the EDX spectrum.

The morphology and crystalline structure of deposited TiO_2 thin films were analyzed by SEM, TEM and XRD methods. The samples deposited under the discharge current 200 mA (samples S1–S4) exhibit a presence of fine and ultrafine cracks. The width of the cracks was increased after the annealing of the samples. The crystalline structure of these films is represented by amorphous phase, which turns into anatase after the annealing in the muffle furnace in atmospheric conditions at a temperature of 400 °C. The films deposited under the high working gas flow rate (300 sccm) and discharge current 400 mA (samples S5 and S6) have shown a developed surface structure which was conditionally divided onto three regions: spiky columnar structures ("a"), transition region ("b") and the region with agglomerated particles ("c"). The crystalline structure of region "a" is mostly represented by rutile phase, region "b" is a mixture of both anatase and rutile phases and region "c" exhibits an anatase/amorphous crystalline structure, which turned into anatase after annealing.

DSSCs were assembled in order to check the perspective of the application of the TiO_2 thin films deposited by means of HCPJ. The test samples were made of low-cost materials such as black carbon soot (counter electrode) and natural dye-sensitizers: raspberry and hibiscus. Natural dye solutions were chosen due to their availability and comparably high conversion efficiency among the other natural dye-sensitizers [6]. The best results were achieved in the sample L1 (raspberry) with FF = 62% and conversion efficiency η = 0.66%. Sample L2 (hibiscus) was only slightly less efficient. In comparison with other relevant results with given natural dyes [38,39], higher results were achieved in [40], η = 1.5% with raspberry dye and η = 0.75% with hibiscus dye. However, in this work the Pt counter electrode was used compared to gold in [31]. The comparably high value of fill factor indicated that the development of DSCCs can offer high quality results using TiO_2 films deposited by HCPJ.

Acknowledgment

Financial support by the Czech Science Foundation, grant no. 15-00863S and by Charles University Grant Agency, grant no. 268115 is gratefully acknowledged. This work was also supported by CNDI–UEFISCDI, project 78/2013, PN-II-ID-PCE-2012-4-0059.

References

[1] Y. Tang, Y. Zhang, J. Deng, J. Wei, H.L. Tam, B.K. Chandran, et al., Mechanical force-driven growth of elongated bending TiO_2-based nanotubular materials for ultrafast rechargeable lithium ion batteries, Adv. Mater. 26 (2014) 6111–6118, http://dx.doi.org/10.1002/adma.201402000.
[2] L. Wang, Z. Nie, C. Cao, S. Khalid, Y. Wu, X. Xu, Carbon-wrapped TiO_2 nanocubes exposed with (001) active facets for high-rate and long-life lithium-ion batteries, J. Power Sources 302 (2016) 259–265, http://dx.doi.org/10.1016/j.jpowsour.2015.10.072.
[3] L. Li, J. Yan, T. Wang, Z.-J. Zhao, J. Zhang, J. Gong, et al., Sub-10 nm rutile titanium dioxide nanoparticles for efficient visible-light-driven photocatalytic hydrogen production, Nat. Commun. 6 (2015) http://dx.doi.org/10.1038/ncomms6881.
[4] S. Mathew, A. Yella, P. Gao, R. Humphry-Baker, B.F.E. Curchod, N. Ashari-Astani, et al., Dye-sensitized solar cells with 13% efficiency achieved through the molecular engineering of porphyrin sensitizers, Nat. Chem. 6 (2014) 242–247, http://dx.doi.org/10.1038/nchem.1861.
[5] S.G. Hashmi, M. Ozkan, J. Halme, K.D. Misic, S.M. Zakeeruddin, J. Paltakari, et al., High performance dye-sensitized solar cells with inkjet printed ionic liquid electrolyte, Nano Energy 17 (2015) 206–215, http://dx.doi.org/10.1016/j.nanoen.2015.08.019.

[6] S. Shalini, R. Balasundara Prabhu, S. Prasanna, T.K. Mallick, S. Senthilarasu, Review on natural dye sensitized solar cells: operation, materials and methods, Renew. Sustain. Energy Rev. 51 (2015) 1306–1325, http://dx.doi.org/10.1016/j.rser.2015.07.052.
[7] Z. Zander, R. Yagloski, J. DeCoste, D. Zhang, B.G. DeLacy, One-pot synthesis of high aspect ratio titanium dioxide nanorods using oxalic acid as a complexing agent, Mater. Lett. 163 (2016) 39–42, http://dx.doi.org/10.1016/j.matlet.2015.10.041.
[8] Y. Tang, C. Wang, Y. Hu, L. Huang, J. Fu, W. Yang, Preparation of anatase TiO_2 nanorods with high aspect ratio for high-performance dye-sensitized solar cells, Superlattice. Microst. 89 (2016) 1–6, http://dx.doi.org/10.1016/j.spmi.2015.11.003.
[9] S.M. Gupta, M. Tripathi, A review of TiO_2 nanoparticles, Chin. Sci. Bull. 56 (2011) 1639–1657, http://dx.doi.org/10.1007/s11434-011-4476-1.
[10] S.H. Kang, M.-S. Kang, H.-S. Kim, J.-Y. Kim, Y.-H. Chung, W.H. Smyrl, et al., Columnar rutile TiO_2 based dye-sensitized solar cells by radio-frequency magnetron sputtering, J. Power Sources 184 (2008) 331–335, http://dx.doi.org/10.1016/j.jpowsour.2008.05.089.
[11] V. Straňák, M. Čada, M. Quaas, S. Block, R. Bogdanowicz, Š. Kment, et al., Physical properties of homogeneous TiO_2 films prepared by high power impulse magnetron sputtering as a function of crystallographic phase and nanostructure, J. Phys. Appl. Phys. 42 (2009) 105204, http://dx.doi.org/10.1088/0022-3727/42/10/105204.
[12] S. Miszczak, B. Pietrzyk, Anatase–rutile transformation of TiO_2 sol–gel coatings deposited on different substrates, Ceram. Int. 41 (2015) 7461–7465, http://dx.doi.org/10.1016/j.ceramint.2015.02.066.
[13] X. Chen, S.S. Mao, Titanium dioxide nanomaterials: synthesis, properties, modifications, and applications, Chem. Rev. 107 (2007) 2891–2959, http://dx.doi.org/10.1021/cr0500535.
[14] W.-S. Kuo, M.-T. Li, Pretreatment of color filter wastewater towards biodegradable by Fresnel-lens-assisted solar TiO_2 photocatalysis, Int. J. Photoenergy 2012 (2012) 1–8, http://dx.doi.org/10.1155/2012/387052.
[15] Y.K. Kho, W.Y. Teoh, L. Mädler, R. Amal, Dopant-free, polymorphic design of TiO_2 nanocrystals by flame aerosol synthesis, Chem. Eng. Sci. 66 (2011) 2409–2416, http://dx.doi.org/10.1016/j.ces.2011.02.058.
[16] R. Perekrestov, P. Kudrna, M. Tichý, The deposition of titanium dioxide nanoparticles by means of a hollow cathode plasma jet in dc regime, Plasma Sources Sci. Technol. 24 (2015) 035025, http://dx.doi.org/10.1088/0963-0252/24/3/035025.
[17] Z. Hubička, The Low Temperature Plasma Jet Sputtering Systems Applied for the Deposition of Thin Films, Univerzita Palackého v Olomouci, Olomouc, 2012.
[18] F.O. de Araújo, E.O. de Almeida, C. Alves, J.A.P. da Costa, T. Dumelow, Deposition of TiO_2 on silicon by sputtering in hollow cathode, Surf. Coat. Technol. 201 (2006) 2990–2993, http://dx.doi.org/10.1016/j.surfcoat.2006.06.015.
[19] K. Ono, M. Wakabayashi, Y. Tsukakoshi, Y. Abe, Decorative black TiCxOy film fabricated by DC magnetron sputtering without importing oxygen reactive gas, Appl. Surf. Sci. 364 (2016) 69–74, http://dx.doi.org/10.1016/j.apsusc.2015.12.009.
[20] V. Johánek, M. Václavů, I. Matolínová, I. Khalakhan, S. Haviar, V. Matolín, High low-temperature CO oxidation activity of platinum oxide prepared by magnetron sputtering, Appl. Surf. Sci. 345 (2015) 319–328, http://dx.doi.org/10.1016/j.apsusc.2015.03.108.
[21] M. Bowes, P. Poolcharuansin, J.W. Bradley, Negative ion energy distributions in reactive HiPIMS, J. Phys. Appl. Phys. 46 (2013) 045204, http://dx.doi.org/10.1088/0022-3727/46/4/045204.
[22] A.P. Ehiasarian, R. New, W.-D. Münz, L. Hultman, U. Helmersson, V. Kouznetsov, Influence of high power densities on the composition of pulsed magnetron plasmas, Vacuum 65 (2002) 147–154.
[23] M. Dobromir, A.V. Manole, V. Nica, R. Apetrei, M. Neagu, D. Luca, Analyzing the development of N-doped TiO₂ thin films deposited by RF magnetron sputtering, Sens. Lett. 11 (2013) 675–678, http://dx.doi.org/10.1166/sl.2013.2936.
[24] M. Dobromir, R.P. Apetrei, S. Rebegea, A.V. Manole, V. Nica, D. Luca, Synthesis and characterization of RF sputtered WO3/TiO2 bilayers, Surf. Coat. Technol. 285 (2016) 197–202, http://dx.doi.org/10.1016/j.surfcoat.2015.11.031.
[25] P. Kudrna, J. Klusoň, S. Leshkov, M. Chichina, I. Picková, Z. Hubička, et al., A study of plasma parameters in hollow cathode plasma jet in pulse regime, Contrib. Plasma Phys. 50 (2010) 886–891, http://dx.doi.org/10.1002/ctpp.201010150.
[26] Z. Hubicka, G. Pribil, R.J. Soukup, N.J. Ianno, Investigation of the rf and dc hollow cathode plasma-jet sputtering systems for the deposition of silicon thin films, Surf. Coat. Technol. 160 (2002) 114–123, http://dx.doi.org/10.1016/S0257-8972(02)00389-4.
[27] J.E. Polk, A.M. Capece, Materials characterization of impregnated W and W–Ir cathodes after oxygen poisoning, Appl. Surf. Sci. 338 (2015) 27–34, http://dx.doi.org/10.1016/j.apsusc.2015.02.116.
[28] M. Hamadanian, V. Jabbari, A. Gravand, Dependence of energy conversion efficiency of dye-sensitized solar cells on the annealing temperature of TiO_2 nanoparticles, Mater. Sci. Semicond. Process. 15 (2012) 371–379, http://dx.doi.org/10.1016/j.mssp.2011.12.004.
[29] L. Que, Z. Lan, W. Wu, J. Wu, J. Lin, M. Huang, High-efficiency dye-sensitized solar cells based on ultra-long single crystalline titanium dioxide nanowires, J. Power Sources 266 (2014) 440–447, http://dx.doi.org/10.1016/j.jpowsour.2014.05.022.
[30] J. González-Benito, E. Castillo, J.F. Caldito, Coefficient of thermal expansion of TiO_2 filled EVA based nanocomposites. A new insight about the influence of filler particle size in composites, Eur. Polym. J. 49 (2013) 1747–1752, http://dx.doi.org/10.1016/j.eurpolymj.2013.04.023.
[31] R. Ashiri, A. Nemati, M. Sasani Ghamsari, Crack-free nanostructured $BaTiO_3$ thin films prepared by sol–gel dip-coating technique, Ceram. Int. 40 (2014) 8613–8619, http://dx.doi.org/10.1016/j.ceramint.2014.01.078.
[32] X. Tang, Crack-free TiO_2 thin films with selfassembling nano-particles fabricated through in-situ sol–gel processing in reverse micelles, Surf. Coat. Technol. 221 (2013) 37–43, http://dx.doi.org/10.1016/j.surfcoat.2013.01.025.
[33] D.A.H. Hanaor, C.C. Sorrell, Review of the anatase to rutile phase transformation, J. Mater. Sci. 46 (2011) 855–874, http://dx.doi.org/10.1007/s10853-010-5113-0.
[34] L. Bárdoš, I. Štěpánek, G. Karwasz, Neutral gas flow velocity profiles in the jet plasma-chemical reactor, Vacuum 40 (1990) 449–452.
[35] F. Dachille, P.Y. Simons, R. Roy, Pressure–temperature studies of anatase, brookite, rutile and TiO_2-II, Am. Miner. 53 (1968) 1929–1939.
[36] H. Kersten, H. Deutsch, H. Steffen, G.M.W. Kroesen, R. Hippler, The energy balance at substrate surfaces during plasma processing, Vacuum 63 (2001) 385–431, http://dx.doi.org/10.1016/S0042-207X(01)00350-5.
[37] Z. Wei, K. Yan, H. Chen, Y. Yi, T. Zhang, X. Long, et al., Cost-efficient clamping solar cells using candle soot for hole extraction from ambipolar perovskites, Energy Environ. Sci. 7 (2014) 3326–3333, http://dx.doi.org/10.1039/C4EE01983K.
[38] N.T. Mary Rosana, D. Joshua Amarnath, K.L. Vincent Joseph, A. Suresh, S. Anandan, G. Saritha, Natural sensitizers for dye sensitized solar cell applications, Int. J. Sci. Eng. Res. 5 (2014).
[39] E.M. Abdou, H.S. Hafez, E. Bakir, M.S.A. Abdel-Mottaleb, Photostability of low cost dye-sensitized solar cells based on natural and synthetic dyes, Spectrochim. Acta A Mol. Biomol. Spectrosc. 115 (2013) 202–207, http://dx.doi.org/10.1016/j.saa.2013.05.090.
[40] M. Alhamed, A.S. Issa, A.W. Doubal, Studying of natural dyes properties as photosensitizer for dye sensitized solar cells (DSSC), J. Electron. Devices 16 (2012) 1370–1383.